ELASTICITY AND CONTRACTANCY OF HAWAIIAN OLIVINE THOLEIITE AND ITS ROLE IN THE STABILITY AND STRUCTURAL EVOLUTION OF SUBCALDERA MAGMA RESERVOIRS AND RIFT SYSTEMS

By Michael P. Ryan

ABSTRACT

Experimental data for the high-temperature elasticity of Hawaiian olivine tholeiite have been evaluated to 1133 K. Young's modulus and the modulus of rigidity demonstrate a linear decrease with increasing temperature. Regression equations developed for replicate runs during flexural resonance have yielded the following relation for the high-temperature Young's modulus: $E(T)=(6.054-0.00083T)\times 10$ GPa. For the rigidity, replicate runs conducted in torsional resonance have yielded the following regression relation: $\mu(T)=(2.615-0.00038T)\times 10$ GPa. Parallel experiments conducted to 973 K have yielded evaluations of the high-temperature expansivity of Hawaiian olivine tholeiite. The linear thermal-expansion coefficients range from $\alpha_L=4.58\times 10^{-6}$ °C^{-1} at 373 K to $\alpha_L=7.93\times 10^{-6}$ °C^{-1} at 973 K. Conducted on the same samples used for the elasticity studies, they have provided a set of internally consistent correction factors for the final evaluations of $E(T)$ and $\mu(T)$. Comparisons of the measured moduli and their temperature derivatives with theoretically predicted values are in good overall agreement. Comparisons of the measured high-temperature thermal expansivities with predictions based on mixing-model computations for basaltic blends of forsterite, augite, and labradorite compare favorably.

A model developed for the high-temperature elasticity of basalt uses the Voigt-Reuss-Hill averaging procedures to provide upper and lower bounds on the aggregate elasticity of basic and ultrabasic rocks. General in nature, it has herein been specialized for basalt. In the general treatment, the composition is variable, ranging from monomineralic aggregates to assemblages with multiple components. The resulting compositional model works directly with the single-crystal properties for each component: molar volumes, adiabatic elastic stiffness and compliance coefficients, and the Voigt and Reuss temperature derivatives for the bulk modulus and rigidity of each mineral phase. The Hill averaging procedure provides a set of median estimates for aggregate elasticity. The parametric contributions of spherical voids (vesicles) and elongate voids (microcracks) that weaken the otherwise pristine solid are incorporated by the self-consistent averaging procedure.

The pressure dependence of elastic-wave velocities for tholeiitic and alkalic basalt, gabbro, periodotite, dunite, and harzburgite is controlled by the progressive closure of microfractures with increasing depth in volcanic systems. For basalt and gabbro, pore-fluid-accessible fracture space is continuously squeezed out as the confining pressures increase within volcanic shields, thus providing a physical background and certain key elements in developing the concept of contractancy in magmatic systems. Combined with geologic observations that bear on the nature of macroscopic fracture networks near the surface of shield volcanoes, the role of contractancy rationalizes: (1) the highly nonlinear confining pressure dependence of compressional and shear wave velocities in intact basaltic rocks; (2) the systematics of $\partial V_p/\partial Z$ for the seismic-velocity profiles for Hawaii, including the low-velocity residuals that characterize the near-surface environment; and (3) the observed in-situ density systematics that characterize the stratigraphy of shield volcanoes, including the frequent observation of their low values at shallow depths. A corollary of the contractant behavior of shield volcanoes is the crossover in the in-situ densities of tholeiitic melt near its liquidus and that of its country-rock environment. This crossover occurs in the nonlinear region of the contractancy curves. In the heart of the crossover is a subregion of neutral buoyancy, where $\rho_{\text{country rock}}-\rho_{\text{melt}}\approx 0$. This behavior rationalizes the long-term stability of tholeiitic magma reservoirs and the frequently observed resting place of intrusives (for example, dikes in rift zones) that lie just beneath the surface of active volcanoes. As Hawaiian volcanoes evolve, they carry their contractancy curves with them. The concept of a contraction profile that has an evolutionary track paralleling the upward growth of the volcanic shield provides the mechanical rationale for the upward climb of subcaldera magma reservoirs as the shield progresses from youth to maturity.

THE HIGH-TEMPERATURE ELASTICITY OF HAWAIIAN BASALT

INTRODUCTION

Elastic moduli are essential to the computation of the displacements, strains, and stress distributions that occur in volcanic systems. Provided the level of the applied loading is below the elastic limit, the strains describing the resulting shape changes are recoverable, and load removal returns the body to its original condition. Imposing the idealization that the load application and strain response is independent of direction allows relating the moduli within a generalization of Hooke's law:

$$T_{ij}=\lambda\epsilon_{kk}\delta_{ij}+2\mu\epsilon_{ij}, \qquad (1)$$

where T_{ij} is a symmetric second-order stress tensor, ϵ_{kk} is a tensor relating volumetric or dilatational strains to the applied loading (T_{ij}), ϵ_{ij} is a second-order tensor that describes the distortional strains that have been generated, δ_{ij} is the Kronecker delta, and λ and μ are the Lamé elastic constants. The Lamé constants are in turn related to the Young's modulus E, the shear modulus G, and Poisson's ratio ν by:

$$\mu = G = \frac{E}{2(1+\nu)} \quad (2)$$

and

$$\lambda = \frac{\nu E}{(1+\nu)(1-2\nu)}; \quad (3)$$

the bulk modulus K, relating mean pressure and volumetric strain, is

$$K = \lambda + \tfrac{2}{3}G = \frac{E}{3(1-2\nu)}. \quad (4)$$

Two of these moduli are of particular use in volcanology. They are the Young's modulus and the modulus of rigidity, or the shear modulus. These moduli are the familiar connecting links between uniaxial stress and strain and shear stress and strain. They are indispensable in continuum analyses of the displacement, stress, and strain fields that accompany magmatic intrusion, the subsidence produced by magmatic withdrawal, and numerous related problems concerned with the mechanics and dynamics of active volcanoes. The experimental program has grown out of the author's interest in the fracture mechanics of intact basaltic rocks near their melting point, in low-pressure environments. Accordingly, a series of experiments was undertaken to provide data on the mechanical parameters required for computations related to crack growth near the solidus.

Prior studies of the temperature dependence of the elastic moduli of basalt have been of two types. The first approach focused on the evaluation of compressional- and shear-wave velocities primarily as a function of confining pressure, but taken over a moderate range in temperature. An example of this approach was provided by Hughes and Cross (1951) and Hughes and Maurette (1957), who evaluated compressional-wave velocities (V_p) and shear-wave velocities (V_s) (from which moduli may be derived) to 600 MPa (6 kbar) and 300 °C. The second approach seeks to determine the temperature dependence in high-temperature environments that cover a significant fraction of the interval from ambient to solidus temperatures. Here, the elastic moduli were of primary interest. Existing work on basalt is limited to the studies of Volarovich and Gurvich (1957), Iida and Kumazawa (1960), and Wingquist (1971). Kern and Richter (1979) extended the earlier temperature limits to 700 °C, in a series of V_p and V_s determinations on altered basalt from the Faroe Islands, with confining pressures to 600 MPa.

The objective of this section is evaluation of the elasticity and expansivity of Hawaiian olivine tholeiite. The primary focus is the evaluation of Young's modulus and the modulus of rigidity, to 1,133 K. Linear thermal-expansion coefficients have been measured in a parallel set of experiments to 973 K.

With respect to the evaluations of the elastic moduli, the present work complements the earlier studies—and is distinct from them—in: (1) combining a theoretical approach for moduli prediction with a parallel experimental program, and using the results of the model predictions to rationalize the compositional and microstructural dependence of elasticity at high temperatures; (2) extending the temperature range from ambient to 1,133 K; (3) focusing on basalt from the Hawaiian province; (4) working with pristine samples that have been unaffected by alteration processes; and (5) refining the resonance approach to incorporate a series of correction factors that properly account for the effects of thermal expansivity.

For the purposes of this report, all rock-unit names are used informally, although some are formal names.

ACKNOWLEDGMENTS

The collaborative support of Robert Koyanagi is gratefully acknowledged. Fred Klein prepared large-format seismic hypocenter maps. David Popish assisted with the early phases of protracted machine-shop activities. Logistical support by the staff of the Hawaiian Volcano Observatory has contributed in several ways. Particularly helpful have been Thomas Wright, Reginald Okamura, Arnold Okamura, and James Griggs. William F. Brace kindly provided samples of diabase. Ruthie Robertson prepared the typescript with characteristic accuracy and grace. Figures have been prepared with the assistance of Jewel Dixon, Lindel Keaton, Marcia Prins, and Betty Shallcross. Tom Chase kindly loaned marine bathymetry negatives. Thoughtful review comments by Richard C. Bradt, Earl K. Graham, Robert Y. Koyanagi, Manuel Nathenson, Eugene C. Robertson, Roger M. Stewart, and Robert I. Tilling have led to improvements in the manuscript. Portions of the work have been carried out with the support of a Grove Karl Gilbert Fellowship under the auspices of the Geologic Division of the U.S. Geological Survey. Additional support has been provided by the U.S. Department of Energy, Office of Basic Science, under interagency agreement No. DE-AI-1-79RA50294.

MEASUREMENTS OF THE ELASTIC MODULI OF BASALT

An early consideration in the experimental program dealt with preparing appropriate samples. Sample-selection criteria included (1) an intact lithology that would be representative of volumetrically large portions of Hawaiian shields; (2) individual samples that are pristine; and (3) a sample site that provides for good cross-sectional exposures within the interior of lava flows. These criteria are well satisfied by the Boiling Pots flow units that crop out west of Hilo (fig. 52.1). Details of the sample sites and flow structures in cross section are provided by Ryan and Sammis (1978).

THE BASALT OF BOILING POTS

Mineralogy and Petrography

Petrographically, the basalt of Boiling Pots is characterized by phenocrysts and microphenocrysts of olivine, scattered microphenocrysts of hypersthene (almost invariably jacketed with augite), plagioclase, and some augite, set in a very fine grained groundmass of subcalcic augite, pigeonite, magnetite, plagioclase microlites, and dark-amber glass. Textural relations are shown in figure 52.2. Modal analyses (table 52.1) are representative of samples in the experimental evaluations of moduli and expansivity.

Electron-microprobe analyses of the crystalline silicates in the basalt of Boiling Pots were performed with an ETAC Autoprobe. The microprobe was operated at 15-kV accelerating voltage and 0.04-μA current and used a 2.0-μm-diameter focused electron beam. Polished petrographic thin sections were prepared from samples from positions in the basalt blocks adjacent to sample locations for high-temperature elastic moduli and expansivity measurements.

TABLE 52.1.—*Modal mineral abundance in the basalt of Boiling Pots*

[Totals for mineral groups are given in last column; values are in modal percent]

Olivine (phenocrysts)	9.3	12.42
Olivine (microphenocrysts)	3.1	
Hypersthene (augite-jacketed)	2.8	
Augite (microphenocrysts)	.1	32.91
Subcalcic augite + pigeonite (groundmass)	29.9	
Plagioclase (microphenocrysts)	1.8	37.37
Plagioclase (microlites)	35.4	
Magnetite (euhedral, groundmass)	4.3	
Glass (with opaque dustings)	12.9	

Olivine.—Olivine is present as subhedral phenocrysts ranging in mean diameter from 2 to 5 mm and as subhedral to anhedral microphenocrysts ranging from 2,000 by 1,300 μm to 520 by 130 μm. Opaque inclusions (chrome-spinel?) are common, while inclusions of amber glass are less common and are in the more poikilitic olivine. Inferred reaction with the melt has corroded crystal faces, and augite rims are present as continuous jackets and as closely spaced neighboring crystals. Transgranular fracture is nearly always present in the larger phenocrysts.

The forsterite content of olivine phenocrysts from the Boiling Pots samples was determined using the X-ray determinative curve of Yoder and Sahama (1957):

$$\text{Fo (in mole percent)} = 4{,}233.91 - 1{,}494.59\ d_{130}$$

where d_{130} refers to the interplanar spacing (in Å) from the (130) reflection. The average of the determinations yielded a composition of $Fo_{90.1}$. The error associated with the determinative curve is 3 to 4 mol percent (Yoder and Sahama, 1957, p. 486). Zoning in olivine microphenocrysts was studied by use of the electron microprobe. Radial microprobe traverses from the center to edge of crystals show relatively magnesian cores and more fayalitic margins. The compositional range covered is $(Mg_{0.86}Fe_{0.14})_2SiO_4$ in the core to $(Mg_{0.78}Fe_{0.22})_2SiO_4$ near the margin. Errors attached to the determination of Mg and Fe are ±1.5 percent and ±2.0 percent, respectively. The combined X-ray analysis and microprobe analyses suggest that the forsterite content of Boiling Pots olivine ranges from $Fo_{90.1}$ in early phenocrysts to $Fo_{78.5}$ as the late olivine crystallized during microphenocryst formation.

Pyroxenes.—Augite is present as reaction rims on olivine and hypersthene microphenocrysts and as discrete euhedral to subhedral crystals ranging from about 200 to 100 μm in diameter. Individual microphenocrysts generally are optically homogeneous but may contain minute inclusions of glass. Microprobe analyses of augite microphenocrysts indicate compositions close to $Wo_{36}En_{50}Fs_{14}$.

Hypersthene microphenocrysts are elongate (1,000 by 100 μm) to stubby (75 by 75 μm) and are invariably mottled medium gray under crossed nicols. Euhedral prismatic (100), (010) faces are typically jacketed with augite reaction rims that range in thickness from 10 to 20 μm. Euhedral terminations, however, are rare, and the hypersthene laths have no augitic jacket on the terminations, suggesting breakage during postreaction fluid movement. Crystallographically aligned blebs, stringers, and lamellae of augite commonly are present within the hypersthene host and have the same optical orientation as the external jackets. Approximately aligned poikilitic zones frequently contain opaque-rich glass inclusions. Hypersthene laths that have grown into contiguity with a neighboring olivine microphenocryst may have jackets of augite that not only rim the hypersthene but enclose the olivine as well. In this role, augite has acted as the welding agent in the formation of occasional glomerocrysts.

Electron-microprobe studies of hypersthene microphenocrysts and their jackets of augite were performed using the ETEC Autoprobe. Hypersthene laths are relatively homogeneous with respect to Ca, Mg, and Fe and have internal compositional ranges near $Wo_{3.8-4.1}$, $En_{81.6-82.1}$, and $Fs_{13.9-14.2}$. The composition of the augitic jackets on the prismatic faces is $Wo_{32.8}En_{47.5}Fs_{19.5}$, suggesting that relative to the melt that produced most augite microphenocrysts, depletion in Ca and Mg and enrichment in Fe had taken place by the time augite jacketing occurred.

Pigeonite is present as irregular groundmass crystals that are invariably anhedral. Mean diameters range from 40 to 20 μm, and their diminutive size lets them occupy vacant positions between adjoining plagioclase microlites in the groundmass topology, thus giving the rock fabric an intergranular character.

Plagioclase.—Plagioclase is present both as sparse microphenocrysts measuring 400 by 60 μm and as tiny groundmass microlites in the 70- to 40-μm length range, with widths of approximately 20 μm. Twinning follows both the Carlsbad law and albite law, and most microlites have 3 to 8 albite-twin individuals. Plagioclase compositions were determined using the ETEC Autoprobe, where the 2-μm beam diameter permitted analyses to be performed in microlite interiors without including surrounding glass or groundmass clinopyroxene within the excitation volume. The results of microlite analyses span the compositional range $Ab_{27.3-39.0}$, $An_{72.2-60.0}$, $Or_{0.5-0.9}$.

Magnetite is present as discrete euhedral crystals whose equant dimensions are approximately 10 μm. These crystals form a minor groundmass component (4.3 modal percent), and they occupy interstitial positions between adjoining plagioclase microlites in the crystalline groundmass network. Glass is medium to dark amber and is generally heavily dusted with opaque particles. Glass is present as thin films separating subparallel plagioclase microlites and as scattered equant pools and triangular patches. No evidence for devitrification has been found and, with the exception of the associated opaques, the glass is optically homogeneous at all levels of magnification.

Plots of weight percent $K_2O + Na_2O$ versus weight percent SiO_2 for the Boiling Pots basalt fall well within the tholeiitic field on an alkali-silica diagram (see, for example, Tilley, 1950; Macdonald and Katsura, 1964). Consistent with a tholeiitic nature, suggested by relations between these oxides, is the common reaction relation between magnesian olivine and their rims of augite.

Microstructure.—The three-dimensional microstructure of several Boiling Pots olivine tholeiite samples was examined using a scanning-electron microscope (SEM). This method provided a means of examining: (1) crystal-glass relations between olivine, pyroxene, plagioclase, and the 13-modal-percent interstitial glass; (2) differences in the behavior of glass above and below the glass-transformation temperature, T_g; (3) intragranular and intergranular

microfractures and the appropriateness of the assumption of a needle-shape geometry for voids representing microfractures in the elastic microstructural model; and (4) vesicles and vesicle shapes to assess the assumption of spherical voids in the approximation used in the elastic microstructural model.

The study employed a Cambridge Stereoscan (600) scanning-electron microscope with a peak accelerating voltage of 25 kV and a maximum resolution of 250 Å. The electron source was a tungsten-wire filament operated at 10^7 electrons s^{-1} and was maintained under a vacuum of 10^{-5} mm Hg.

The results of the SEM study are as follows:

(1) The glass phase covers practically all matrix crystals with a coat of varying thickness. The only general exceptions to this phase are crystals that are immediately adjacent to vesicles.

(2) Spherical geometry is a fair to good approximation for the shape of most observed vesicles, thus suggesting that the assumption of spherical voids in the elastic microstructural model is appropriate (see section "Modeling the High-Temperature Elasticity of Basalt").

(3) Needle-shaped geometry may be a fair approximation for the shape of many observed microcracks. (This is not always the case, however, as many microcracks have irregular geometries that resemble complexly warped planes.)

Porosity.—Most of the porosity in basalt samples may be attributed to spherical or nearly spherical vesicles that, in general, are not interconnected. Another type of porosity occurs in the form of microcracks that are produced as a result of microscopic contraction anisotropy in the fabric of the cooling rock. These microcracks take the form of intracrystalline fractures (especially in olivine microphenocrysts) and intercrystalline fractures along the margins of microlites and surrounding glass.

Because much of the total porosity is of an isolated form, measurement of the absolute porosity was the appropriate approach to assess the overall level of porosity.

The absolute porosity (in percent) may be expressed as

$$\Phi_A = \left(\frac{V_v + V_{mc}}{V_v + V_{mc} + V_{xtl+gl}} \right) \times 100, \qquad (5)$$

where V_v is the volume of vesicles, V_{mc} is the volume of microcracks, and V_{xtl+gl} is the volume of the matrix of crystals and glass.

To measure absolute porosity, the bulk (total) volume of a 5.25-cm by 1.25-cm by 0.75-cm sample was measured with a mercury pycnometer. The sample was crushed to 100 mesh with a percussion mortar and pestle. This method effectively released the contribution of the noncommunicating pores and microcracks in the interior of the sample, so that their volume would be added to the total void volume. The volume of the crushed sample was measured using a Russell volumeter, employing kerosene as the working fluid. The difference between the pycnometer and the volumeter measurements is the contribution of vesicle and microcrack volumes to the total (bulk) volume. The measured values are believed to be accurate to ±0.1 percent. Measured absolute porosities ranged from 21.4 to 14.3 percent for combined samples.

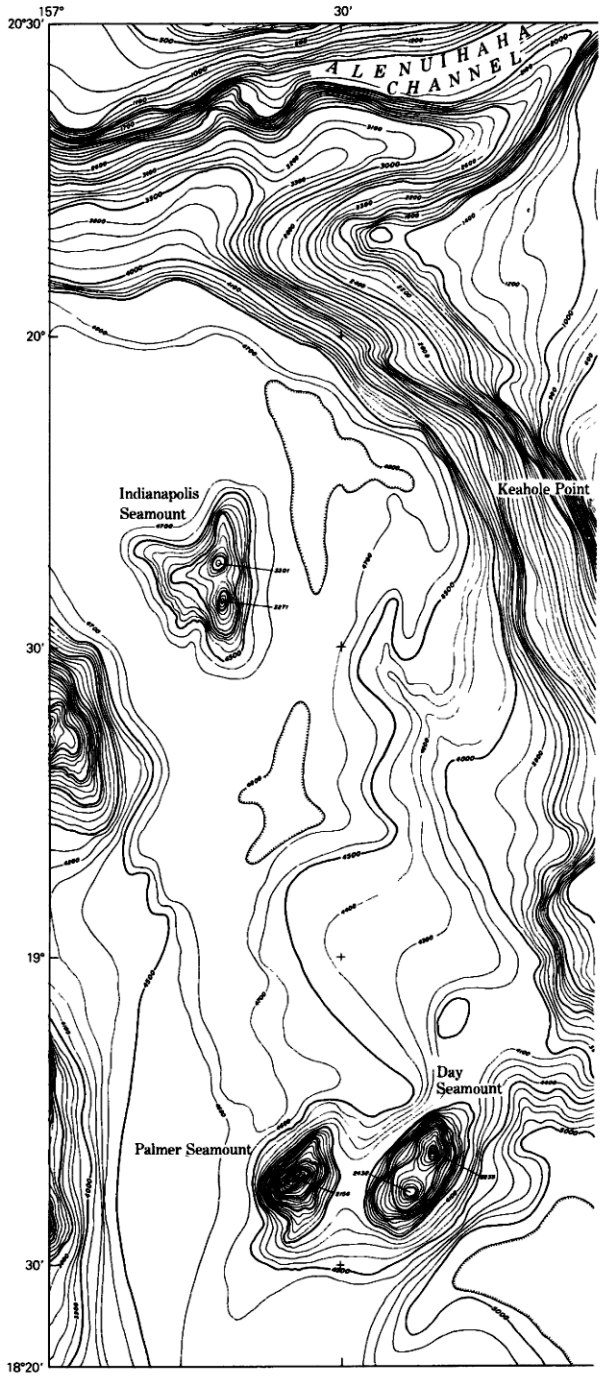

FIGURE 52.1.—Topography of Island of Hawaii, showing summits of principal volcanic shields, Loihi Seamount, and major seamounts of south Hawaii. Surmounting subcaldera magma reservoirs and rift zones of active volcanoes Mauna Loa, Kilauea, and Loihi Seamount is a heavily fractured veneer of country rock characterized by exceptionally low in-situ values of compressional-wave velocity

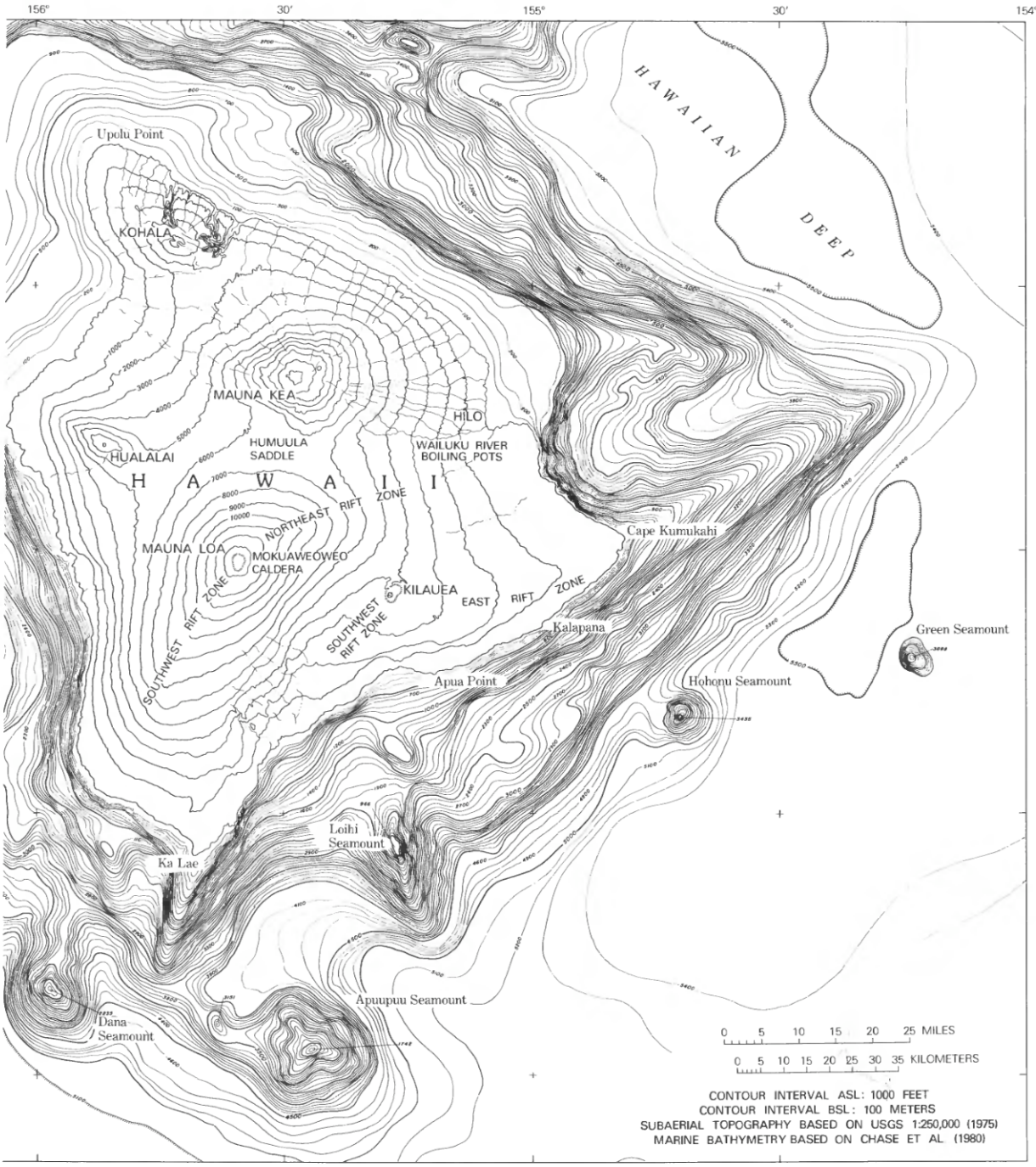

and density. Supersolidus intrusives within magma reservoirs and rift zones of these growing shields are stabilized by crossovers in in-situ density of tholeiitic melt near its liquidus and that of surrounding—and surmounting—country rock. As volcanic centers evolve, they carry their surficial veneer of low-density country rock with them, continuously providing a region of neutral buoyancy for magma within the shield. This, in turn, provides mechanical rationale for upward climb of subcaldera magma reservoirs, as evolving volcano progresses from submarine infancy through subaerial maturity to old age.

EXPERIMENTAL PROGRAM

The experimental program for the evaluation of elastic moduli employs the dynamic resonance technique developed by Spinner and Tefft (1961) and is based on earlier approaches of Ide (1936) and Förster (1937), who first recognized that controlled mechanical resonance provided a means of measuring the elastic moduli of solids. The computational approach used in evaluating the Young's modulus and shear modulus from the respective flexural and torsional resonant frequencies is based on the presentation in Hasselman (1961).

A Nametre (model 12) acoustic spectrometer was used to induce and record the resonant vibrational frequencies. A schematic diagram of the spectrometer and supporting equipment is shown in figure 52.3. The spectrometer consists of a Hewlett-Packard (3310A) function generator, which produces a sinusoidal output waveform ranging from 0.01 Hz to 100 kHz. Mechanical vibrations were transmitted to the sample by an Astatic commercial cutting head. A second Astatic (x-26) cutting head acted as a pickup transducer. The transducers are composed of quartz crystals, which provide the piezoelectric transmission and reception. Output from the pickup-transducer power amplifier was displayed on a Hewlett-Packard (122A) cathode-ray-tube oscilloscope, which provided a

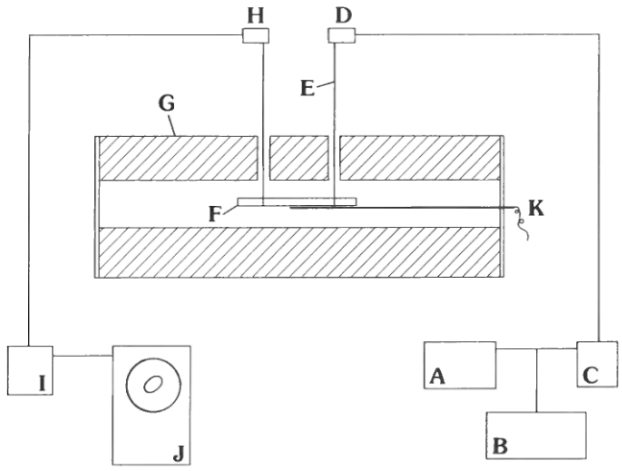

FIGURE 52.3—Schematic diagram of components of assembly for dynamic flexural and torsional resonance measurements at high temperatures: (A) variable-frequency signal generator; (B) digital frequency counter; (C) power amplifier; (D) driving transducer; (E) sample suspension system; (F) sample; (G) Kanthal-wound resistance furnace; (H) pickup transducer; (I) pickup power amplifier; (J) oscilloscope; and (K) platinum-platinum·10 percent rhodium thermocouple.

FIGURE 52.2—Photomicrograph of olivine tholeiite from Boiling Pots. Olivine phenocrysts are surrounded by plagioclase microlites set in a finer grained groundmass of pyroxene microcrysts and intercrystalline glass (heavily dusted with opaques). Under crossed nicols. Field of view is 400 μm by 600 μm.

graphical presentation of vertical-displacement amplitudes in the resonating sample. An associated voltmeter provided the means of maximizing the sample resonance via maximizing the pickup-transducer power-amplifier voltage. Digital readout of the resonant frequency was provided by a Hewlett-Packard (5325B) frequency counter with a range of 5 Hz to 10 MHz and a lower resolution of 0.01 Hz.

Ambient temperature measurements for both the Young's modulus and shear modulus evaluations employed electromagnetic noncontact transducers that induced and picked up vibration in the sample via metal tabs epoxyed to the sample ends.

High-temperature measurements employed an Alumel-wire suspension system connected from the transducers to the sample nodal points. A Satec Systems (Se-17p) Kanthal-wound, horizontally mounted furnace provided the high-temperature environment. Temperatures were maintained with a Thermoelectric (400 series) proportional controller, and a platinum-platinum·10 percent rhodium (Pt-Pt·10Rh) thermocouple.

Dynamic Young's Modulus at Ambient Temperatures

The Young's modulus (E) is evaluated at ambient pressure and temperature by applying equations relating the resonant frequency of the first mode of flexural vibration of an isotropic, homogeneous, elastic prism with a rectangular cross section to the sample mass and shape. Thus,

$$E=\left(\frac{0.94645Cmf^2}{B}\right)\times 10^2 \text{ MPa}, \tag{6}$$

where E is the Young's modulus evaluated at 25 °C, m is the mass (in grams) of the sample, f is the resonant frequency (in hertz) for the first mode of flexural vibration, B is the vertical dimension (in centimeters) of the cross section perpendicular to the direction of vibration, and C is a shape factor given by Hasselman (1961):

$$C=\left(\frac{D}{L}\right)-3\left[1+6.585(1+0.0752\nu+0.8109\nu^2)\left(\frac{D}{L}\right)^2 - \frac{100.083(1+0.2023\nu+2.173\nu^2)\left(\frac{D}{L}\right)^4}{12+76.06(1+0.14081\nu+1.536\nu^2)\left(\frac{D}{L}\right)^2} - 0.86806\left(\frac{D}{L}\right)^4\right], \tag{7}$$

where D is the thickness (in centimeters) of the sample cross section parallel to the direction of vibration, L is the sample length (in centimeters), and ν is Poisson's ratio.

Samples were prepared by machining 5.00- by 1.25- by 0.65-cm prisms from blocks of basalt that were judged to be homogeneous with respect to the distribution of vesicles and olivine phenocrysts. These rectangular bars were then resin-bonded to steel blocks, and the upper (free) surface ground parallel to the base in an automatic grinding machine. Rotation of the sample and subsequent regrinding assured that the upper and lower surfaces were parallel.

Sample dimensions were measured with a Mitutoyo micrometer, with a stated accuracy of ±0.002 cm. Sample masses were measured using a Mettler electronic balance, with an accuracy of ±0.001 g. Sources of error reside primarily in the measurements of sample geometry (length, width, and height) and sample mass. An additional source of error may result from slight deviations in rectilinearity of the overall geometry. Maximum resolution of resonant frequency on the Hewlett-Packard digital counter was 0.01 Hz; however, resonant frequencies were read to the nearest cycle per second. Table 52.2 summarizes the dynamic Young's modulus at 23 °C in selected samples.

Calibration of the acoustic spectrometer was performed by measurements of the dynamic Young's modulus of fused-silica frequency standards and established a precision of ±0.01 Hz for the fundamental bending mode of resonant vibration.

Single Crystals and Basaltic Rocks

A preliminary estimate of the modulus defect ($\Delta E/E_o$) produced by the included voids in basalt may be made by combining single-crystal elastic moduli on a weighted-average basis (see fig. 52.4). The Hill-averaged Young's moduli have been computed for each mineral by application of the standard relation of Birch (1960):

$$E_{\mathrm{VRH}}^{\mathrm{XTL}}=\frac{9(K_{\mathrm{VRH}}^{\mathrm{XTL}}\,\mu_{\mathrm{VRH}}^{\mathrm{XTL}})}{3K_{\mathrm{VRH}}^{\mathrm{XTL}}+\mu_{\mathrm{VRH}}^{\mathrm{XTL}}}, \tag{8}$$

where the subscript VRH denotes a Hill-averaged value and the superscript XTL denotes a single-crystal quantity.

Applying the mixing relations for K_{VRH} and μ_{VRH} for a polyphase mixture (see section "Modeling the High-Temperature Elasticity of Basalt"), the Young's modulus for a model basalt composition, $Fo_{100}=0.10$, augite $=0.45$, $An_{56}=0.45$, may be calculated by a second application of the standard relation, where $K_{\mathrm{VRH}}^{\mathrm{MIX}}$ and $\mu_{\mathrm{VRH}}^{\mathrm{MIX}}$ are evaluated at 25 °C and denote the bulk modulus and rigidity for the aggregate:

$$E_{\mathrm{VRH}}^{\mathrm{MIX}}=\frac{9(K_{\mathrm{VRH}}^{\mathrm{MIX}}\,\mu_{\mathrm{VRH}}^{\mathrm{MIX}})}{3K_{\mathrm{VRH}}^{\mathrm{MIX}}+\mu_{\mathrm{VRH}}^{\mathrm{MIX}}}. \tag{9}$$

Employing the bulk modulus (K) and rigidity (μ) values $K_{\mathrm{VRH}}=129$ GPa and $\mu_{\mathrm{VRH}}=81.6$ GPa for Fo_{100} (Graham and Barsch, 1969), $K_{\mathrm{VRH}}=95.6$ GPa and $\mu_{\mathrm{VRH}}=57.9$ GPa for augite (Aleksandrov and others, 1964), and $K_{\mathrm{VRH}}=72.0$

TABLE 52.2.—*Ambient-temperature dynamic Young's modulus for basalt of Boiling Pots*

[Young's modulus (E) evaluated at 23 °C]

Sample	E (GPa)	Porosity (percent)
BP-75-R7	74.70	14.3
BP-75-R2	62.78	15.1
BP-75-R4	62.60	15.6
BP-75-R6	60.52	15.8
BP-75-R1	60.39	15.8
BP-75-R5	60.06	16.8
BP-75-R3	55.90	17.8

GPa and $\mu_{VRH}=34.3$ GPa for An_{56} (Ryzhova, 1964) yield a value of 110.39 GPa.

A comparison between the Young's modulus of this basaltic mixture of single crystals and that of the Boiling Pots olivine tholeiite reveals an appreciable gap of 47 GPa.

This difference in predicted and observed elasticity results from voids (vesicles and microcracks) in the basalt matrix, and so the hachured band in figure 52.4 has accordingly been labeled "defects." It probably, however, represents the maximum effect of microstructure, because the contributions of glass and opaque minerals have not been incorporated.

Dynamic Elastic Moduli at High Temperatures

Measurements made at high temperatures employed the following additional procedures:

(1) From 25 °C, the set point on the proportional temperature controller was moved up in 25-°C increments. At each increment, a measurement of the flexural or torsional resonant frequency was made.

(2) As the temperature of a sample increases, the flexural (or torsional) frequency at which it absorbs mechanical energy and resonates is continuously lowered.

(3) A uniform sample temperature was provided by blanketing the entire Kanthal resistance furnace with Kaowool spunglass insulation. Care was taken so that filaments of spunglass made no physical contact with the suspension system.

(4) Thermal equilibrium after a 25-°C increment generally required about 1 hour to achieve after the temperature from the thermocouple had matched the set point on the proportional controller. The test of equilibrium was a stationary resonant frequency for a 10- to 15-minute time interval. The overall heating rate from 25 °C to the maximum temperature (T_{max}) was 1.1 °C min^{-1}.

(5) As temperatures were increased to high levels (in excess of 700 °C), measurements were made until the aperture of the Lissajous figure was no longer a reliable indicator that resonance had been achieved.

(6) Corrections for the effect of thermal expansion were made, using the temperature-dependent linear thermal-expansion coefficients, $\alpha_L(T)$, evaluated at 100 °C increments.

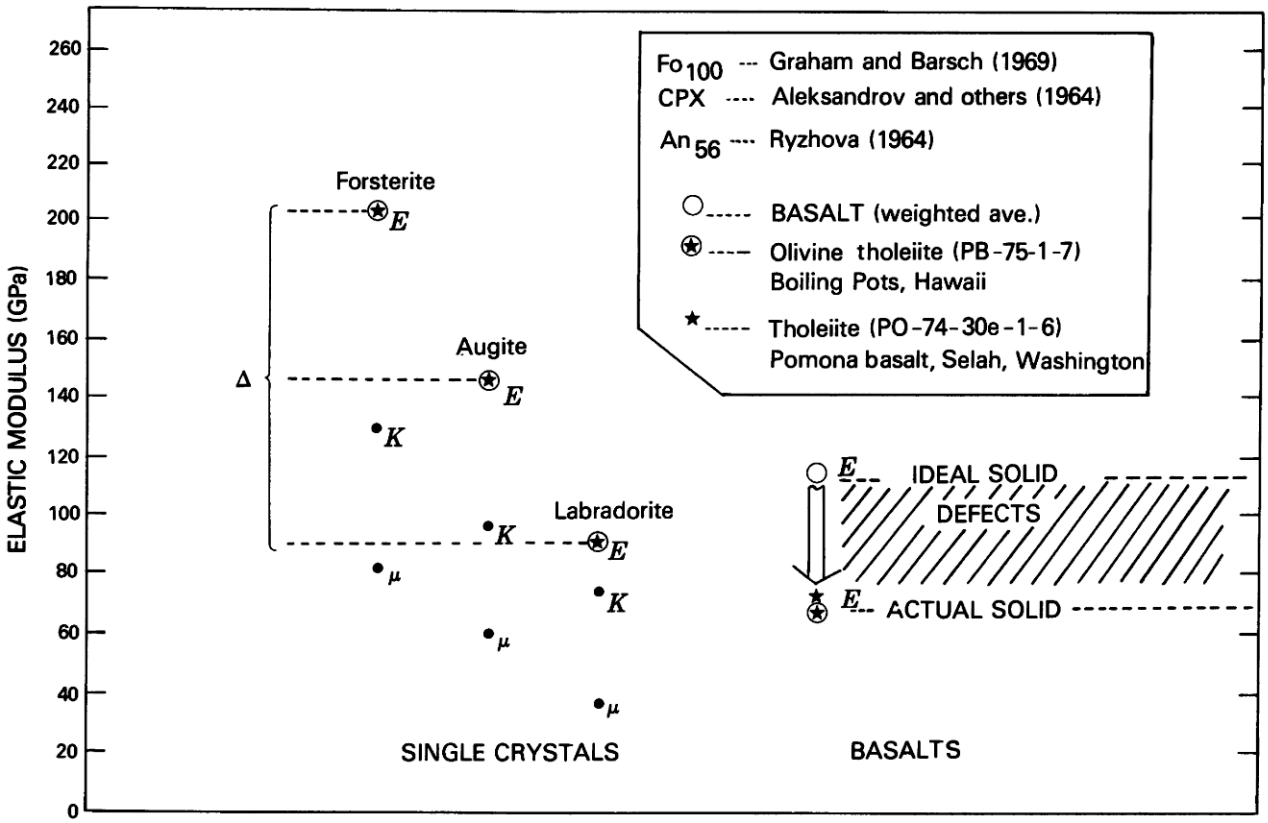

FIGURE 52.4.—Elastic moduli of single-crystal candidates of basalt mineralogy. Young's modulus (E) for ideal solid is weighted average of E values for forsterite, augite, and labradorite. Bulk modulus, K, rigidity, μ, and Young's modulus, E, for forsterite, augite, and labradorite have been included for comparison. Hachured area represents difference between computed composite and measured values for rock and is interpreted as being contribution of defects (vesicles and microcracks) present in rock but not represented in compositional estimate.

(7) Resonant frequencies obtained with the high-temperature Alumel suspension wires at ambient temperature were compared with frequencies obtained with the electromagnetic drive and pickup system.

Shear modulus.—Ambient-temperature evaluations of the shear modulus have followed a procedure that is similar to the Young's modulus evaluations. The essential difference requires the transverse excitation of the sample to induce torsional resonant vibrations instead of flexural vibrations.

Evaluations of the high-temperature shear modulus, μ, were made by relating the temperature-dependent torsional resonant frequency to the shear modulus and torsional resonant frequency determined at 25 °C (Hasselman, 1961):

$$\mu(T)=\mu(25)\frac{f_T^2}{f_{25}^2}\left[\frac{1}{1+\alpha_l(\Delta T)}\right], \qquad (10)$$

where $\mu(25)$ is the ambient-pressure, 25-°C shear modulus or rigidity, f_{25}^2 is the 25 °C torsional resonant frequency, f_T^2 is the high-temperature torsional resonant frequency, and $\alpha_L(\Delta T)$ is the temperature-dependent linear thermal-expansion coefficient for basalt, which enters as a correction factor.

Figure 52.5 presents the replicate rigidities and provides a comparison with available data for the high-temperature rigidity of basalt. The values from Wingquist (1971) are for the Dresser basalt, and those from Iida and Kumazawa (1960) are for the 1950 lava of Mihara Volcano (Izu, Oo-Shima, Japan). Table 52.3 lists the rigidity as a function of temperature to 800 °C. The linear-regression relation for $\mu(T)$ from 25 to 700 °C for sample BP-75-R2 is

$$\mu(T)=(2.611-0.00035T)\times 10 \text{ Gpa}, \qquad (11)$$

for sample BP-75-R4

$$\mu(T)=(2.618-0.00042T)\times 10 \text{ GPa}, \qquad (12)$$

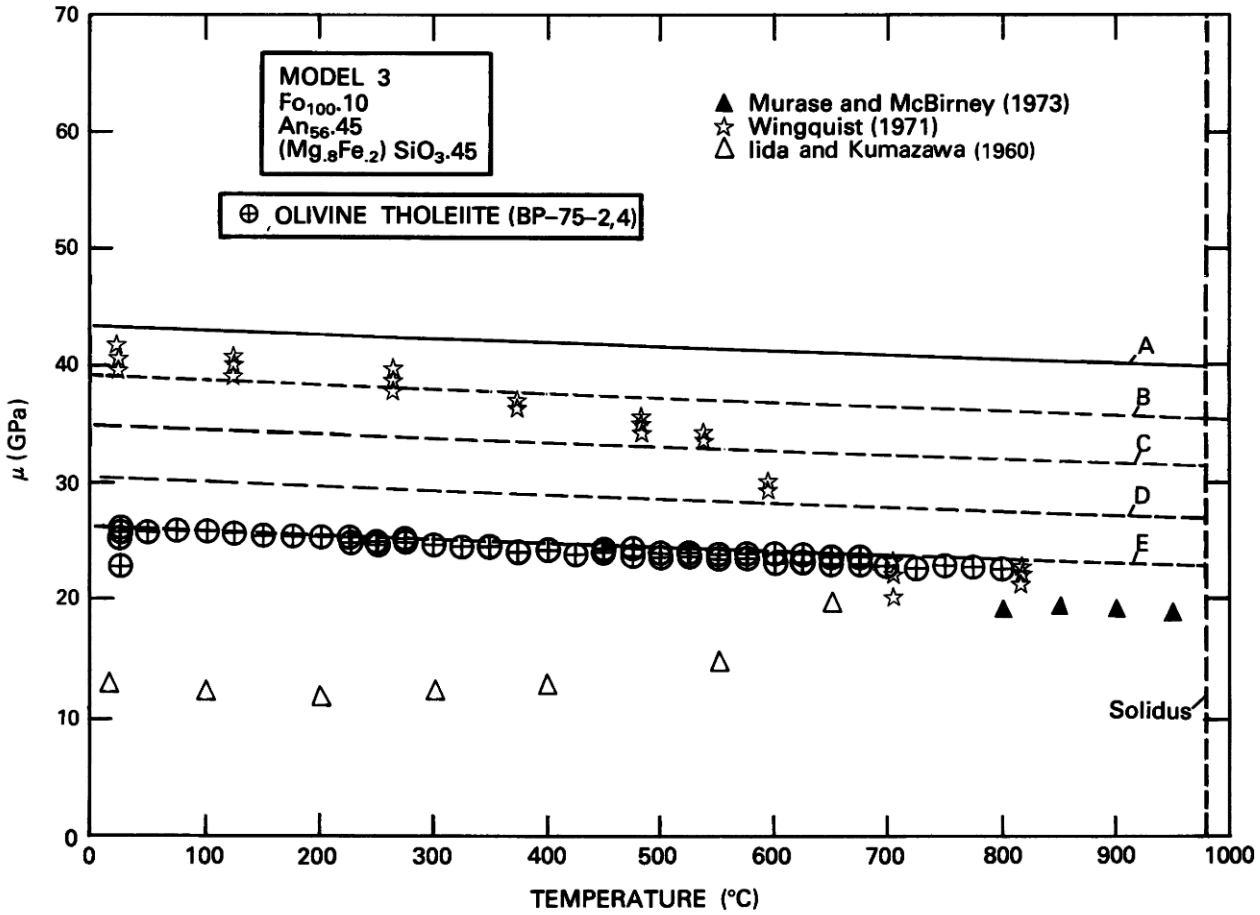

FIGURE 52.5.—High-temperature, ambient-pressure rigidity of Hawaiian olivine tholeiite. Solid line (A) has been computed using V-R-H averaging procedure and a compositional submodel 3 mixture of forsterite, plagioclase, and pyroxene. Computed high-temperature rigidities B, C, D, and E have incorporated progressively higher fractions (5, 10, 15, and 20 percent, respectively) of spherical voids—representing mechanical weakening effects of vesicles. Computed and measured temperature derivatives of μ, $d\mu/dT$, compare favorably.

TABLE 52.3.—*Shear modulus as a function of temperature*
[Sample BP-75-R4(G)]

$$\mu(T)=\mu(25)\underbrace{\left(\frac{F_T^2}{F_{25}^2}\right)}_{A}\underbrace{\left(\frac{1}{1+\alpha_l(\Delta T)}\right)}_{B}$$

Temperature (T) (°C)	A (GPa)	B	$\mu(T)$ (GPa)	$\frac{\mu(T)}{\mu(25)}$
25	26.1	1.0000	26.1	1.00
50	25.9	.9998	25.9	.99
75	25.8	.9997	25.8	.99
100	25.7	.9996	25.7	.98
125	25.6	.9995	25.6	.98
150	25.6	.9993	25.5	.98
175	25.5	.9992	25.4	.97
200	25.4	.9991	25.4	.97
225	25.3	.9989	25.2	.96
250	25.2	.9987	25.1	.96
275	25.1	.9986	25.0	.96
300	25.0	.9984	24.9	.95
325	24.8	.9983	24.8	.95
350	24.7	.9980	24.7	.94
375	24.6	.9979	24.6	.94
400	24.5	.9977	24.4	.93
425	24.3	.9974	24.3	.93
450	24.3	.9972	24.2	.92
475	24.2	.9970	24.1	.92
500	24.0	.9969	24.0	.91
525	23.9	.9962	23.8	.91
550	23.8	.9960	23.7	.90
575	23.7	.9958	23.6	.90
600	23.6	.9957	23.5	.90
625	23.6	.9952	23.4	.90
650	23.5	.9950	23.4	.89
675	23.5	.9948	23.4	.89
700	23.4	.9946	23.3	.89
725	23.3	.9937	23.2	.89
750	23.2	.9935	23.1	.88
775	23.1	.9932	23.0	.88
800	23.0	.9930	22.9	.87

and for the average of samples BP-75-R2 and BP-75-R4

$$\mu(T)=(2.615-0.00038T)\times 10\ \text{GPa}. \tag{13}$$

Rigidities obtained from the resonant-frequency values and their corresponding predicted values from the linear regression treatment have been compared to 700 °C. The value of the differences between measured and predicted values are the regression residuals. Comparisons of the magnitude of these residuals suggest that a linear temperature dependence for rigidity is appropriate over the interval 25–700 °C. An examination of the sign of the residuals with changes in temperature shows no systematics, either within the data of a single sample or between the pooled data of both samples. The evident linearity in the data is consistent with the behavior expected for a solid that is continuously increasing its volume, and concurs with the behavior in single-crystal studies of forsterite (Graham, 1969; Graham and Barsch, 1969) and bronzite (Frisillo, 1972), as well as in studies of nonsilicates (Jones, 1977) and the formalism of lattice dynamics (Leibfried and Ludwig, 1961).

Young's Modulus.—Evaluations of the Young's modulus, E, were made by relating the temperature-dependent flexural resonant frequency to the Young's modulus and the flexural resonant frequency determined at 25 °C (Hasselman, 1961):

$$E(T)=E(25)\frac{f_T^2}{f_{25}^2}\left[\frac{1}{1+\alpha_l(\Delta T)}\right], \tag{14}$$

where $E(25)$ is the ambient-pressure, 25 °C Young's modulus, f_{25}^2 is the 25 °C flexural resonant frequency, f_T^2 is the high-temperature flexural resonant frequency, and $\alpha_l(\Delta T)$ is the temperature-dependent linear thermal-expansion coefficient for basalt.

The thermal-expansion coefficient $\alpha_l(T)$ that was used to correct the shear moduli is the same one employed here. The Young's modulus of 54.0 GPa and an $E(T)/E(25)$ value of 0.894 for one sample may be compared with values of 54.6 GPa and 0.915 for the replicate, evaluated at their common high-temperature point of 725 °C.

Plots of E versus temperature are presented in figure 52.6 for both samples, and comparisons may be made with the available data for basalt, gabbro, and peridotite. Table 52.4 lists the values of $E(T)$ to 865 °C.

The regression equations for the temperature dependence of the Young's modulus in the Boiling Pots basalt for sample BP-75-R6 is

$$E(T)=(6.059-0.00085T)\times 10\ \text{GPa}, \tag{15}$$

for sample BP-75-R1

$$E(T)=(6.049-0.00081T)\times 10\ \text{GPa}, \tag{16}$$

and for the average of samples BP-75-R6 and BP-75-R1

$$E(T)=(6.054-0.00083T)\times 10\ \text{GPa}. \tag{17}$$

TABLE 52.4.—*Young's modulus as a function of temperature*
[Sample BP-75-R1]

$$E(T)=E(25)\underbrace{\left(\frac{F_T^2}{F_{25}^2}\right)}_{A}\underbrace{\left(\frac{1}{1+\alpha_l(\Delta T)}\right)}_{B}$$

Temperature (T) (°C)	A (GPa)	B	$E(T)$ (GPa)	$\frac{E(T)}{E(25)}$
25	60.4	1.0000	60.4	1.00
50	60.2	.9998	60.2	.99
75	60.0	.9997	60.0	.99
100	59.8	.9996	59.7	.98
125	59.6	.9995	59.5	.98
150	59.4	.9993	59.3	.98
175	59.1	.9992	59.0	.97
200	58.9	.9991	58.8	.97
225	58.7	.9989	58.6	.97
250	58.5	.9987	58.4	.96
275	58.4	.9986	58.3	.96
300	58.1	.9984	58.1	.96
325	58.0	.9983	57.9	.95
350	57.8	.9980	57.7	.95
375	57.6	.9979	57.5	.95
400	57.4	.9977	57.3	.94
425	57.3	.9974	57.2	.94
450	56.9	.9972	56.7	.93
475	56.7	.9970	56.6	.93
500	56.6	.9969	56.4	.93
525	56.3	.9962	56.1	.92
550	56.2	.9960	56.0	.92
575	56.0	.9958	55.8	.92
600	55.8	.9957	55.5	.91
625	55.6	.9952	55.3	.91
650	55.4	.9950	55.1	.91
675	55.1	.9948	54.8	.90
700	54.8	.9946	54.5	.90
725	54.3	.9937	54.0	.89
750	53.9	.9935	53.6	.88
775	53.2	.9932	52.8	.87
800	52.8	.9930	52.4	.86
825	52.3	.9928	51.9	.85
865	51.6	.9924	51.2	.84

Inspection of these values reveals that the temperature dependence of the Young's modulus for Hawaiian olivine tholeiite is very nearly linear over the interval 25–700 °C and accords with expectations based on the single-crystal $d(C_{ij})/dT$ for forsterite (Graham, 1969) or bronzite (Frisillo, 1972), or the predictions of lattice dynamics (Leibfried and Ludwig, 1961). Departures in linearity in $E(T)$ have been detected above 700 °C. Examination of the source of this change in slope suggests the presence of the glass transition.

MEASUREMENTS OF THE THERMAL EXPANSIVITY OF BASALT

An accurate evaluation of the temperature-dependent dynamic Young's modulus and dynamic rigidity requires a correction for the effects of thermal expansion within the resonating sample. Thermal expansivity is itself, however, a function of temperature, as the anharmonic vibrations within crystal lattices and within SiO_4 and

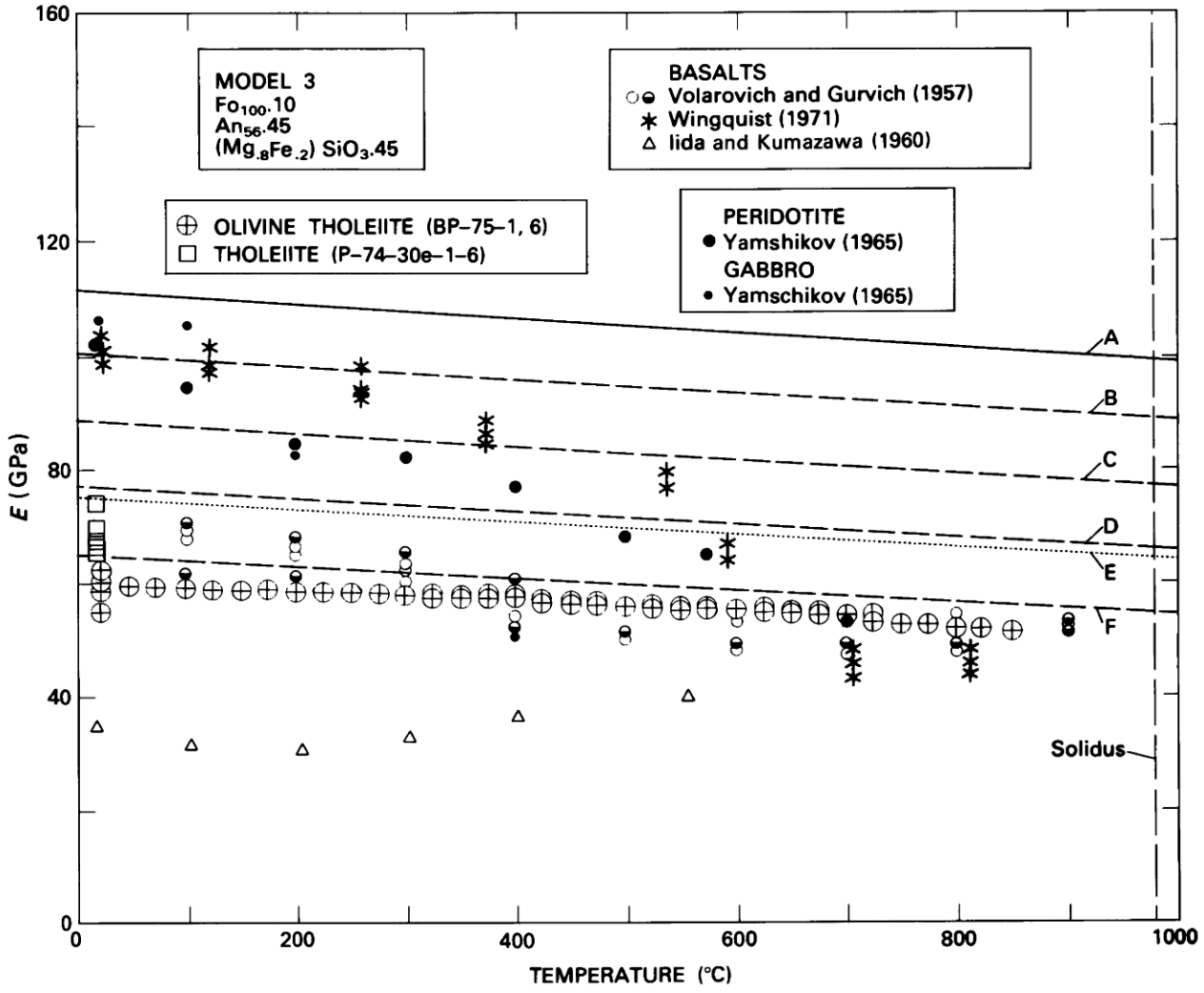

FIGURE 52.6.—High-temperature, ambient-pressure Young's modulus of Hawaiian olivine tholeiite. Available literature data have been included. Squares at 22 °C are data for moduli of Pomona basalt, Selah, Washington. Solid line (A) represents nonflawed computed modulus, without weakening effects of spherical voids (vesicles). Lines B, C, D and F represent progressive increments of 5, 10, 15, and 20 percent voids, respectively. Separation between curves D and E represents addition of 1 volume percent needle-shaped voids, simulating a class of microcracks that occur along crystal junctions. Computed and measured temperature derivatives of E, dE/dT, compare favorably.

AlO_4 tetrahedra in the glass progressively increase in amplitude with temperature.

The objective of this section is to discuss the measurement of linear thermal strain in basalt that will permit the evaluation of linear thermal-expansion coefficients. At the same time, they provide temperature-dependent correction factors that may be applied in the evaluation of the shear modulus and Young's modulus in the same basalt.

Thermal-expansion correction factors were generated by measuring the linear thermal strain by dilatometric methods and by relating incremental changes in longitudinal strain to the change in temperature that produced them. This set of thermal-expansion correction factors covers the temperature range 25–900 °C. The linear expansion coefficients embody within them several expansion components, which involve crystalline and glassy phases in the rock matrix as well as planar voids that heal as temperatures rise (that is, a microstructural component that is temperature dependent).

EXPERIMENTAL PROCEDURE

High-temperature measurements of thermal expansivity were obtained using an Orton Automatic Recording Dilatometer. A schematic diagram of the dilatometer is shown in figure 52.7; it consists of a 25-cm-diameter by 50-cm-long stainless-steel-clad furnace. An alumina sample holder and pushrod house the sample and transmit sample-length changes to a Daytronic (02B600) linearly variable differential transformer (LVDT). A Daytronic (201B) transducer exciter-demodulator produced a dc millivoltage for a Houston Omnigraphic (HR-100) x-y recorder. The x-y recorder automatically plotted sample macroscopic strain and temperature during heating (and cooling) cycles.

Samples were prepared by diamond-barrel coring with a 0.40-in.-inner-diameter core barrel. The sample diameter was 1.01 cm, and the sample lengths were 5.08 ± 0.002 cm. Sample ends were cut square and then ground flat, using an abrasive wheel and lapping grit normally used in preparing standard petrographic thin sections. One end of the sample was slightly beveled to ensure a single contact point against the alumina pushrod of the LVDT.

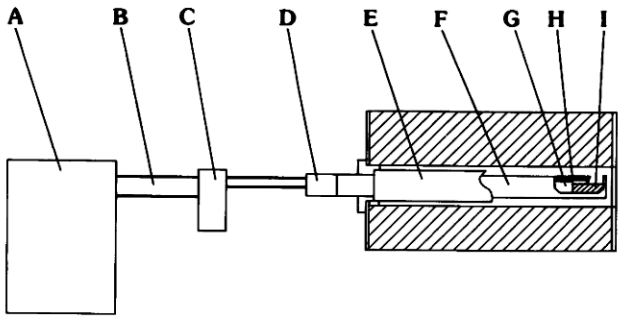

FIGURE 52.7.—Schematic diagram of components in dilatometer assembly used for measurements of linear strain at high temperatures. (A) x-y recording unit; (B) thermocouple leads and LVDT leads; (C) transducer exciter-demodulator; (D) linearly variable differential transformer (LVDT); (E) silicon-carbide resistance heating element; (F) alumina sheath; (G) alumina pushrod assembly; (H) platinum-platinum·10 percent rhodium (Pt-Pt·10Rh) thermocouple; (I) sample.

Dilatometer calibration was done using single crystals of α-quartz as comparators.

Linear thermal-expansion coefficients were evaluated from the defining relation

$$\alpha_l = \frac{1}{l_0}\left(\frac{\Delta l}{\Delta T}\right), \tag{18}$$

and volume coefficients taken as

$$\alpha_V \cong 3\alpha_l. \tag{19}$$

Operation of the dilatometer consisted of placing the machined sample in a split-cylinder alumina cradle whose inside diameter was slightly larger than the sample diameter, thus providing horizontal support while minimizing contact friction during expansion. The flat-cut sample end was placed square against the stop block (stationary end of cradle), and the slightly beveled end contacted the center of the pushrod. Temperature measurements were made with a platinum-platinum·10 percent rhodium (Pt-Pt·10Rh) thermocouple. A slight flexure in the thermocouple shank maintained a constant contact between the thermocouple bead and the upper surface of the sample. The millivoltage outputs of the LVDT and the thermocouple were supplied to an x-y plotter that provided a continuous record of sample-length changes with changing temperature.

LINEAR-STRAIN AND THERMAL-EXPANSION COEFFICIENTS

In contrast with the expansivity of samples of basalt from Kilauea Iki lava lake—where α_v values reached 55×10^{-6} °C^{-1} above 850 °C—expansion above 700 °C does not have a marked component ascribed to the configurational mobility within the glass. This contrast is attributed to the relatively small volume of glass (13 percent) in the Boiling Pots rocks. Ryan and Sammis (1981) discuss the glass transition in basalt and its mechanical significance in regulating the evolution of the fracture front during thermal-stress-induced cracking.

Table 52.5 contains the mean linear coefficients, α_l, for eight replicates and their standard deviation values to 700 °C. Note that variation is highest at low temperatures, lowest at moderate temperatures, and rises again at the 700-°C level. This variation suggests that the progressive closure of randomly oriented microcracks is an important contribution to the aggregate thermal-expansion coefficient below 300 °C and that the minimum variation above 300 °C (but below 700 °C) is reflective of the intrinsic variation in the Boiling Pots basalt expansivity. The larger variation at higher temperatures is interpreted as differences brought about by random differences in the number of olivine phenocrysts from sample to sample. Figure 52.8 illustrates the linear strain produced in basalt samples by controlled heating programs to 925 °C. Figure 52.9 presents the linear and volume thermal-expansion coefficients.

Data on the expansivity of forsterite, augite, and labradorite at 20, 400, and 800 °C (Skinner, 1966) have been employed to form

TABLE 52.5.—*Mean linear thermal-expansion coefficients ($\bar{\alpha}_l$) for basalt of Boiling Pots*

[Mean values determined from samples BP-75-2, BP-75-3, BP-75-4, BP-75-8, BP-75-10, BP-75-11, BP-75-12, BP-75-13]

Temperature (T) (°C)	$\bar{\alpha}_l$ ($\times 10^{-6}$) °C^{-1}	Standard deviation
100	4.58	1.05
200	5.60	1.06
300	4.90	.65
400	6.52	.75
500	7.01	.58
600	7.43	.32
700	7.93	.821

aggregate volume thermal-expansion coefficients for model aggregates by making use of relations for the expansivity of a mixture:

$$\alpha_V = \frac{1}{V}\sum_{i=1}^{n} x_i v_i \alpha_i, \tag{20}$$

where x_i is the volume fraction of mineral i, v_i is the molar volume of mineral i, α_i is the expansion coefficent of mineral i, and V is the aggregate volume, given by

$$V = \sum_{i=1}^{n} x_i v_i.$$

Molar volumes are available in Robie and Waldbaum (1968) and Robie and others (1978). For a model composition of $Fo_{75} = 0.10$, augite $= 0.45$, $An_{64} = 0.45$, $\alpha^l_{20} = 5.07 \times 10^{-6}$ °C^{-1}, $\alpha^l_{400} = 6.53 \times 10^{-6}$ °C^{-1}, and $\alpha^l_{800} = 8.49 \times 10^{-6}$ °C^{-1}, where the subscripts refer to degrees Celsius. Comparison of these

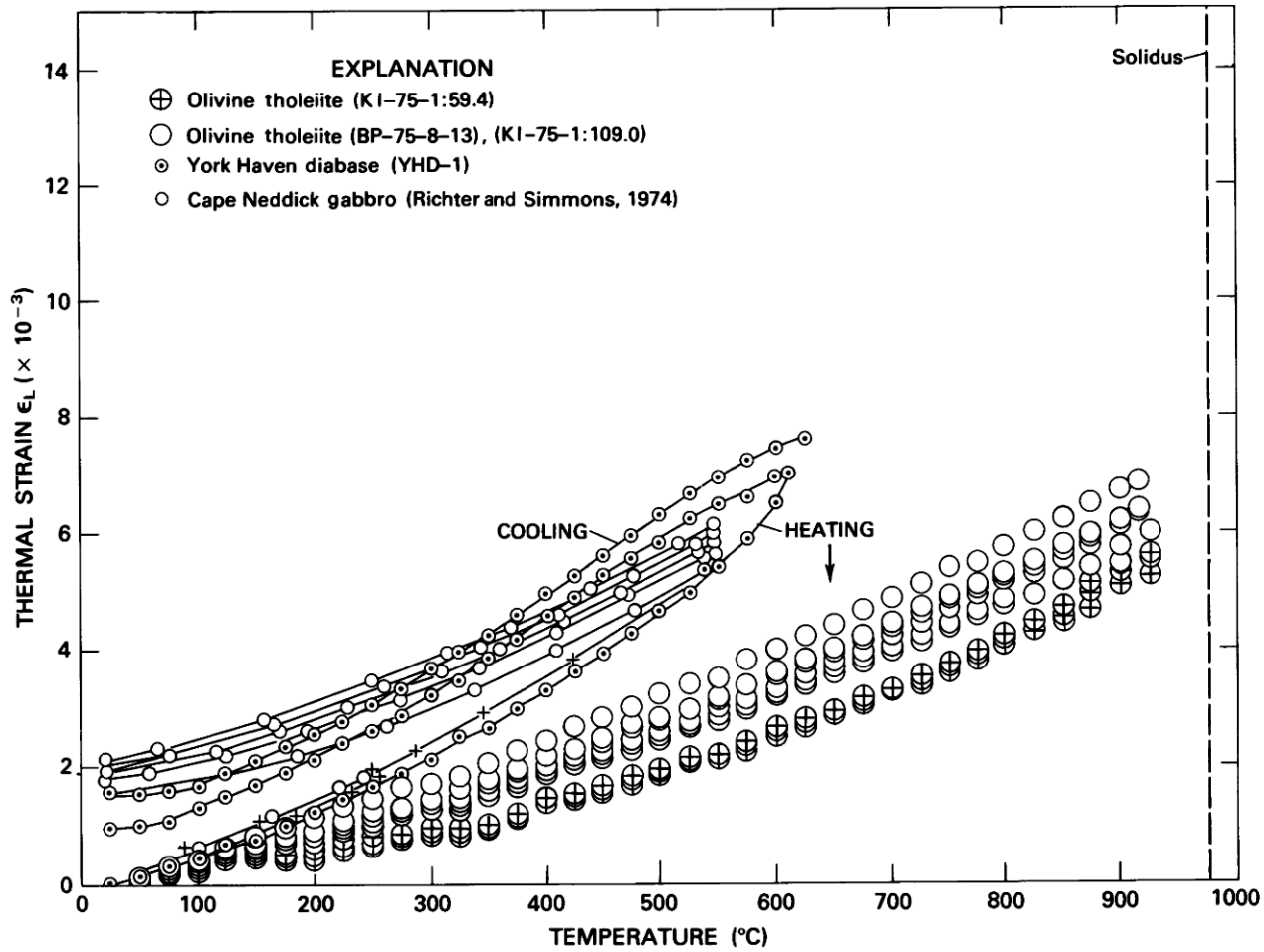

FIGURE 52.8.—Linear strain in olivine tholeiite from Boiling Pots and Kilauea Iki lava lake, Hawaii (open circles from 109-ft level of drill hole KI-75-1 and crossed circles from 59.4-ft level of drill hole KI-75-1). Expansivity has been evaluated from dilatometer measurements made during heating portion of experiment, to minimize contribution of microfractures to α_l. Cyclic runs on York Haven diabase have induced a nonrecoverable strain due to microcracking; this data is superposed on results of Richter and Simmons (1974) for comparison. Each successive cooling cycle has opened a new generation of microfractures, as suggested by progressive temperature-thermal strain hysteresis in heating and cooling curves.

values with the α_l values in table 52.5 shows that the expansivity of Boiling Pots rocks climbs in asymptotic fashion to meet the trend of the model composition. For both the rock and model, expansions from 325 to 700 °C are similar, suggesting that a 300-°C temperature excursion is required for preexisting microcracks to close and the full intrinsic expansivity to become dominant. Above 300 °C, the comparison between the predicted and experimental results is excellent.

CYCLIC EXPANSIVITY AND IRREVERSIBLE THERMAL STRAIN

Experiments have been conducted using cyclic heating and cooling programs, during which the instantaneous sample length has been continuously monitored. These experiments have used the Orton Automatic Recording Dilatometer as configured in the discussion above. In the broadest sense, the experiments have been motivated to develop a qualitative feeling for the ways in which cyclic heating by intrusive bodies (in the near-surface environment) might generate microfractures—of considerable relevance to the discussions in the section "Pressure Dependence of Elasticity in Hawaiian Basalt: Contractancy and Magmatism."

The experiments have been designed to test the following propositions:

(1) For Hawaiian basalt, what are the expansivity effects of cyclic thermal histories?

(2) What proportions of the expansions and contractions are reversible, and how much is irreversible?

(3) What are the mechanical differences in repetitive cycling to the same maximum temperature and in cycling to successively higher temperatures?

(4) Are there essential differences between the cyclic expansivity of porous and nonporous igneous rocks, as exemplified by samples of basalt and diabase?

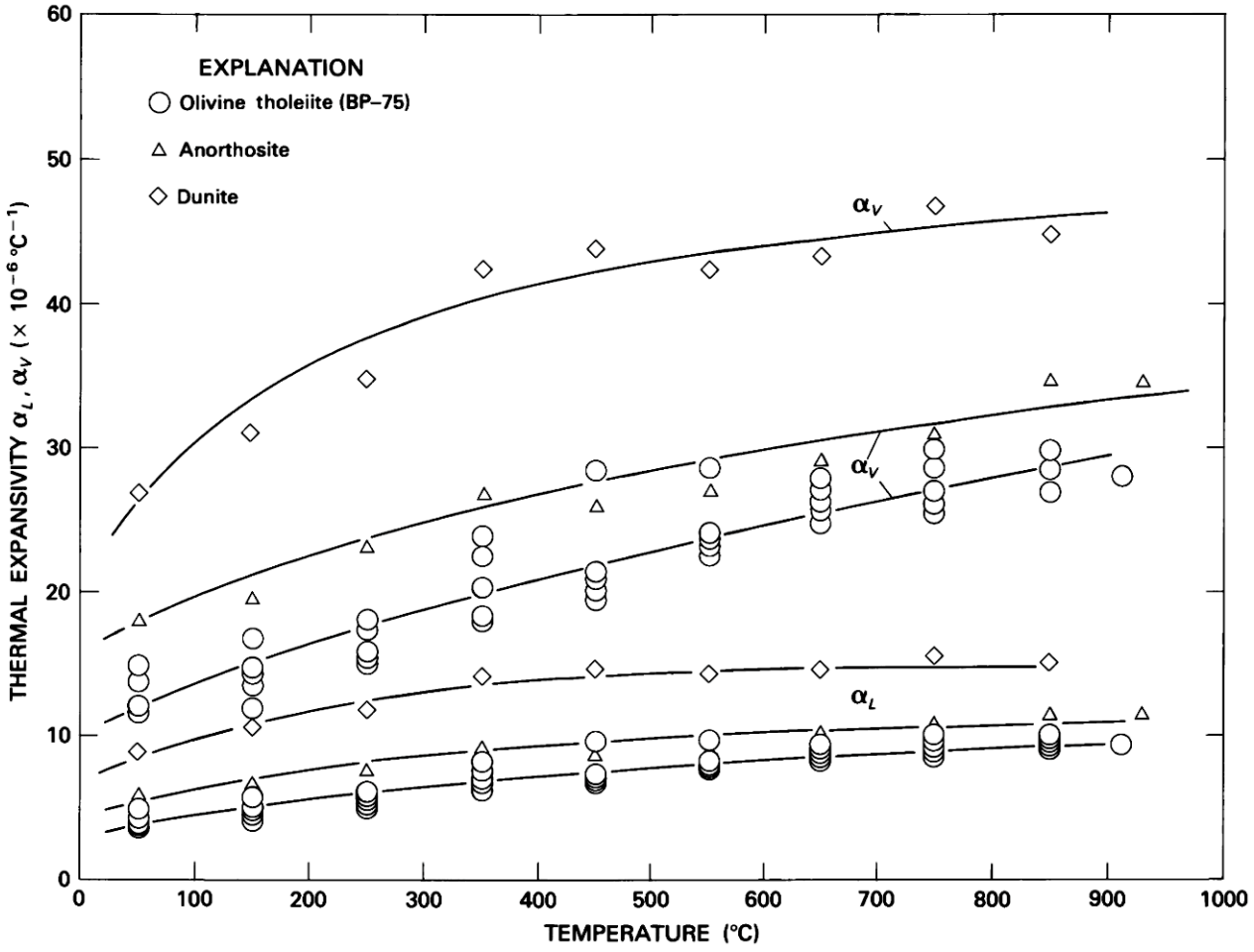

FIGURE 52.9—Linear (α_L) and volume (α_V) thermal-expansion coefficients for olivine tholeiite from Boiling Pots. Dunite and anorthosite expansivities provide comparisons.

Figure 52.10 illustrates the behavior of basalt during a series of heating and cooling cycles to 950 °C. The experiments were performed on olivine tholeiite from the Boiling Pots with a modal mineralogy as shown in table 52.1 and a porosity level of 15 percent. The heating rate was 3 °C min^{-1}, and the cooling rate was determined by the thermal inertia of the furnace at its natural cooling rate. The expansivity-temperature plot has been subdivided into a field of volume increase (as inferred by the sample-length change, in percent) and a field of volume decrease. The line dividing these two fields is the ambient-temperature initial-reference length, l_0. The curves show the following features. (1) The cooling portion of a cycle does not retrace the heating portion but lies beneath it, producing a loop that indicates hysteresis in sample volume and irreversible thermal strain. The separation of the curves at ambient temperature is a measure of the nonrecoverable strain induced within a cycle and between cycles. At the conclusion of cycle 1, the irreversible length change is approximately 0.4 percent, for example. (2) Successive cycles to the same maximum temperature (950 °C) accumulate successive increments of irreversible thermal strain. These increments move continuously in the direction of a net contraction in length. The hysteresis in thermal strain produced by temperature increases and the contraction in sample dimensions that accompanies cooling to ambient temperatures suggest thermally induced changes in the microstructure. Compatible with this behavior is the inferred production of microcracks during heating and the densification induced by the rupture of micropore and vesicle-vesicle bridges (microcrack-induced) during cooling and contraction. The experiments suggest that measurements of elastic moduli taken during heating-cooling cycles would similarly display a hysteresis in behavior—producing, for example, values of K, μ, and E that would not retrack upon

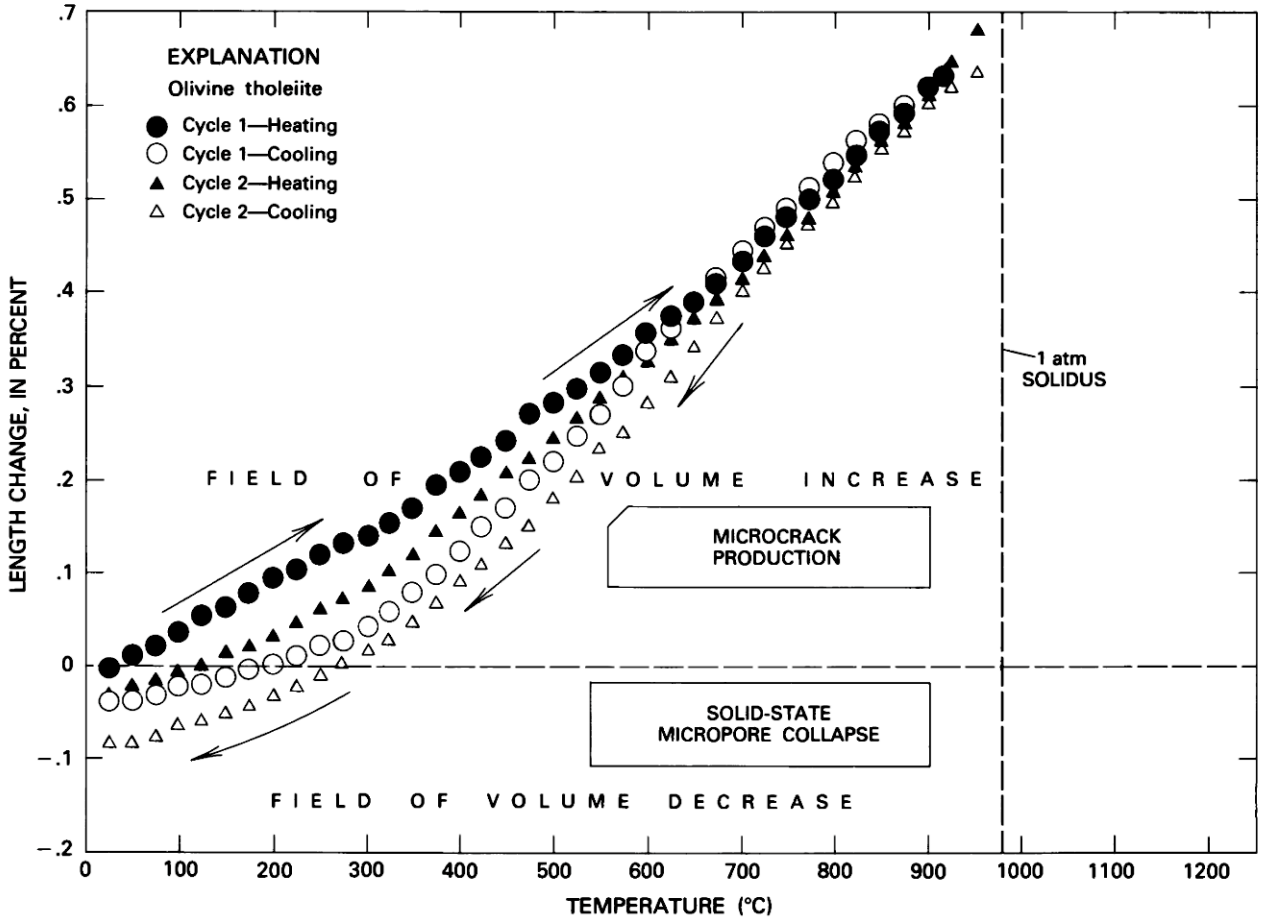

FIGURE 52.10.—Expansivity of Hawaiian olivine tholeiite during cyclic heating and cooling. Solid symbols track change in sample dimensions (length) accompanying heating, whereas open symbols record cooling path within a given cycle. For porous basalt, net effect of cycles to 950 °C, is a reduction in sample length, thus suggesting that microfractures induced during heating have bridged crystal + glass matrix between vesicles, thereby allowing incremental micropore collapse during contraction produced by subsequent cooling portion of a cycle. Contrasting behavior is demonstrated by irreversible length changes produced by microcracking in completely crystalline and nonporous intrusive rocks, as exemplified by diabase in figure 52.11.

cooling those determined during heating. This behavior would qualitatively accord with the results of Ide (1937), who found reductions in the velocity of sound in samples of diabase and norite heated to 700 °C in experiments in which the maximum temperature was raised in successive cycles. Such a program of cyclic elastic-moduli measurements with cooling as well as heating experiments has not been undertaken in this study, and it remains to be determined what, for example, the variance in the Young's modulus or the rigidity induced by, for example, the 0.4-percent change in sample length produced by heating to 950 °C would be after returning the sample to ambient temperature. Note, however, the difference between the net irreversible effects produced in the Ide (1937) samples and those in the olivine tholeiite: the former increasing their dimensions via inferred microcrack production only, and the latter undergoing a decrease in dimension attributed to solid-state densification during micropore collapse. Under confining pressure, we would therefore expect a slight increase in basalt moduli reflecting the sample-volume reduction.

Contrasting with the mechanical behavior exhibited by olivine tholeiite in the heating-cooling cycles is that of diabase, as suggested above. Further evidence of this contrast is provided in figure 52.11, which shows the expansivity of diabase cycled between ambient temperature and 625 °C at a heating rate of 3 °C min^{-1}. As before, thermal-strain/temperature hysteresis loops have been induced by the inferred production of microcracks in the sample during heating. But note the very different signature of this hysteresis: the opening of the loops is produced by an irreversible length increase (consistent with inferred lower elastic moduli), as contrasted with a loop opening

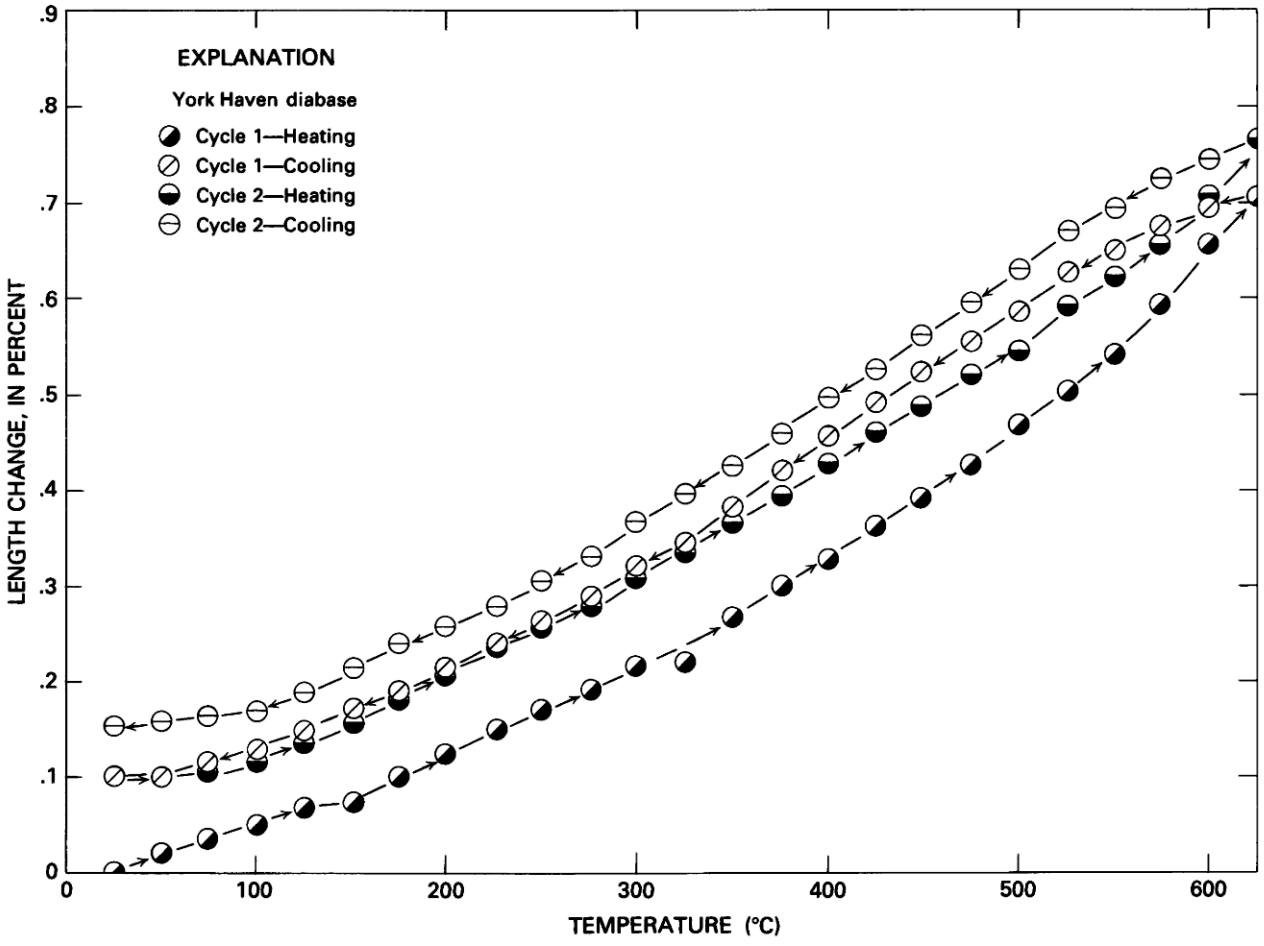

FIGURE 52.11.—Expansivity of diabase during cyclic heating and cooling. Half-filled symbols track change in sample dimensions (length) accompanying heating, whereas open symbols record cooling path within a given cycle. Arrows between data points indicate movement to higher or lower temperatures. For nonporous and holocrystalline intrusives such as diabase, excursions to 625 °C induce microfractures that do not close reversibly upon cooling. Each excursion to high temperatures induces a new generation of microcracks and an additional increment of irreversible dimension change. All cycling is associated with increased sample volume, contrasting with behavior of porous olivine tholeiite (figure 52.10).

induced by length decreases (suggesting higher elastic moduli). Other aspects of the effects of heating-cooling cycles remain qualitatively similar, although the direction in which they move again contrasts with the basalt: successive excursions to high temperature induce progressive increments of irreversible (positive) thermal strain. Thus, sample volumes progressively increase in response to the microstructural changes induced by internal cracking.

Finally, how do the effects of (1) repetitive cycling to the same maximum temperature (T_{max}) and (2) cycling to successively higher values of T_{max} differ? Figure 52.12 draws heavily on the work of Richter and Simmons (1974) and adds to that the results of experiments of type (1) and type (2). For the York Haven diabase, raising the T_{max} to 800 °C (from 610 °C) in three successive increments produces three successive generations of new microcracks and, in turn, three distinctly new levels of thermal strain. On the fifth cycle, the T_{max} is maintained at the same level (800 °C), and, by inference, relatively few new microcracks have been generated, producing only a modest increment of irreversible strain. In an experiment of type (1), the same T_{max} is maintained throughout, producing successive generations of new microcracks with progressively smaller populations. This result accords with the results of Richter and Simmons (1974), who found limiting levels of microstructural damage with large numbers of cycles to the same maximum temperature. In turn, this result suggests that a damage threshold exists that is capable of accommodating successive thermal-deformation cycles through internal shock absorbers made up of assemblages of preexisting microcracks. Accommodating higher levels of thermal strain requires the excursion to significantly higher temperatures, initiating a new round of microcrack production. Simply revisiting the same old T_{max} is insufficient to significantly increase this microcrack population.

MODELING THE HIGH-TEMPERATURE ELASTICITY OF BASALT

In this section, a model for estimating the elastic moduli of basalt is developed. It has been motivated by the desire to construct and apply an approach for computing the ambient and high-temperature moduli, thus providing theoretical guidance for the temperature dependence of the Young's modulus and the rigidity evaluated in the experiments. This modeling therefore forms a complementary companion to the experimental work and has been motivated by the measurements themselves. The primary focus of the modeling is in developing tools for evaluating the temperature dependence of the rigidity ($\mu(T)$) and the Young's modulus ($E(T)$).

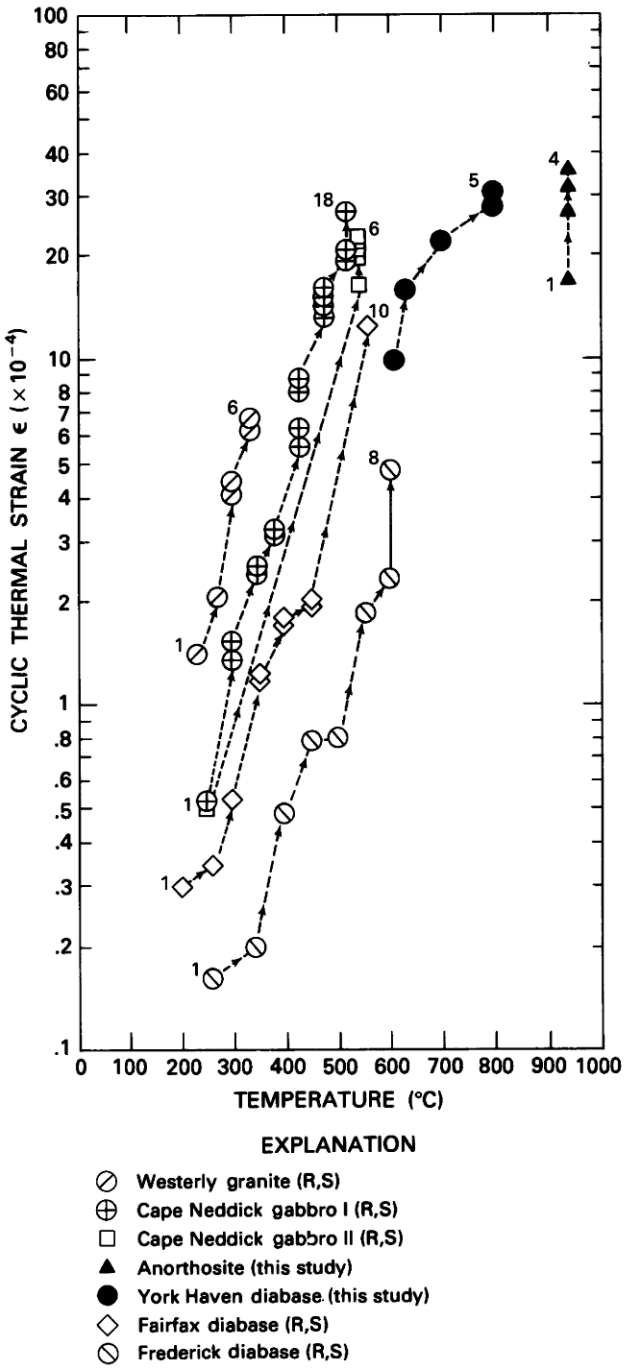

FIGURE 52.12.—Thermal strain-temperature plot of holocrystalline rocks having cyclic heating-cooling thermal histories. Numbers at side of lithologic symbols indicate cycle number within an experimental series; first and last cycle numbers have been labeled. Arrowed pathways indicate temperature (maximum) and correlative thermal strain, through a succession of excursions to high temperatures. For successive cycles to same maximum temperature (symbols line up vertically) relatively small amounts of additional irreversible strain are produced, suggesting diminished production of internal microfractures. Successive excursions to higher levels of temperature (diagonal pathways) induce additional irreversible strain and, by inference, a new generation of thermal microfractures. Samples (Richter and Simmons, 1974) run to maximum temperatures of 600 °C. Experimental comparative runs from the study of Richter and Simmons (1974) are designated (R, S) in the figure explanation.

In the modeling, the temperature range of concern is 25 °C to the solidus for Hawaiian tholeiite (980 ± 5 °C). The rock is assumed to be unconfined, and pressure is not, at this point, a variable. The role of pressure will be discussed in the section "Pressure Dependence of Elasticity in Hawaiian Basalt: Contractancy and Magmatism," with reference to in-situ contractancy.

The model has been divided into two submodels, the first treating compositional effects, and the second one dealing with microstructure. Solids that contain no weakening flaws have elastic properties that are dictated by their composition and their temperature. A compositional model is developed to account for these two contributions to aggregate elasticity. The presence of weakening flaws reduces the moduli that would otherwise result in a pristine solid. A microstructural model has been coupled to the compositional model to account for these effects. Roman numerals have been suffixed to each model to help distinguish one from the other. The compositional model (I) and the microstructural model (II) are shown in figure 52.13.

COMPOSITIONAL MODEL (I)

VOIGT, REUSS, AND HILL AVERAGING SCHEMES AND EFFECTIVE ELASTIC MODULI OF A POLYCRYSTALLINE AGGREGATE

The elastic properties of single crystals of olivine (orthorhombic), augite (monoclinic), and plagioclase (triclinic) are functions of direction within the lattice. To construct a compositional model of basalt elasticity by combining single-crystal elastic data, we need a means of averaging the directional moduli over all orientations and thereby producing a solid that is elastically isotropic in a macroscopic sense. Two averaging methods have been used to effect polycrystalline elasticity from single-crystal data, and they provide, through their assumptions, an upper (Voigt, 1928) and a lower (Reuss, 1929) bound to the aggregate elastic moduli.

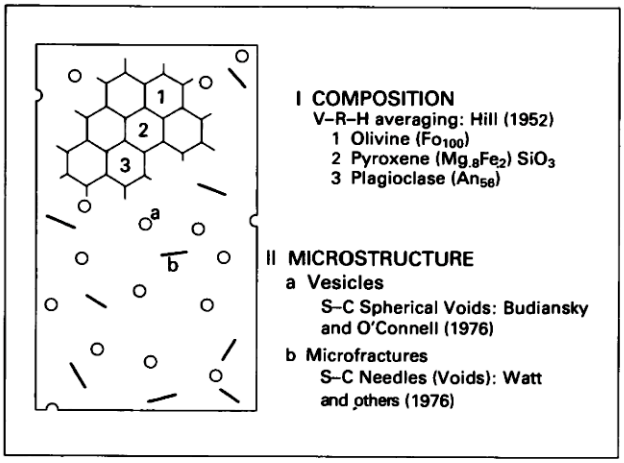

FIGURE 52.13.—Model for high-temperature elasticity of basalt. Compositional submodel I combines contribution of mineral phases (1, 2, 3) to aggregate K, μ, and E by combining single-crystal elastic constants in a Voigt-Reuss-Hill averaging scheme for mixtures. Compositional submodel generates magnitude of modulus and predicts overall temperature dependence by combining temperature derivatives for all component phases. Microstructural submodel II incorporates effects of weakening flaws on moduli. Vesicles (a) formed during posteruption degassing of melt are simulated by spherical voids; microfractures (b) formed between crystals during subsolidus cooling are simulated by needle-shaped voids.

Assuming that the strain distribution in a polycrystalline aggregate was uniform and constant, Voigt (1928) derived an effectively isotropic bulk and shear modulus by averaging the single-crystal stiffnesses over all orientations. This approximation, which requires that the microscopic strain in component grains be equal throughout the matrix and equal to the macroscopic strain of the aggregate, results in a disequilibrium of forces between individual crystals. The bulk modulus (K_V) of Voigt (1928) is expressed in terms of the single-crystal elastic-stiffness coefficients, C_{ij},

$$K_V = \tfrac{1}{9}[(C_{11}+C_{22}+C_{33})+2(C_{12}+C_{23}+C_{13})], \quad (24)$$

whereas the rigidity (μ_V) is given by

$$\mu_V = \tfrac{1}{15}[(C_{11}+C_{22}+C_{33})-(C_{12}+C_{23}+C_{13}) + 3(C_{44}+C_{55}+C_{66})]. \quad (25)$$

Assuming that the stress distribution in the aggregate was uniform and constant, Reuss (1929) derived an effectively isotropic bulk and shear modulus by averaging single-crystal compliances over all orientations. This approximation, which requires that the microscopic stresses between component crystals be equal throughout the matrix and equal to the macroscopic stress, produces distorted grains that no longer fit together (that is, compatibility is violated).

The bulk modulus (K_R) derived by Reuss (1929) is in turn expressed in terms of the single-crystal elastic-compliance coefficients, S_{ij},

$$\frac{1}{K_R} = [(S_{11}+S_{22}+S_{33})+2(S_{12}+S_{13}+S_{23})], \quad (26)$$

and the rigidity (μ_R) by

$$\frac{1}{\mu_R} = \tfrac{4}{15}[(S_{11}+S_{22}+S_{33})-(S_{13}+S_{12}+S_{23}) + \tfrac{3}{4}(S_{44}+S_{55}+S_{66})+S_{33}]. \quad (27)$$

Hill (1952) has demonstrated that the Voigt and Reuss moduli are, in fact, upper and lower bounds on K and μ—a result of the assumptive extremes of constant strain and stress, respectively. Hill suggested that a more appropriate measure of aggregate elasticity would lie between these extremes and proposed using an average of the Voigt and Reuss schemes. This intermediate measure is known as the V-R-H average (or simply the Hill average) and is given by

$$K_{VRH} = \tfrac{1}{2}(K_V + K_R) \quad (28)$$

and

$$\mu_{VRH} = \tfrac{1}{2}(\mu_V + \mu_R). \quad (29)$$

The separation between the Voigt and Reuss bounds for an aggregate is thus a measure of the crystal anisotropy within the aggregate, and $K_V = K_R = K$ for an elastic isotropic substance.

STRUCTURE OF THE COMPOSITIONAL MODEL

The high-temperature bulk modulus and shear modulus for the polyphase mixture, given by Graham and Dobrzykowski (1976), are

$$K(T) = K(25) + \left(\frac{\partial K}{\partial T}\right)\Delta T, \tag{30}$$

and

$$\mu(T) = \mu(25) + \left(\frac{\partial \mu}{\partial T}\right)\Delta T, \tag{31}$$

where $\Delta T = (T - 25)$ in degrees Celsius.

To compute the upper and lower bounds on (30) and (31), the Voigt-averaged and Reuss-averaged moduli for a polyphase mixture are applied.

The upper and lower bounds on the temperature derivatives of the bulk modulus and the shear modulus are computed by applying the appropriate relations for a polyphase mixture.

The Hill-averaged moduli are then evaluated from the averages of the upper and lower bounds for the mixture:

$$K(T)^{\mathrm{MIX}}_{\mathrm{VRH}} = \tfrac{1}{2}[K(T)_V + K(T)_R], \tag{32}$$

and

$$\mu(T)^{\mathrm{MIX}}_{\mathrm{VRH}} = \tfrac{1}{2}[\mu(T)_V + \mu(T)_R]. \tag{33}$$

For an evaluation of the Young's modulus (E) at high temperatures, the standard relation (for example, Birch, 1960) is used:

$$E(T)^{\mathrm{MIX}}_{\mathrm{VRH}} = \frac{9K(T)^{\mathrm{MIX}}_{\mathrm{VRH}} \cdot \mu(T)^{\mathrm{MIX}}_{\mathrm{VRH}}}{3K(T)^{\mathrm{MIX}}_{\mathrm{VRH}} + \mu(T)^{\mathrm{MIX}}_{\mathrm{VRH}}}. \tag{34}$$

For high-temperature upper and lower bounds on the Young's modulus, $K(T)_{\mathrm{VRH}}$ and $\mu(T)_{\mathrm{VRH}}$ in (34) are replaced by $(K(T)_V, \mu(T)_V)$ and $(K(T)_R, \mu(T)_R)$, respectively.

COMPOSITIONAL SUBMODELS

The compositional model employs olivine, clinopyroxene, and plagioclase as matrix components. Three compositional submodels have been formed by varying the volume fractions of component minerals. These submodels are referred to as submodel 1, submodel 2 and submodel 3, and their volume fractions are listed in table 52.6.

Submodel 3 was intended to represent an average basalt, whereas submodels 1 and 2 were intended to represent compositional bounds on basalt elasticity by employing relatively pyroxene-rich (hard matrix) and plagioclase rich (soft matrix) mineralogies. It is expected that submodels 1 and 2 would provide upper and lower bounds on aggregate elastic moduli. They enclose the elastic behavior of a submodel 3 aggregate.

TABLE 52.6.—*Compositional submodels for basalt elasticity*

[Values represent volume fractions]

Component	Submodel 1	Submodel 2	Submodel 3
Olivine Fo_{100}	0.10	0.10	0.10
Pyroxene $(Mg_{0.8}Fe_{0.2})SiO_3$	.60	.20	.45
Plagioclase An_{56}	.30	.70	.45

OLIVINE

Olivine has been incorporated in the model by using the zero pressure, 298 K elastic stiffness and compliance coefficients of forsterite and the temperature derivatives of the bulk modulus and rigidity as reported by Graham and Barsch (1969) and presented by Graham (1969).

PYROXENES

The contribution of pyroxene employs the zero-pressure, 298 K data of Ryzhova (1964) for augite. These data permit pyroxene to be included in aggregate moduli calculations for ambient temperature. Temperature derivatives of the elastic coefficients for augite are not available. For high-temperature calculations, the temperature derivatives for the orthopyroxene bronzite, $(Mg_{0.8}Fe_{0.2})SiO_3$, have been used (Frisillo, 1972).

PLAGIOCLASE

The role of plagioclase in basalt elasticity has been incorporated by employing the results of Aleksandrov and others (1964) as reported for the zero pressure moduli of An_{56} evaluated at 298 K. Data on the temperature dependence of the elastic constants for the plagioclase feldspars is virtually nonexistant. An approximation of this dependence is therefore required. The relatively open structure of α-quartz suggests that the temperature derivatives of the elastic moduli of its framework may approximate the temperature induced changes in the open framework of plagioclase (E.K. Graham, oral commun.). This substitution has been adopted.

The Voigt- and Reuss-averaged bulk and shear moduli for An_{56} based on the Aleksandrov and others (1964) data and reported in Simmons and Wang (1971) are listed in table 52.7.

MICROSTRUCTURAL MODEL (II)

The primary modulus-reducing agents in a basalt microstructure are vesicles and thermally induced microcracks. Though expressions are provided for incorporating both vesicles and microfractures (where needle shaped), the primary objective has been to simulate the effect of vesicles in weakening the otherwise pristine solid. Thin-section petrography and scanning-electron microscopy has demonstrated that vesicles account for most of the porosity in basalt. Including the mechanical effects of vesicles and microcracks in basalt elasticity has been accomplished by incorporating approximations for the elastic contributions of spherical voids and needle-shaped voids by making use of the self-consistent approximation of Hill (1965) and Budiansky and O'Connell (1976), as presented by Watt and others (1976).

TABLE 52.7.—*Compositional-model input properties and derived interim Voigt and Reuss bulk moduli and rigidities*

[Reference in parentheses]

Parameter	Fo_{100}		Augite		An_{56}		Units
V_i	43.79	(2)	66.09	(4)	100.52	(2)	$cm^3\ mol^{-1}$
ρ_i	3.221	(1)	3.320	(5)	2.69	(7)	$g \cdot cm^{-3}$
M_i	140.708	(2)	216.56	(4)	272.44	(2)	$g \cdot mol^{-1}$
K_i^v	1,311.9	(1)	1,048.0	(5)	753	(7)	kbar
K_i^r	1,268.8	(1)	1,021.0	(5)	688	(7)	kbar
μ_i^v	831.8	(1)	754.8	(5)	370	(7)	kbar
μ_i^r	801.9	(1)	738.9	(5)	317	(7)	kbar
α_i^p	24.65×10^{-6}	(1)	47.7×10^{-6}	(6)	12×10^{-6}	(8)	$°C^{-1}$
$(dK/dT)_V^i$	−0.173	(1)	−0.275	(3)	−0.10	(9)	kbar $°C^{-1}$
$(dK/dT)_R^i$	−0.178	(1)	−0.261	(3)	−0.10	(9)	kbar $°C^{-1}$
$(d\mu/dT)_V$	−0.134	(1)	−0.120	(3)	−0.015	(9)	kbar $°C^{-1}$
$(d\mu/dT)_R$	−0.138	(1)	−0.119	(3)	−0.015	(9)	kbar $°C^{-1}$

(1) Graham (1969); Graham and Barsch (1969).
(2) Robie and Waldbaum (1968).
(3) Frisillo (1972) values for bronzite.
(4) Robie and Waldbaum (1968) values for diopside.
(5) Aleksandrov and others (1964) data for augite.
(6) Frisillo and Buljan (1972) data for bronzite.
(7) Ryzhova (1964) data for labradorite.
(8) Skinner (1966) data for An_{95} at 20 °C.
(9) V-R-H averaged values for α-quartz from Anderson and others (1968).

SELF-CONSISTENT TREATMENT

Kröner (1958, 1967) expressed the aggregate moduli of an elastic, isotropic polyphase solid in terms of the individual moduli and individual strains of each component, summed over all included phases and added to the moduli of the matrix. Approximating the strain occurring in an isolated inclusion of the i^{th} material embedded in an infinite (and otherwise homogeneous) elastic matrix subject to pure loading (compressive or shear) at infinity and having the as-yet-to-be-determined elastic constants of the total aggregate led to the first self-consistent approximation.

Budiansky (1965) has combined the Kröner (1958, 1967) approach with the exact results of Eshelby (1957), who demonstrated that the strain state of an inclusion in a matrix sheared at infinity is uniform, to derive coupled, implicit expressions for the effective elastic constants of heterogeneous solids. In the Budiansky approach, the exact Eshelby results are used as estimators of the average shear strain in each phase, which, when coupled to the Kröner aggregate moduli expressions, leads to simultaneous equations for the effective shear and bulk moduli in terms of constituent moduli.

STRUCTURE OF THE MICROSTRUCTURAL MODEL

For a two-phase aggregate, the self-consistent approximation for the effective modulus Watt and others, 1976) may be expressed as

$$\frac{M^*-M_1}{M_2-M_1}=V_2\left[1+\frac{V_1(M_2-M_1)}{M_1+f}\right]^{-1}, \qquad (35)$$

where M^* is the effective modulus of the total aggregate (K^* or μ^*), M_1 is the modulus (K_1, μ_1) of the included phase, M_2 is the modulus of the matrix (K_2, μ_2), V_1 is the volume fraction of the included phase, V_2 is the volume fraction of the matrix, and f is a function that is dependent on the moduli of the included phase as well as on the effective aggregate moduli (though not necessarily at the same time). The two phases are (1) voids and (2) matrix. Note that the matrix itself is actually polycomponent and polycrystalline.

The approximation for spherical inclusions of the minor phase is given by (35), such that for effective bulk modulus

$$K^*: \quad f=\tfrac{4}{3}\mu^*, \qquad (36)$$

and for effective rigidity

$$\mu^*: \quad f=\frac{\mu^*(9K^*+8\mu^*)}{6(K^*+2\mu^*)}. \qquad (37)$$

In this treatment, the included phase is the vapor phase that occupies spherical vesicles and is described by $K_1=0$; $\mu_1=0$. The finite bulk modulus and rigidity of the matrix is solely a function of the modal percentage of the component mineralogy (that is, submodel 1, 2, or 3).

The expressions for aggregate moduli are coupled (nonseparable) and are solved by an iterative computational procedure. In general, four to five iterations were satisfactory for convergence, and in no case has more than ten iterations been required.

The approximation for needle-shaped inclusions of the minor phase is given by (35), such that for the effective bulk modulus

$$K^*: \quad f=\tfrac{1}{3}\mu_1+\mu^*. \qquad (38)$$

and for the effective rigidity

$$\mu^*: \quad f=\frac{5}{\dfrac{1}{3(K_1+\frac{1}{3}\mu_1+\mu^*)}+\dfrac{2(2\mu_1+\mu^*+G)}{(\mu_1+\mu^*)(\mu_1+G)}}-\mu_1, \qquad (39)$$

where

$$G=\frac{\mu^*(K^*+\frac{1}{3}\mu^*)}{K^*+\frac{7}{3}\mu^*} \qquad (40)$$

and μ_1, μ^*, K_1, and K^* have been defined above.

The approximation employs air as the included minor phase that occupies the microcracks that open during cooling, and accordingly, $K_1=0$; $\mu_1=0$.

As in the case for spherical inclusions, the microcrack approximations (needles) are solved iteratively for K^* and μ^*. Convergence rates are comparable to the vesicle approximations.

Flat microcracks have not been explicitly considered, but their incorporation is straightforward (see O'Connell and Budiansky, 1974; Watt and others, 1976).

The results of the combined predictions of the compositional model (I) and microstructural model (II) are presented and discussed below, in light of measured $E(T)$, $\mu(T)$, levels of absolute porosity, and compositional details for Hawaiian basalt.

ELASTIC MODELS AND ELASTIC MEASUREMENTS

The $\mu(T)_{VRH}$ for compositional submodels 1, 2, and 3 are presented and compared in figure 52.14. Compositional submodel 3 has the mineralogy that most closely resembles an average basalt composition, as contrasted with submodels 1 and 2, and thus

submodel 3 should be compared with the data. The nonporous moduli are given by solid lines of different weight that correspond to the dashed (porous) moduli for the appropriate model. For a given composition, all five curves ($\phi = 0$, 0.05, 0.10, 0.15, and 0.20) are parallel, indicating no computed porosity-temperature interaction. This relation accords with what one would expect, because porosity has been shown to have a negligible effect on thermal expansivity in solids (Coble and Kingery, 1956). The rapid inflexion of the E(T) curves for the data of Wingquist (1971) suggests that dehydration was occurring in the alteration minerals of their samples over the range 500–700 °C. The samples of Murase and McBirney (1973) and Iida and Kumazawa (1960) did not have a reported characterization that permits an evaluation of the reason(s) they do not exhibit a linear temperature dependence.

The $\mu(T)_{VRH}$ for compositional submodel 3 is shown in figure 52.15, and the evaluated rigidities of the Boiling Pots replicates are indicated by the crossed circles. Using an average value of ϕ for the entire range of measured porosities gives $\phi = 0.166$. This average is a difference of approximately 3.4 percent porosity based on the magnitude of the predicted and measured ambient-temperature rigidity and the corresponding porosity levels.

The distance between the Voigt- and Reuss-averaged bounds for a nonflawed solid (K_1, μ_1, K_2, and μ_2 are finite) is a measure of the differences in moduli for the single-crystal components. The

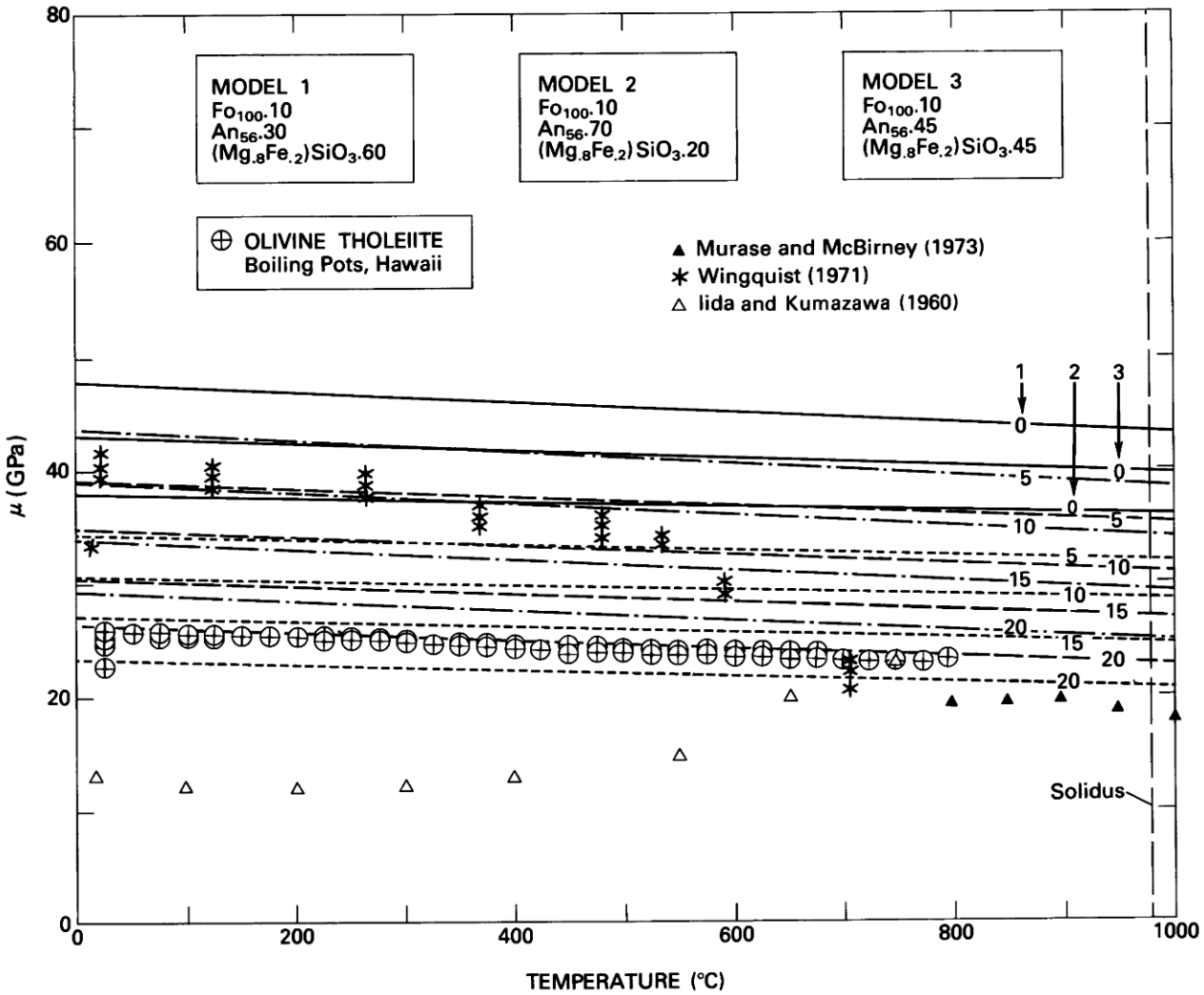

FIGURE 52.14.—Predicted high-temperature, ambient-pressure rigidity for three model basalts (see table 52.6) and rigidity of olivine tholeiite from Boiling Pots. Trends of compositional models without porosity ($\phi = 0$; labeled with 0) are represented by solid lines. Trends of compositional models with varying levels of porosity (labeled 5, 10, 15, 20) are represented by dashed lines for $\phi = 0.05$, $\phi = 0.10$, $\phi = 0.15$, and $\phi = 0.20$ volume fractions of spherical voids, respectively. Bronzite simulates temperature dependence of pyroxenes. Available literature data are included.

V-R-H bounds for the matrix, evaluated at a level of zero porosity, are shown in figure 52.5. This figure illustrates the mineralogical contributions to the model aggregate elasticity.

The Hill-averaged Young's moduli for compositional submodel 3 are presented in figure 52.6 for porosity levels (spherical voids) to $\phi = 0.20$. In addition, the effect of microcracks at dilute concentration are shown (needle-shaped voids) for $\phi = 0.01$. The separation between lines D and E was produced by microcrack additions to an aggregate that already contained 15 percent spherical pores. This addition of microcrack effects produced an additional 1.8-GPa (18-kbar) decrement.

For the temperature-dependent Young's modulus ($E(T)$) replicates evaluated from flexural-frequency measurements of Boiling Pots basalt, the average volume-fraction absolute porosity is $\phi = 0.15$. This value is approximately a 5-percent difference between the porosity value expected, assuming a submodel 3 composition with purely spherical voids, and the determined value.

The temperature dependence of the Hill-averaged bulk modulus, shear modulus, and Young's modulus is presented in table 52.8 for submodel compositions 1, 2, and 3. The highest temperature dependence (largest absolute value) of the moduli on a collective basis is for the pyroxene-rich submodel 1 and is reflective of the relatively large adiabatic temperature derivative of the bulk modulus ($(\partial K/\partial T)^S_{VRH}$) value for bronzite ($-26.8$ MPa/ °C) and, in turn, the relatively high volume thermal expansivity of augite ($47.7 \times 10^{-6}\,°C^{-1}$). Plagioclase-rich submodel 2 shows the lowest

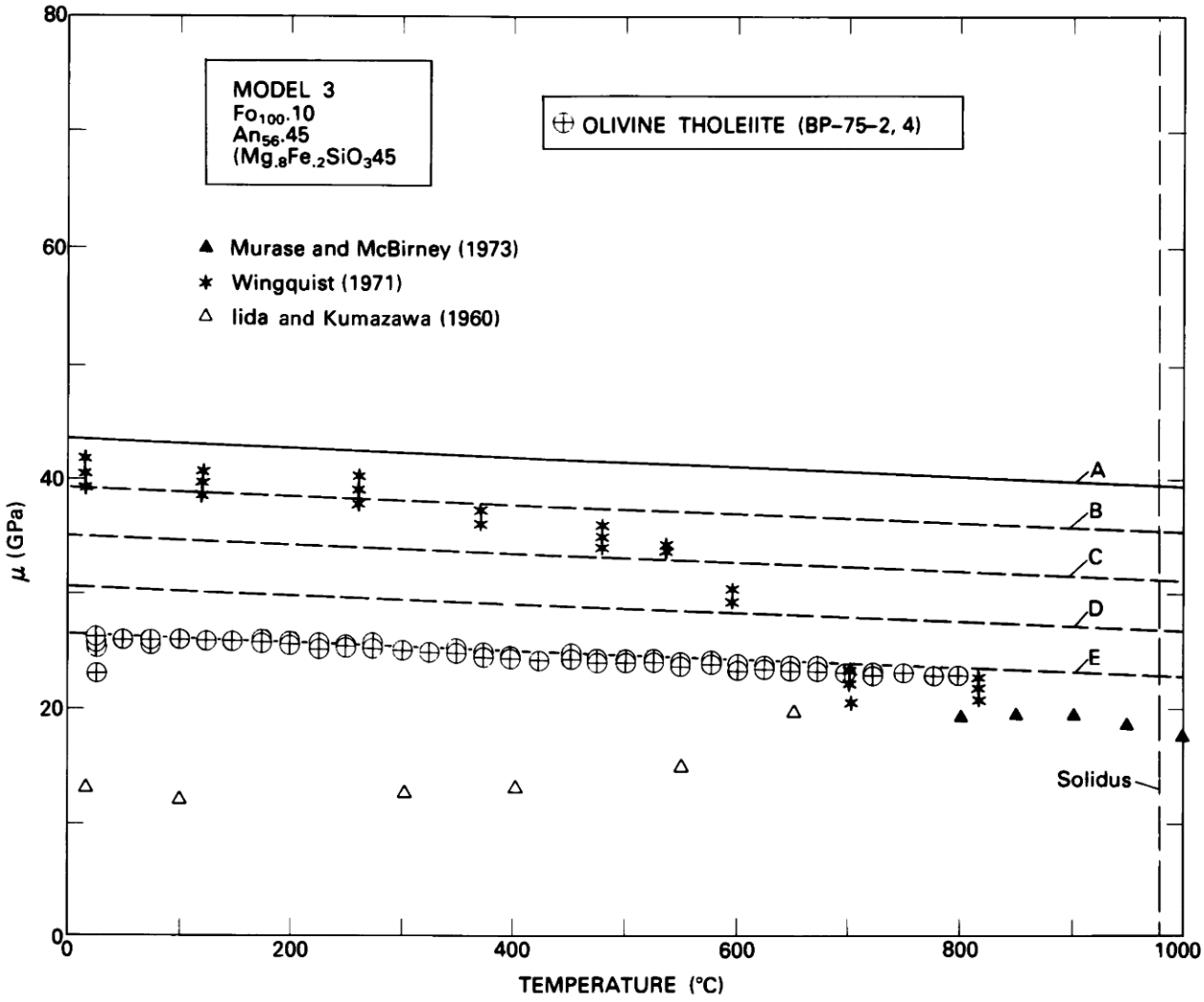

FIGURE 52.15.—Predicted high-temperature, ambient-pressure V-R-H rigidities and matrix Voigt and Reuss bounds on rigidity for compositional submodel 3. Measured rigidity of Boiling Pots olivine tholeiite, crossed circles. Differences between measured and predicted rigidities probably result from iron oxide minerals and intercrystalline glass that have not been incorporated in submodel.

TABLE 52.8.—*Comparison of the temperature dependence of the elastic moduli from the compositional model (I) at Φ = 0 and the measured dynamic rigidity and Young's modulus for olivine tholeiite of Boiling Pots*

	$(\partial K/\partial T)_{VRH}$ (MPa/°C)	$(\partial \mu/\partial T)_{VRH}$ (MPa/°C)	$(\partial E/\partial T)_{VRH}$ (MPa/°C)
Compositional submodel:			
1	−15.31	−4.47	−13.13
2	−11.28	−2.34	−7.32
3	−13.30	−3.39	−10.23
Boiling Pots olivine tholeiite measurements		−3.5[1] −4.2[2] −3.8[3]	−8.5[4] −8.1[5] −8.3[6]

Sample designation:
(1) BP-75-R2(G)
(2) BP-75-R4(G)
(3) BP-75-R2(G) + R4(G)
(4) BP-75-R6 ..... Φ = 0.15
(5) BP-75-R1 ..... Φ = 0.15
(6) BP-75-R6 + R1 ..... Φ = 0.15

temperature dependence of K, μ, and E, and the average basalt (submodel 3) lies between 1 and 2 in temperature dependence.

The temperature derivatives for the rigidity and Young's modulus of Hawaiian olivine tholeiite have been generated by the least-squares regression procedure. These derivatives are presented in the lower portion of table 52.8 and may be compared with the model derivatives. In the table, the entries for both $\partial\mu/\partial T$ and $\partial E/\partial T$ of samples BP-75-R2(G), -R4(G), -R6, and -R1 are replicates, whereas the other sample entries are derivatives that were formed via least-squares regression on the averaged-value data set.

Comparison of the model and measured rigidity values in table 52.8 shows that submodel 3 with plagioclase contents of 45–50 percent provides a close approximation to the modulus reduction with temperature of the Boiling Pots olivine tholeiite.

Differences between moduli magnitudes predicted using compositional submodels plus microstructural modeling and those magnitudes evaluated by resonant-frequency measurements are believed to arise from the following sources:

(1) Opaque and glass-filled minor inclusions in olivine, hypersthene, augite, and plagioclase phenocrysts and microphenocrysts;

(2) Groundmass magnetite and opaque-rich groundmass glass pockets that have not been incorporated in the model; and

(3) Subtle differences in the elastic properties of matrix crystals versus model crystals that may arise from (a) compositional zoning and defects in olivine and (or) defects in pyroxene and in labradorite, or (b) unrelieved thermal strains in crystal lattices, induced by posteruption chilling.

For all moduli, the measured values lie between the pyroxene-rich and plagioclase-rich upper and lower values. That is,

$$(\partial\mu/\partial T)_{VRH}^{\text{model 1}} > (\partial\mu/\partial T)_{\text{measured}} > (\partial\mu/\partial T)_{VRH}^{\text{model 2}}$$

and

$$(\partial E/\partial T)_{VRH}^{\text{model 1}} > (\partial E/\partial T)_{\text{measured}} > (\partial E/\partial T)_{VRH}^{\text{model 2}}.$$

These relations hold for both the average of the measured values and for each of the replicates. This bounding behavior of the Hill-averaged models accords with the expected behavior, recalling that the modal abundance of all pyroxene species in the Boiling Pots basalt was 32.9 percent, whereas the total of groundmass and microphenocryst plagioclase content is 37.3 percent and olivine totals 12.4 percent.

THE PRESSURE DEPENDENCE OF ELASTICITY IN HAWAIIAN BASALT: CONTRACTANCY AND MAGMATISM

This section, which discusses the pressure dependence of elasticity in Hawaiian rocks, complements the discussion of the major sections of this paper on variations in elasticity and expansivity, which are temperature dependent. Focus is placed on the implications these rock properties have for the mechanical controls on magmatic storage regions within active shield volcanoes; both subcaldera reservoirs and their rift systems are considered. Underlying the discussion are the influences of microstructure, microcracks, and composition as previously developed. A major conclusion of this section is that the pressure dependence of elasticity in the rocks of shield volcanoes affects their in-situ behavior in ways that lead naturally to spatial domains of magmatic stability. Ramifications include (1) density crossovers in the in-situ country rock and magma; (2) a rationale that unifies the observed seismic-velocity variations within and beneath Hawaiian shields, experimentally determined rock properties, and the massive dilatancy associated with the free surface of the Earth in regions of active volcanism; and (3) the mechanical rationale for the long-held inference that Hawaiian magma reservoirs move progressively upward during their life cycle.

Studies of the mechanics of magmatic fluids, rock-fluid mixtures, and the deformation accompanying injection and withdrawal with relevance to regions of active volcanism have been approached from six viewpoints: (1) in-situ density contrasts between melt and country rock within mantle and crustal sections (Waff, 1980; Stolper and others, 1981; Grove and Baker, 1983; Herzberg and others, 1983; Sparks and Huppert, 1984), with emphasis on the distribution in and separation from the mantle source region, and the role of fractional crystallization on melt density; (2) wholesale diapiric rise with concurrent decompression melting (Ramberg, 1981); (3) continuum solutions of hydraulic fracture stability and fluid-induced deformation (Weertman, 1971a, b; Johnson and Pollard, 1973; Pollard, 1976; Pollard and Muller, 1976; Weertman and Chang, 1977; Pollard and Holzhausen, 1979; Weertman, 1980; Ryan and others, 1983; Spence and Turcotte, 1985); (4) reviews and syntheses of the effective-stress principle (Shaw, 1980; Gold and Soter, 1985); (5) thermodynamic analyses in combination with the wetting mechanics of basaltic melts (Waff and Bulau, 1979; Bulau and others, 1979; Waff, 1979, 1980); and (6) fluid-dynamic and fluid-static analyses of incompressible single-phase (Shaw and Swanson, 1970; Vogt, 1974; Solomon, 1975; Fedotov, 1977a, b, c), incompressible multiphase (Sleep, 1974; McKenzie, 1984), and compressible multiphase fluids (Wilson and Head, 1981). In a different vein, but of relevance to the following discussion, is the work of Eaton and Murata (1960) and Fiske and Jackson (1972), who respectively computed equilibrium heights expected for

Hawaiian volcanoes and emphasized the importance of gravitational stresses in the development of Hawaiian rift zones.

In its conceptual development, the discussion that follows differs from these studies in the following ways:

(1) The focus of attention on the free surface of the Earth, with particular emphasis on the heterogeneous distribution of material properties, and the nonlinear mechanical behavior exhibited by rocks as the surface is approached;

(2) The evolutionary consequences that derive for magmatic bodies as the Earth's free surface is progressively translated upward—an explicit consideration of the evolutionary track followed by shield volcanoes within a magmatic province, as they mature and age;

(3) An integration of the confining pressure behavior of shield volcanoes, with their geodetic, seismic, density (gravitational), lithologic and structural characteristics, providing guidelines, constraints and tests for internal consistency; and

(4) An exploration of the three-dimensional structure of the resulting contractancy concept, and its implications.

The discussion can be started by posing a series of related questions. What are the controls on the stability of magmatic bodies at depth? What are the roles of open, partially contracted, and fully contracted fractures in these environments? Can the recurring themes of intrusion-eruption and the drainback of lava within rift systems be understood within a context of vertical changes in macroscopic and microscopic fracture closure, as these affect the bulk density of a volcanic shield and interact with the density of magma at depth? The thrust of the discussion then lies in the confining-pressure dependence of the mechanical properties of shield volcanoes. A set of general relations can be developed by the study of well-characterized volcanoes in Hawaii, especially Kilauea and Mauna Loa.

PHENOMENOLOGY OF CONTRACTANCY

The bulk compressibility of the subsolidus volcanic shield may be expressed as follows:

$$\beta_{VS} = \beta_M + \beta_{MS} + \beta_{PF} + \beta_F, \tag{41}$$

where β_{VS} is the volanic-shield compressibility, β_M is the mineral phase compressibility, β_{MS} is the microstructure compressibility that combines contributions from vesicles and microcracks, β_{PF} is the pore-fluid compressibility, and β_F is the macroscopic fracture compressibility.

For tholeiitic shield volcanoes, the mineral-phase compressibility is built up from the individual compressibilities of olivine, clinopyroxene, orthopyroxene, and plagioclase, with subordinate contributions from magnetite, ilmenite, and apatite. In general terms, the largely tholeiitic shield will have compressibilities dominated by the volumetrically important mineral species: olivine, clinopyroxene, and plagioclase. The magnitude of this contribution will then scale with the weighted volume fraction of each component.

The total compressibility of large volumes of the shield may now be divided into two contributors: intrinsic and extrinsic. Laboratory studies evaluate the intrinsic contributors, and the separation of single-crystal acoustic-velocity studies and whole-rock studies provides a means of sorting out the crystalline and microstructural contributions. The extrinsic contribution is provided by the large fractures within the shield. These fractures are the dilatant cracks and fissure networks that intersect the free surface of the volcano. They define the bounding planes of rift-zone graben and may be exploited by rising magma during intrusion and eruption sequences. Seismic velocity studies carried out over major segments of a shield then sample the total compressibility. The evaluation of the bulk modulus of portions of the shield then yields a means of recovering the relevant in-situ compressibility—summed for each major contributor above.

Contractancy, in the sense used here, can be viewed as a mechanically opposite effect of dilatancy. It is reflected in the progressive reduction in volume of an element of rock that contains minerals, microcracks, macroscopic joints and fractures, equant pores, and saturating pore fluids, as this conceptual element is subjected to continuously increasing confining pressures. The phenomenon, within the context of magmatic systems, is dominated by the progressive closure of macroscopic fractures and joints, and microscopic fractures with depth. This closure is viewed as a progressive elimination of the extrinsic contributors to bulk compressibility. It is a realization that very nonlinear effects dominate the mechanical behavior of rocks as the surface of the Earth is approached. These effects are well exemplified by the pressure dependence of V_p and V_s in both the laboratory studies and field-derived seismic-velocity profiles. Contractancy may be contrasted with dilatancy, which is an inelastic volume increase under applied loading (Brace and others, 1966; Schock and others, 1973). Such volume increases lead to decreases in the ratio V_p/V_s (Whitcomb and others, 1973; Wyss and Holcomb, 1973) and begin at approximately one-half to two-thirds the fracture strength of the rock.

Evaluations of the compressional and shear wave velocities of rocks, from the transit times of acoustic waves in laboratory samples, provide the means of assessing the microstructural and mineralogical contributions to contractancy. The pressure dependence of V_p for the dominant lithologies of Hawaiian volcanoes is summarized in figures 52.16, 52.17, and 52.18. These lithologic types represent their tholeiitic shields, alkalic and nephelinitic interlayers and caps, intrusive complexes, olivine-rich cumulates, and the mafic and ultramafic rocks of their oceanic crustal and upper-mantle foundations. In each of the figures, the pressure dependence of V_p, $\partial V_p/\partial P$, shows the two types of behavior: an early, highly nonlinear dependence extending from 0 to 200 MPa (2 kbar), and a generally linear regime starting at about 200 MPa and extending to higher pressures. Studies of holocrystalline rocks (Todd and Simmons, 1972), as well as of porous lithologies (King, 1966), have attributed this change in wave velocity to the progressive closure of microcracks within the rock matrix. This microfracture closure—or contractancy—produces the early rapid rise in V_p and V_s characteristic of the low-pressure shallow environment. The generally linear change in wave velocity above 200 MPa is produced by the compressibility of the minerals within the matrix.

CONTRACTANCY WITHIN SHIELD VOLCANOES

Several lines of evidence suggest that the superstructure of Hawaiian shield volcanoes contain dilatant fractures and that these open fractures extend to considerable depths. The evidence includes:

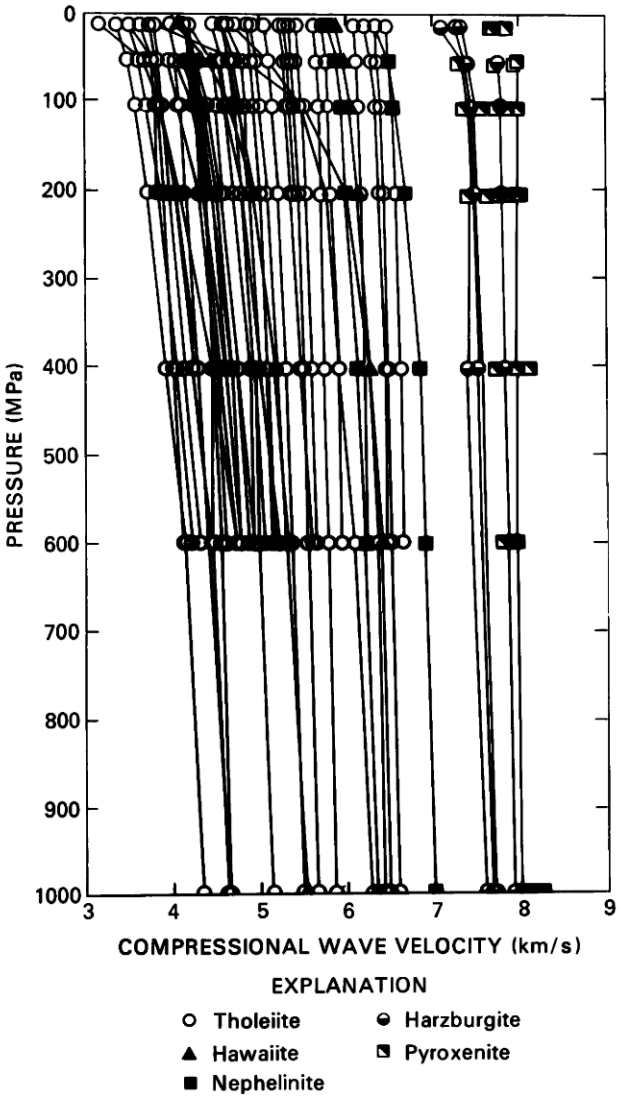

FIGURE 52.16.—Pressure dependence of compressional-wave velocities (V_p) in tholeiitic, alkalic, and nephelinitic basalt and in ultramafic lithologies composing upper-mantle underpinnings of Hawaiian volcanoes. Of particular interest is nonlinear behavior of V_p at confining pressures below 200 MPa, which is produced by progressive elimination of microfractures with continued pressure increases. Data compiled from Bajuk and others (1957), Manghnani and Woollard (1968), Christensen and Salisbury (1972, 1973), Christensen (1973, 1976, 1978), Fox and others (1973), Fox and Schreiber (1973), Christensen and others (1974a, b), Schreiber and others (1974), Hyndman (1976), Kroenke and others (1976), and Salisbury and Christensen (1976).

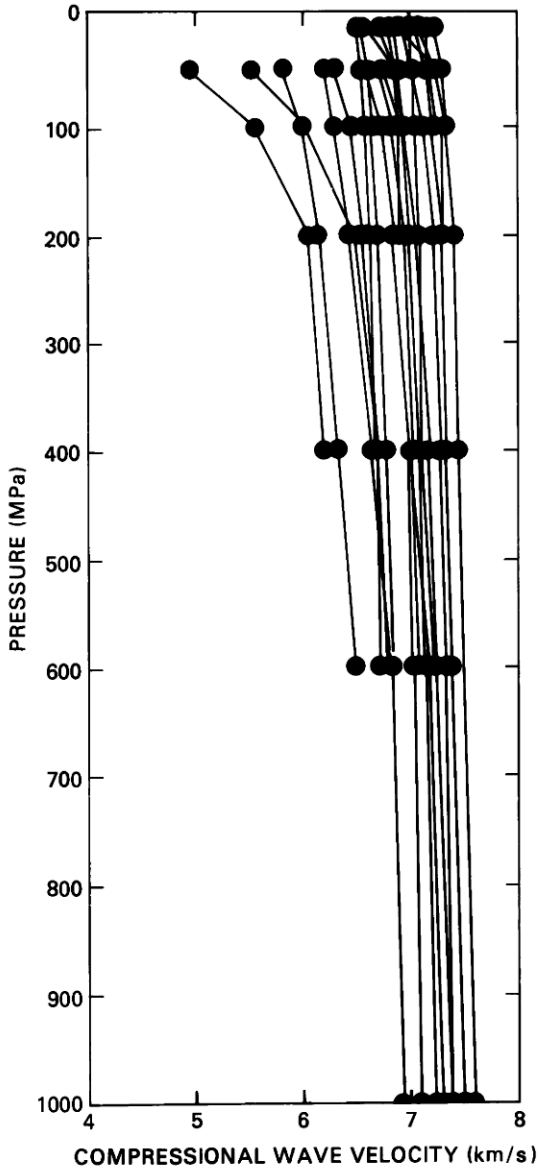

FIGURE 52.17.—Pressure dependence of compressional-wave velocity in gabbro. Distribution of gabbroic xenoliths in vent areas of Hawaiian volcanoes and their resemblance to intrusives exposed in cores and rift zones of dissected volcanoes suggest that gabbros form in a major fraction of magmatic storage region in active portions of system. Marked changes in $\partial V_p/\partial P$ above and below 200 MPa suggest a progressive closure of microfractures in upper regions of volcanic shield, with a transition to mineral compression at $p > 200$ MPa (2 kbar). Data compiled from Schreiber and others (1972), Fox and others (1973), Mizutani and Newbigging (1973), Wang and others (1973), Christensen and others (1975), Hyndman (1976), Kroenke and others (1976), and Christensen (1978).

(1) Gaping cracks in rift systems and summit calderas that have crack opening displacements ranging from tens of centimeters to meters (for example, the Great Crack of Kilauea's southwest rift zone);

(2) Exceptionally low compressional-wave velocities in the upper 2 km of the volcanic pile;

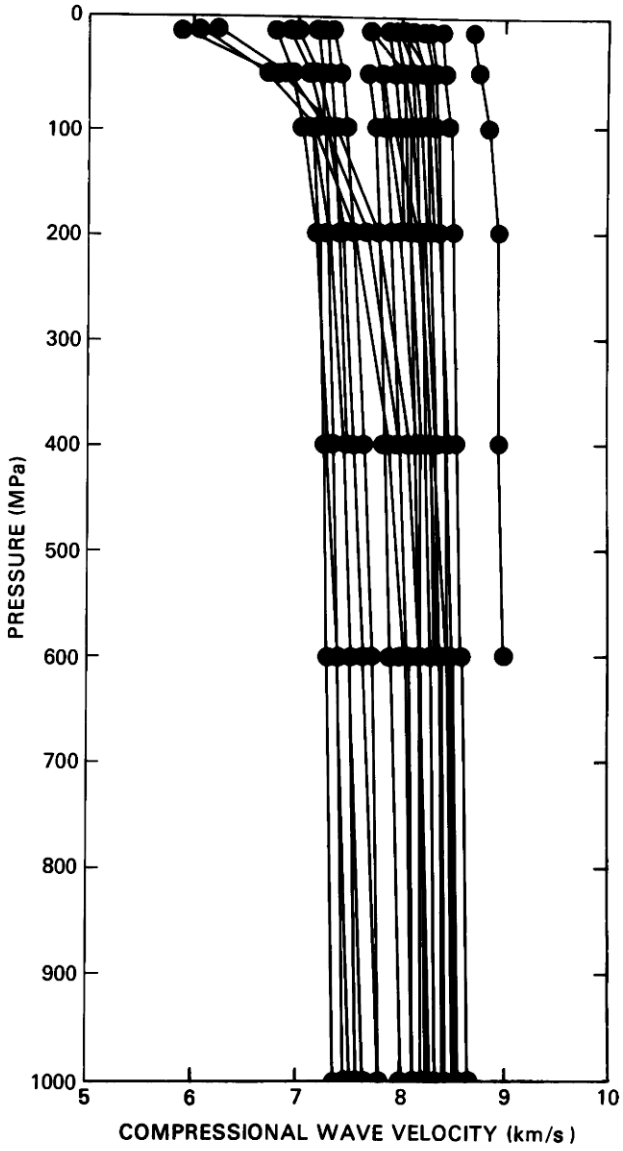

FIGURE 52.18.—Pressure dependence of compressional-wave velocity in dunite. Dunitic xenoliths in alkalic and nephelinitic vent areas suggest relatively widespread occurrence of dunite in upper mantle beneath Hawaii. Additional association is made with refractory mantle-root areas of tholeiitic suite of lavas, as well as a role as cumulates in crustal storage reservoirs during tholeiitic magmatism. In most of these roles, aggregate elastic behavior will lie well within region dominated by mineral compression and structural properties of olivine. For olivine-rich early cumulates that form in storage compartments within a volcanic shield or rift-zone base, nonlinear sections of compressional-wave curves are expected to apply. Data compiled from Hughes and Cross (1951), Bajuk and others (1957), Kanamori and Mizutani (1965), Christensen (1966, 1971), Manghnani and Wollard (1968), Mao and others (1970), Christensen and Ramananantoandro (1971), Babuska (1972), Christensen and Salisbury (1972), and Rao and others (1974).

(3) Exceptionally low in-situ densities in the upper 2 km;

(4) The common observation of massive drainback at the conclusion of an eruptive phase. An archetypical example is the drainback volume of 6×10^6 m^3 for phases of the 1959 Kilauea Iki eruption (Richter and Moore, 1966), and drainback rates as high as 1.5×10^6 m^3 per hour.

(5) Simultaneous eruption and drainback, as exemplified by the 1983 activity at Puu Oo, in Kilauea's east rift zone; and

(6) The long-observed discrepancy between the vertical and horizontal displacement fits to geodetic model predictions. As discussed by Ryan and others (1983), the vertical displacements at Kilauea, for example, are largely reversible, whereas the horizontal components are very weakly reversible. For the upper regions of the shield, rock behavior is elastic in the vertical plane, whereas the horizontal plane contains substantial inelasticity.

The fracture systems within Kilauea caldera, the summit region, and the upper southwest rift zone are shown in figures 52.19 and 52.20.

ENVIRONMENT AT DEPTH: EFFECTS OF PRESSURE AND TEMPERATURE

Rocks forming the central and basal sections of oceanic shield volcanoes are expected to contain pore fluids. Traveling downward within the subaerial portion of an oceanic volcanic system, we would therefore expect to approach a horizon above which the pore space contains air, volcanic gases, and water vapor and below which the accessible pore space is saturated with H_2O. The water would be either fresh or saline, depending on the local configuration of the Ghyben-Herzburg lens. It is relevant then to consider the contractancy of basalt with both dry and H_2O-saturated pore space, and its pressure dependence. These curves are presented in figure 52.21*B* for basalt (Christensen and Salisbury, 1975). The characteristically nonlinear $\partial V_p/\partial P$ at pressures less than 200 MPa is well developed—particularly for the dry curve where the accessible porosity is occupied by air. Both sets of curves show an additional effect: there is a pressure window above which (that is, toward higher P) the pore space accessible to any second phase—air or H_2O—has been squeezed out. For basalt and gabbro, this pressure window corresponds to a transition zone centered at about 200–300 MPa. The figure also contains a series of inset diagrams that depict the progressive elimination of macroscopic and microscopic fracture permeability with progressive increases in confining pressure. The transition zone that coincides with the convergence of the dry and fluid-saturated compression branches is herein referred

to as the compression transition zone. This zone separates the figure into two subregions: a shallow region where the dominant mechanism is the compression of fractures and pore fluids, and a deeper region where further volume reductions are dominated by mineral compression. In constructing the figure, the confining pressures of Christensen and Salisbury (1975) have been converted to depth equivalents, taking into account the density-depth relations for Kilauea presented by Zucca and others (1982).

A summary diagram of data (fig. 52.21*A*) represents the geodetic and seismic constraints on the depth intervals inferred for the position of the summit magma reservoir. These constraints are derived from (1) three-dimensional deformation modeling employing collateral geologic and mechanical property contraints (Ryan and others, 1983); (2) two- and three-dimensional studies of the distribution of magma-reservoir seismicity (Koyanagi and others, 1976; Ryan and others, 1981); (3) geometrically idealized modeling of simply connected sources of pressure or displacement (Mogi, 1958; Deiterich and Decker, 1975); and (4) inversions of summit-tilt, trilateration, and vertical-displacement data, via least-squares regression (Dvorak and others, 1983). The depth interval 2 to 4 km is common to all the inferred ranges and appears to comprise a consensus for the uppermost reaches of the storage region proper. This depth region for magma storage extends to at least 6 km, based on geodetic and seismic evidence.

A comparison of figures 52.21*A* and 52.21*B* suggests that there is a strong correlation between the depths of subcaldera magma storage and the depth intervals that permit the continued dilation of fluid-accessible fractures in basalt. Increases in compression to confining pressure levels in excess of that required to eliminate fracture porosity passes the reference-volume element in figure 52.21*B* below the compression transition zone and into a depth level below the summit storage complex. Note that the curves in figure 52.21*B* describe the microcrack closure behavior for basalt. The addition of macroscopic joint closure has a pressure dependence that is qualitatively similar. Detailed differences between the two arise from the contribution of crack surface topography to joint stiffness

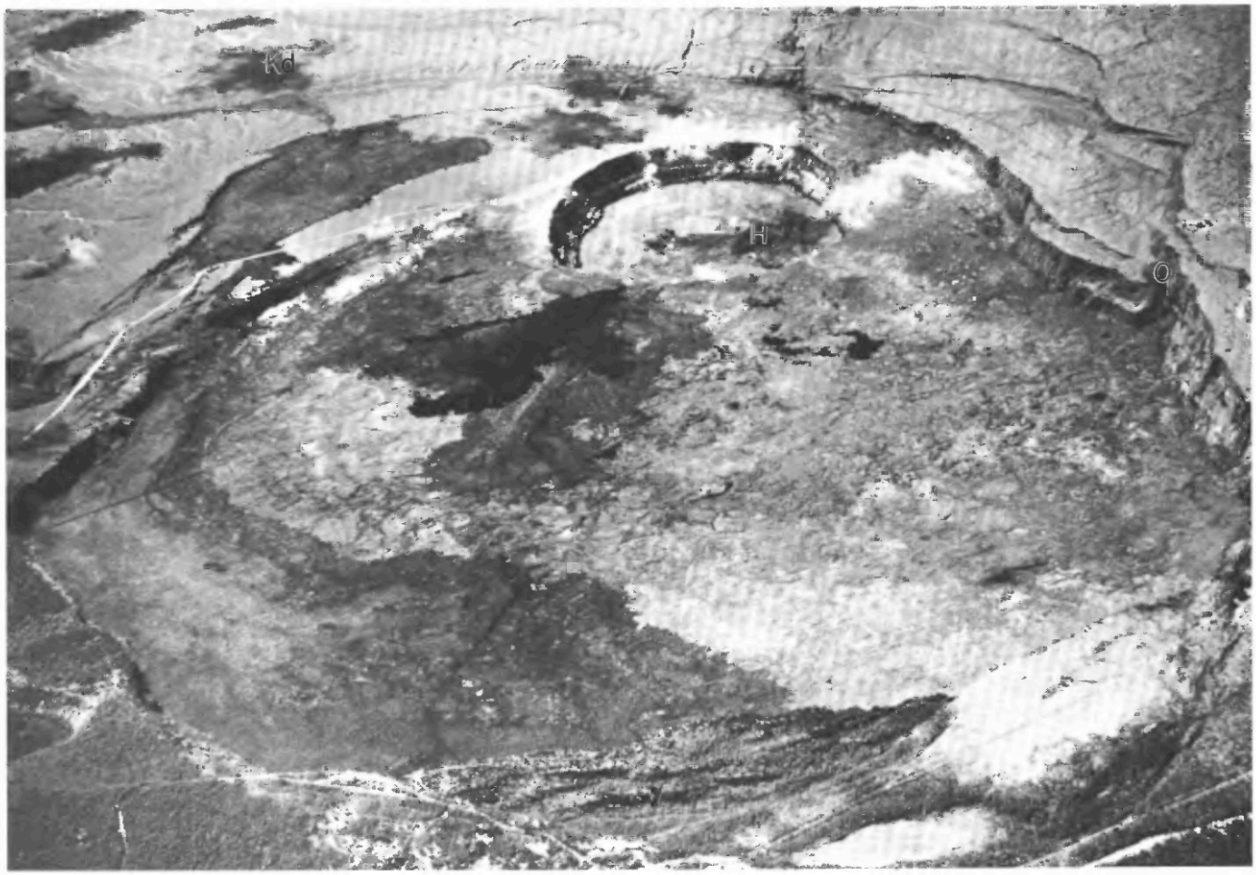

FIGURE 52.19.—Kilauea caldera in west-directed view. Magmatic inflation and deflation centers migrate laterally beneath much of western caldera floor and to south, beyond upper Kau Desert (Kd). Such temporal migration patterns are surface expressions of multiply connected complex of dikes and sills that form summit magma-storage reservoir. They are spatially associated with region of neutral buoyancy. Multiple collapse regions within caldera lie at foot of Volcano House (V). Hawaiian Volcano Observatory (O), and within Halemaumau (H). Photograph by James Griggs.

(Brown and Scholz, 1985). To be noted also is that these curves describe the crack-closure behavior for basalt in the absence of an applied pore pressure—that is, they reflect the inherent crack and rock stiffness itself in maintaining open permeable pathways above the compression transition zone. Applied pore pressures enhance the stability of an open fracture network at depth, as discussed in the next section.

Open fractures provide an environment for laterally extensive magmatic movements in three ways: (1) the obvious intrusion sites provided by dilatant macroscopic fractures; (2) the contributions to neutral buoyancy and magmatic stability produced when the open fracture network is so pervasive that the in-situ rock density is reduced to values equal to (and less than) the in-situ density of melt near its liquidus: and (3) the dilation of microfractures that provide penetration pathways for melt adjacent to advancing crack tips at depth. The wetting properties of basalt near its liquidus (Waff and Bulau, 1979; M. Ryan, unpublished data, 1980) confirm this capability.

The fracture-closure/depth behavior for basalt and gabbro also correlates with the depth extent of Kilauea's rift systems. These depths have been inferred by the position of the bottom of the zone of south-flank seismicity—produced by the inflation of dikes within the southwest and east rift zones. This depth is locally 9–12 km beneath the surface of the volcano. Beneath the east rift zone, this depth is 9–10 km, which is coincident with the 8- to 9-km depth (beneath sea level) inferred from south-flank block kinematics in the study of Crosson and Endo (1982). This region coincides with the transition zone that lies at the base of the field of fracture and pore-fluid compression in figure 52.21*A*. These relations are in harmony with the porposal of Nakamura (1980), who suggested that the mechanically soft sediments of the old ocean floor provided lateral accommodation for the development of long rift zones in Hawaiian shield volcanoes. Indeed, both shield contractancy and lateral slip surfaces in low-modulus sediments may locally work together in regulating the depth extent of rift zones. During continued shield building, however, the keel of the active rift system is expected to rise

FIGURE 52.20.—Junction of southwest rift zone (SWRZ) and Kilauea caldera near Halemaumau (H). Fractures produced on surface record stretch at depth due to increments of dike injection. These fractures produce low in-situ densities and compressional-wave velocities that characterize upper 2 km of shield. In turn, low in-situ densities interact with density of tholeiitic melt near its liquidus to produce region of neutral buoyancy that stabilizes magmatic storage at depth as well as dike emplacement within rift systems. An automobile on caldera rim road (right center) provides scale. Photograph by James Griggs.

above the old oceanic floor and have a depth extent exclusively regulated by the mechanics of volcanic-shield contractancy. A summary of the mechanical relations that have been detailed in figure 52.21*A* and 52.21*B* is provided in figure 52.22.

In addition to the pressure dependence of rock behavior in the vicinity of the magma-storage reservoir, it is of interest to comment on the temperature dependence of basalt elastic moduli near the shallow, low-pressure portions of the reservoir, which can be done by evaluating $E(T)$ and $\mu(T)$ at temperatures approaching the solidus. Applications include estimating the relative contribution(s) of thermal-stress-induced fracture and evaluations of the bending stresses associated with magma-reservoir-roof flexure during inflation-deflation cycling. In evaluating these moduli, three auxilary constraints have been applied: (1) direct temperature-depth measurements beneath the summit of Kilauea; (2) the location of the summit reservoir based on geodetic and seismic studies (discussed above); and (3) eruption and liquidus temperatures determined in summit and near-summit eruptions, and reconstructed in melting experiments on summit compositions. The region of evaluation lies below the upper several hundred meters that characteristically has heavy contributions of macroscopic fractures, leading to the expected low in-situ moduli.

Rotary drilling to 1,262-m depth beneath Kilauea's summit (Zablocki and others, 1974) has provided a temperature-depth profile through the shallow water table to a position below sea level. The stabilized profile shown in figure 52.21*A* has a bottom-hole temperature of 137 °C and suggests an initial thermal gradient of about 370 °C/km. This profile bottom provides a pinning point that is used to hinge a family of thermal gradients, as discussed below.

Temperatures have been measured by optical pyrometry in summit and near-summit lava fountains (for example, Richter and Murata, 1966; Peck and Kinoshita, 1976), and directly in advancing flows and in lava lakes (for example, Wright and Weiblen, 1968; Jackson and others, 1975; Swanson and others, 1976). For many of these measurements, the shrouding effects associated with eruption plumes and the thermal gradients associated with the free surface of active flows suggest that they are generally below true magmatic temperatures. Relations between liquidus temperatures and iron enrichment determined experimentally for samples of Kilauea Iki eruption pumice (Thompson and Tilley, 1969) suggest temperatures in the range 1,225 to 1,188 °C. In addition, Helz and Thornber (1985) present an approach for restoring temperatures measured in lava-lake drill holes to the predrilling in-situ values, based on a glass-based calcium geothermometer. Olivine crystallization in Makaopuhi lava lake (Wright and Weiblen, 1968) has identified a temperature of 1,200 ± 10 °C. Collectively, these studies suggest that the liquidus temperature for Kilauean olivine tholeiite at atmospheric and near-surface pressures lies close to 1,200 °C, and this value has been associated with the subcaldera storage environment in figure 52.21*A*. It is enclosed by a shaded band that encompasses the high temperature end of the illustrated measurement ranges, and extends to 1,210 °C.

From the high-temperature limit of the drill-hole bottom (137 °C) at 1,262 m, four thermal gradients have been constructed to the 2.0-, 2.5-, 3.0- and 3.5-km-depth levels. These gradients are labeled A through D, and they span the range 1,440 to 476 °C/km (fig. 52.21A). They are tied to the 1,200 ± 10-°C low-pressure liquidus for the range of depths appropriate for the "attic" of Kilauea's subcaldera magma reservoir. The span in gradients explicitly recognizes the aggregate uncertainty in both the detailed positioning of the storage region and its temperatures. In this respect, it is prudent to consider a probable range of values. Grouped together, the drill-hole measurements, the liquidus temperature assignments, and the resulting interpolation gradients form a one-dimensional thermal model for the summit section of Kilauea.

From the relations for the temperature dependence of the Young's modulus and the rigidity previously presented and evaluated, working estimates can be made for conditions of low pressure. For the Young's modulus, the relation $E(T)=(6.054-0.00083T)\times 10$ GPa, evaluated along gradient A in figure 52.21*A*, leads to the relation $E(z)_A \approx (6.054-1.195z)\times 10$ GPa, where z is the depth in kilometers. Evaluated along gradient D, the corresponding relation is $E(z)_D \approx (6.054-0.395z)\times 10$ GPa. For the shear modulus, the relation $\mu(T)=(2.615-0.00038T)\times 10$ GPa, leads to $\mu(z)_A \approx (2.615-0.547z)\times 10$ GPa and $\mu(z)_D \approx (2.615-0.181z)\times 10$ GPa. Evaluations made to temperatures approaching the low-pressure solidus suggest that about a 15-percent reduction occurs in both E and μ. Considerations of the high-temperature tensile strengths of basalt (M. Ryan, unpublished data; Ryan and Sammis, 1981), combined with the linear thermal-expansion coefficients described in the section "High-Temperature Elasticity of Hawaiian Basalt" and the relation of thermal stress under plane-strain conditions,

$$\sigma_T = \frac{E\alpha_l(\Delta T)}{1-\nu},$$

suggest that local temperature drops of 50 to 100 °C are sufficient to cause thermal-stress-induced fracture. Hence, moderate falls in temperature that may, for example, be associated with influxes of relatively cool water—produced by tectonic adjustments within the mantling aquifer—may thermally load the rocks above active magma reservoirs to points near failure. This thermal component would then be coupled with the bending stresses that are associated with the flexure of the reservoir roof during inflation-deflation cycling. Together, they produce the seismically active lid on the storage region below. Associated with this recurrent rock fracture would be inferred changes in the fracture network, the mechanics of which are discussed below.

EFFECTS OF PORE FLUIDS AND JOINT CLOSURE

The curves in figures 52.21*B* and 52.22 illustrate the confining pressure (P_c) dependence of compressional-wave velocity for basalt and emphasize the depth dependence of permeable pore-space elimination. The progressive nature of microcrack closure with increasing P_c is also emphasized. It is of interest now to outline the effects expected for macroscopic joint closure and the effect of pore fluids under pressure.

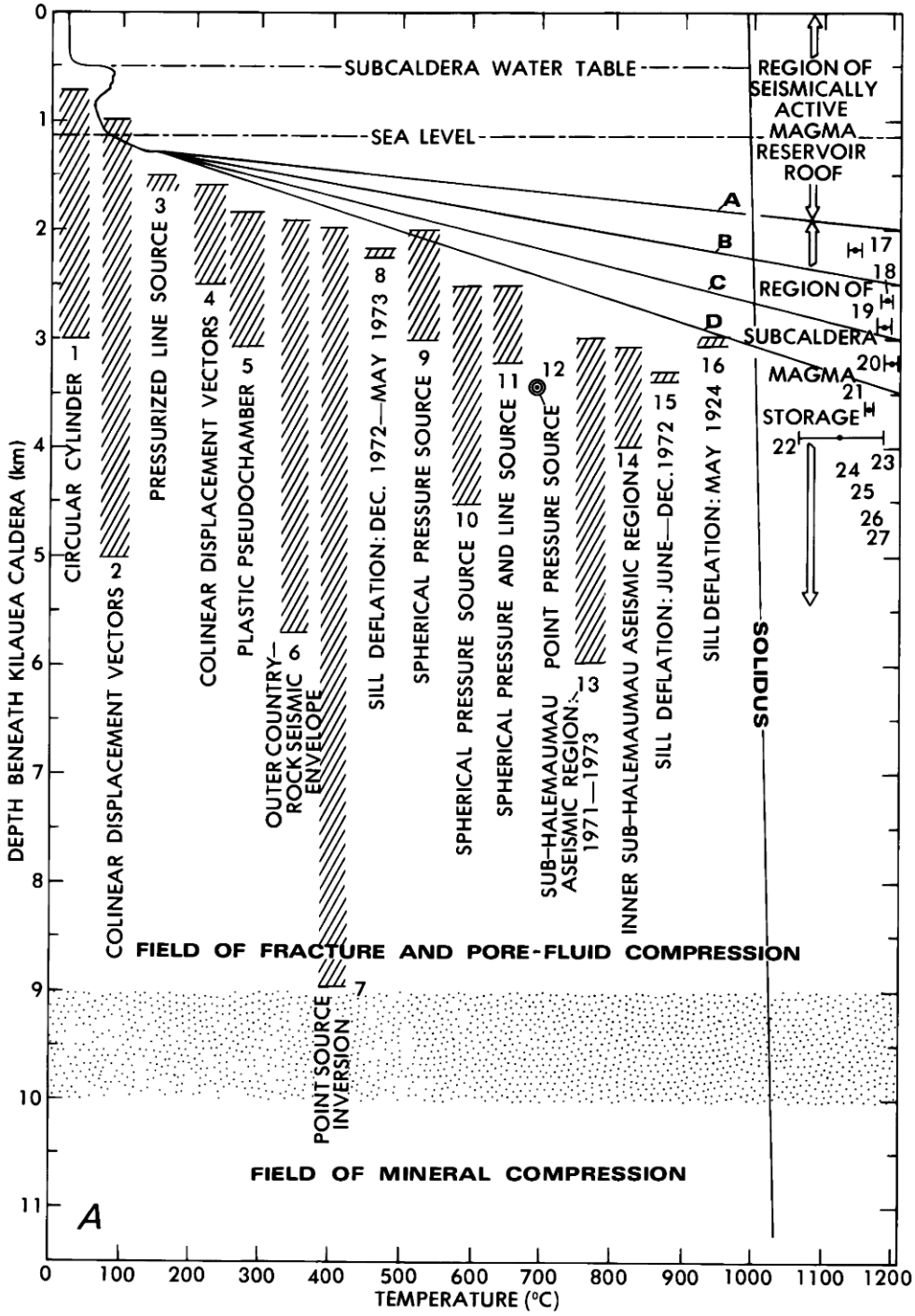

FIGURE 52.21.—Depth relations beneath Kilauea caldera. *A*, Summary depth distributions of Kilauea's subcaldera magma-storage reservoir and its intrusive components. Depth interval 2–4 km is common to all 16 models and submodels. Added to field is temperature profile beneath summit as measured directly to 1,262 m. Direct temperature measurements in erupted lava, laboratory determinations, and optical pyrometer measurements are given by horizontal bars that cluster near 1,200 °C. They have been assigned to the 2- to 4-km-depth interval, reflecting consensus of geodetic and seismic reservoir models (numbers 1–16). Hachured region that encloses them is intended to suggest a broad-working estimate of a range of in-situ temperatures within this depth interval. Radiating from maximum temperature point at 1,262 m to depth regions along the 1,200-°C margin that

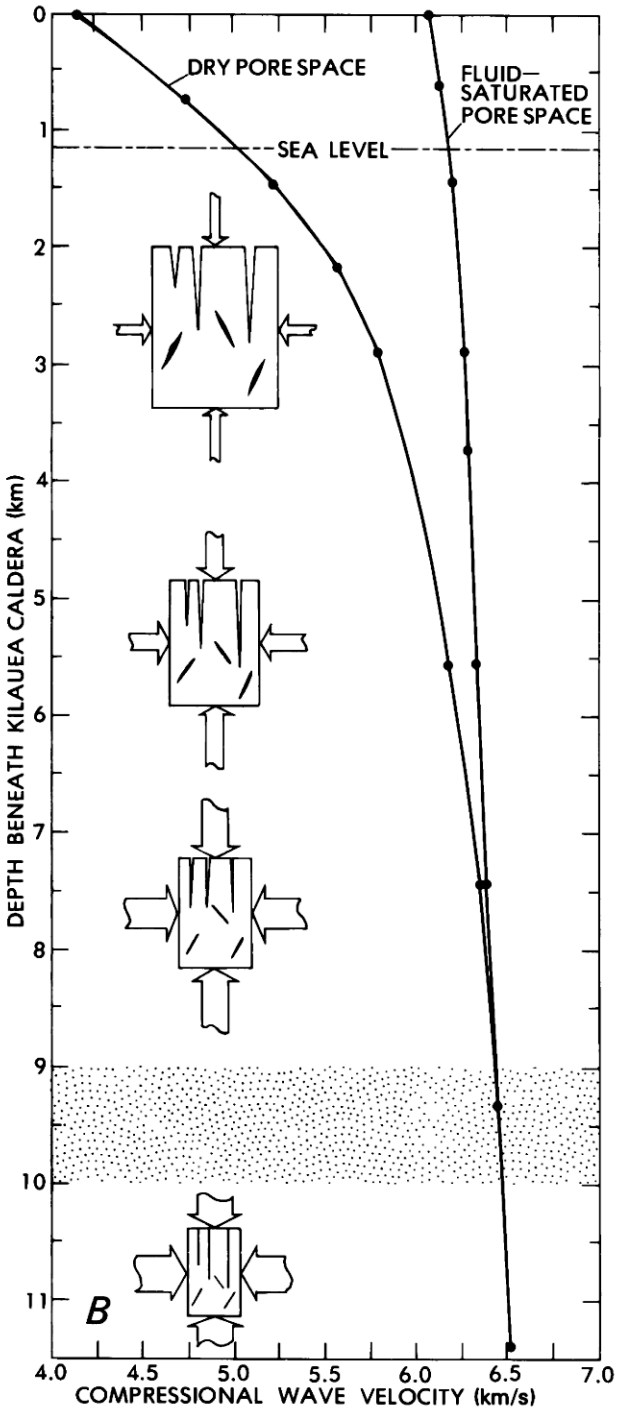

corresponds to upper levels of summit magma storage is a family of four thermal gradients (A–D). They explicitly recognize uncertainty implied by both depth distributions and temperature ranges. Data sources for compilation include (a) Summit temperature-depth profile: Zablocki and others (1974). (b) Solidus: Wright and Okamura (1977); pressure dependence of solidus, dT_m/dP: Yoder and Tilley (1962); Hill and Boettcher (1970). (c) Depth of summit magma storage (numbers identify plotted values and ranges): (1) Dieterich and Decker (1975); (2) Duffield and others (1982); (3) Walsh and Decker (1971); (4) Mogi (1958); (5, 7) Jackson and others (1975); (6) Fiske and Kinoshita (1969); (8) Davis and others (1974); (9) Ryan and others (1981); (10) Dvorak and others (1983); (11, 14, 15, 16) Ryan and others (1983); (12) Eaton (1962); (13) Koyanagi and others (1976). (d) Magmatic temperatures (numbers identify plotted measurements): (17) Moore and others (1980); (18, 21) Swanson, Duffield, and Fiske (1976); (19) Jackson and others (1975); (20, 26) Wright and Weiblen (1968); (22) Richter and Murata (1966); (23, 24) Thompson and Tilley (1969); (25) Yoder and Tilley (1962); (27) Wright and Fiske (1971). ***B***, Compressional-wave velocities in dry and H_2O-saturated basalt as a function of increasing depth (confining pressures). Congruence of branches at 9-km depth suggests that all H_2O-accessible porosity has been squeezed out. Further increases in confining pressure (arrowed pathways) cross through transition region (dot pattern) into field of mineral-compression-dominated volume changes. Inset diagrams depict progressive elimination of microscopic and macroscopic permeability with increasing confining pressure. Data sources for compilation include pressure dependence of compressional-wave velocity from Christensen and Salisbury (1975).

For an orthotropic medium containing three sets of mutually orthogonal joints, the effective compressibility may be expressed as (Amadei and Goodman, 1981):

$$\beta^* = \frac{1}{K^*} = 3\left(\frac{1-2\nu}{E}\right) + \sum_{i=1}^{3} \frac{1}{K_{ni}S_i}, \qquad (42)$$

where β^* is the effective compressibility, K^* is the effective bulk modulus, ν is Poisson's ratio, E is the Young's modulus, K_{ni} is the joint stiffness, and S_i is the interjoint spacing.

The nonlinear contribution to compressibility and contractancy arises from the stress-dependent normal fracture (or joint) stiffness. This is a hyperbolic variation in fracture closure with changing normal stress. For dolerite, Bandis and others (1983) have compiled K_{ni} data for joint closure in dolerite. The relevant units are (normal stress component)/(fracture closure), or megapascals per centimeter.

For an unjointed medium, or a medium in which the joint spacing is very large, the volumetric strain may be related to the applied confining pressure (P_c) through the elastic moduli:

$$\frac{\Delta V}{V_0} = 3\left(\frac{1-2\nu}{E}\right)P_c. \qquad (43)$$

This equation defines volumetric compression in the case of mechanical isotropy, where both flaws and joints are unavailable for closure. The isotropic compression path is plotted in figure 52.23 and is labeled "unjointed media."

Volumetric strain for a jointed media with the potential for pore-pressure (P_p) development in the joint network may be expressed as:

$$\frac{\Delta V}{V_0} = (P_c - P_p)\beta^* + 3P_p\left(\frac{1-2\nu}{E}\right). \qquad (44)$$

When combined with equation 42, the strain becomes

$$\frac{\Delta V}{V_0} = 3(P_c - P_p)\left(\frac{1-2\nu}{E}\right) + \sum_{i=1}^{3} \frac{1}{K_{ni}S_i} + 3P_p\left(\frac{1-2\nu}{E}\right). \qquad (45)$$

The compression paths of jointed media are also plotted on figure 52.23, and the curve for $P_p = 0$ lies to the right of a family of curves that describe contractancy with fluid pressure in the fracture network. The area between the isotropic path and the compression path for $P_p = 0$ has been shaded and represents the expected contractancy range for joint sets whose essentially infinite spacing is tantamount to elastic isotropy, and the suite of curves for the 30-cm joint spacing labeled "jointed media." This area is thought to represent the spectrum of joint spacings relevant to Hawaiian volcanic shields. The jointed media curves generally mimic the nature of the pressure dependence of contractancy as seen in the V_p-versus-confining-pressure behavior in figures 52.16 and 52.17, for instances of microfracture closure under laboratory conditions. Particularly well developed is the characteristic form of $\partial(\Delta V/V_0)/\partial P$ at the lowest pressures shown.

Applied pore pressures have three effects. First, increases in fluid pressure force the volumetric-strain curves progressively to the left (fig. 52.23). This effect is expected because pore pressure stabilizes open fractures at depth, preventing less aggregate compression for a given confining pressure. Second, the relative effect of a fixed pore pressure diminishes progressively as the confining pressure is increased. This effect is illustrated by the convergence of

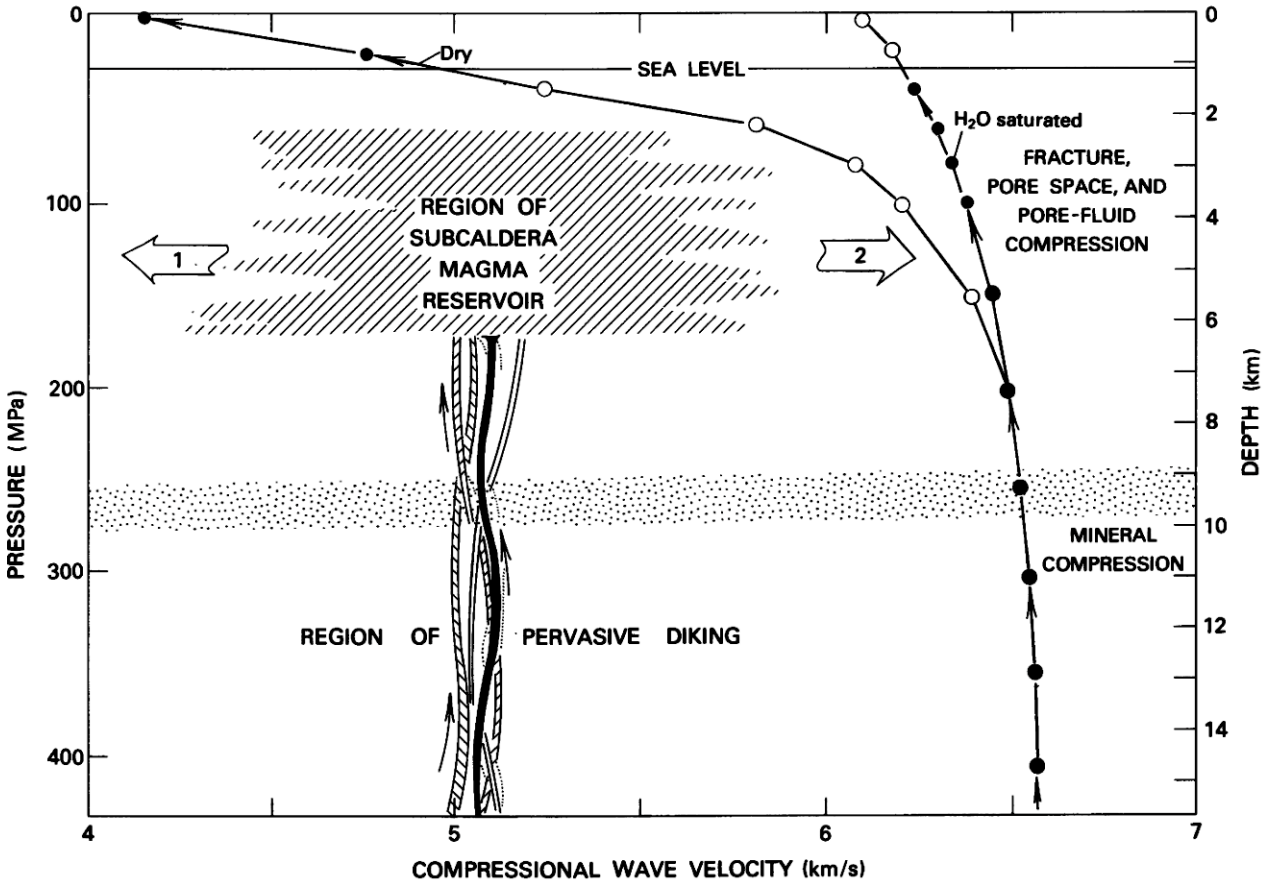

FIGURE 52.22.—Contractancy of basalt in relation to depth distribution of primary magmatic storage within Kilauea. Compressional-wave velocities have been compiled from data of Christensen (1974) and Christensen and Salisbury (1975). Filled and open circles track pathway of V_p as a function of depth and pressure in H_2O-saturated and dry environments, corresponding to changes in depth from upper mantle, oceanic crust, volcanic shield, and submarine reference points to subaerial positions. Filled circles correspond to measurements of relevant decompression track for Kilauea. Stippled band represents a contractancy transition zone, above which pore fluids are continuously squeezed out by increasing levels of confining pressure, and below which fluid-accessible porosity has been eliminated. Accordingly, transition zone defines a contractancy map with two subfields: at shallow depths (0–8 km), dominant mechanism is compression of fractures, pore space, and pore fluids; at greater depths (>9 km), dominant mechanism is mineral compression. Stratigraphic extent of magma storage reservoir has been constrained by geodetic and seismic studies and lies mostly in 2.2- to 6-km-depth interval, corresponding to crossruled region. It is coincident with that portion of contractancy field characterized by fluid-accessible fracture space. Horizontally directed arrows (1 and 2) infer lateral injection of magma into adjacent rift zones. Depth extent of these active rift systems is also coincident with that portion of contractancy map that is associated with fluid-accessible fracture space. Beneath transition zone is a region of mineral compression that is stratigraphically associated with pervasive diking linked with vertical magma movements from mantle depths.

the jointed-media curve set with increasing P_c. Third, at extremely shallow depths, moderate increases in joint fluid pressure drive the curves from the contraction-dominated field into the dilation field. This effect occurs when fluid pressures exceed the confining pressure.

It is of interest now to look at the ways pore-pressure development in the rock microstructure can influence the contractancy of basalt. Christensen (1984) has studied the effects of confining pressure (P_c), pore fluid pressure (P_p), and effective pressure (P_e), where

$$P_e = P_c - P_p, \tag{46}$$

on the compressional and shear wave velocity in basalt. These effects are summarized in figures 52.24 and 52.25, respectively; they are based on the data of Christensen (1984) and represent adaptations

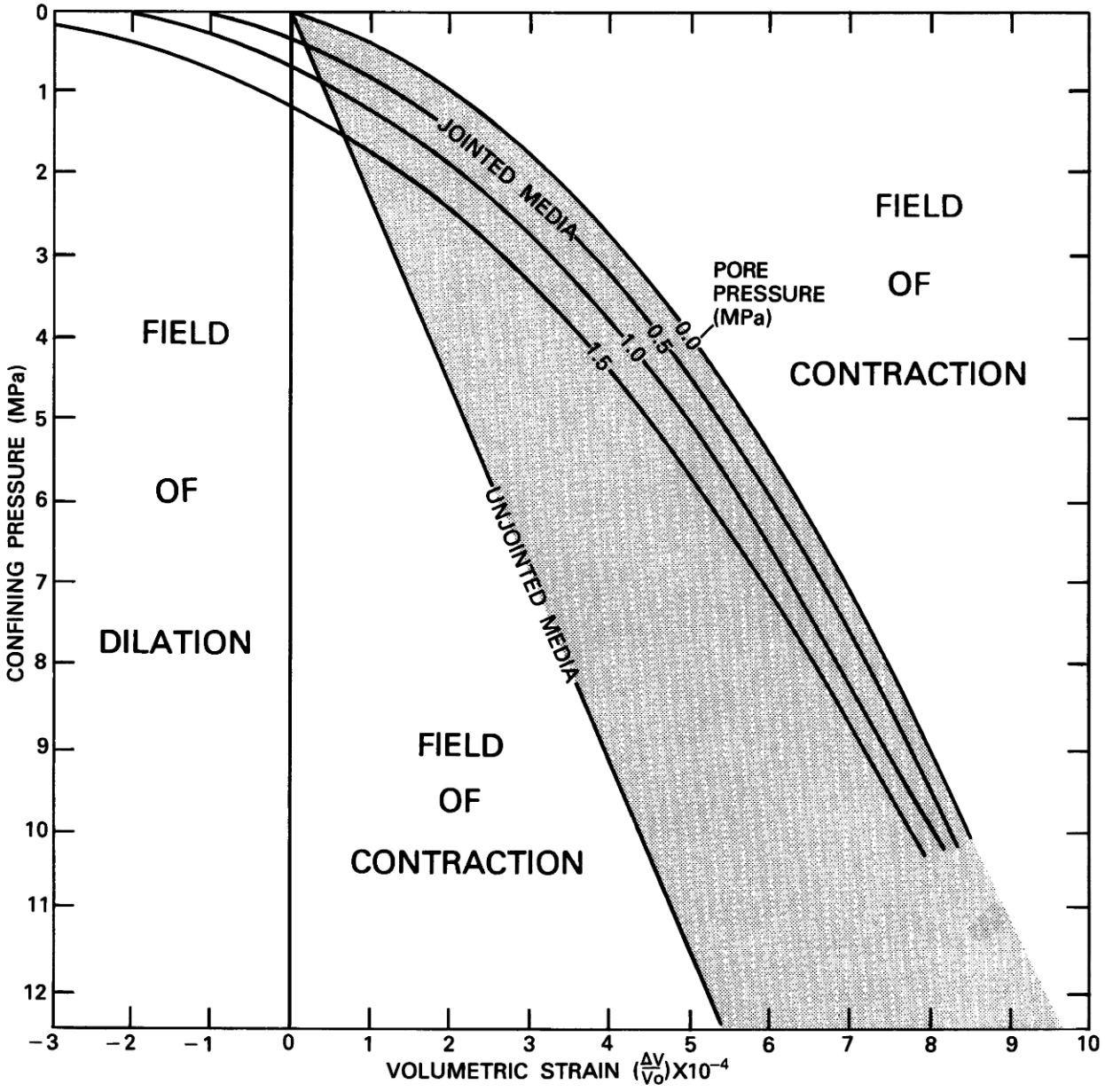

FIGURE 52.23.—Volumetric strain versus confining pressure for unjointed and jointed media with effects of variable pore pressure. Modified from Amadei and Goodman (1981).

of his presentation for reference confining pressures beneath Hawaiian shield volcanoes. In the figures, the familiar nonlinear profile of $\partial V_{p,s}/\partial P$ is produced by the compression of the rock skeleton at zero pore pressure. The hydrostatic reference curve has a fixed low-pressure datum at a depth intermediate between the depth of the summit water table (fig. 52.21*A*) and sea level, for Kilauea as an example. This curve recognizes the temporal and spatial changes in the topography of the intrashield water table and attempts to strike an average. The zero-confining-pressure datum is the volcanic summit. The depth extent encompasses nearly all of the summit magma-reservoir region and most of the rift zones.

The effect of hydrostatic pore pressure shifts the curves to the left, preserving the overall shape of the contractancy profile. Between the P_p = hydrostatic and $P_p = 0$ curves is sandwiched a narrow field where the pore pressure is less than hydrostatic. This field is labeled "C," and it has been shaded in the figures. The pervasive seismicity and rock fracture that characterize the shields of active Hawaiian volcanoes suggest that ambient pore pressures at depth may be inferred to be at or near hydrostatic. To the extent that fluid continuity is maintained by renewed rock fracture, water is expected to be continuously expulsed during the compaction that accompanies volcanic-shield evolution. This general pattern of compaction dewatering should characterize the bulk of the volcanic flanks, where fluid continuity is continuously maintained via the fracture process. For rift-zone environments maintained at near-magmatic temperatures, metamorphism passes through greenschist to amphibolite facies (Liou and others, 1974), and alteration and replacement reactions may be expected to locally close down permeability and promote the development of higher pore-fluid pressures, thus helping, on a local scale, to stabilize open fractures and

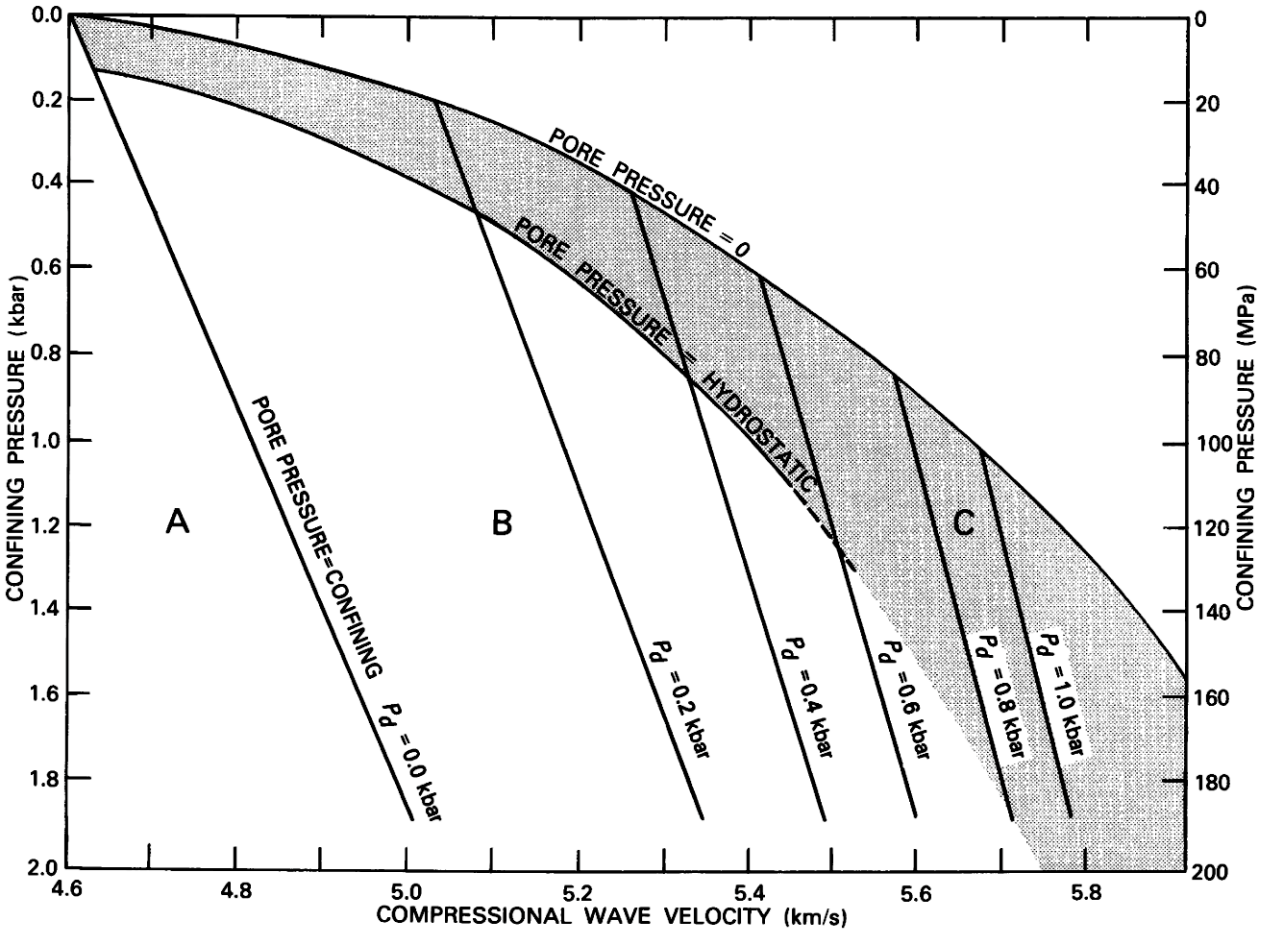

FIGURE 52.24.—Effects of variable pore pressure on compressional-wave velocity in basalt. Fields correspond to mechanically distinct ratios of pore pressure to pressure applied externally to rock skeleton. Field A: pore pressure exceeds external confining pressure; field B: pore pressure is less than confining pressure but greater than hydrostatic; field C: pore pressure is less than hydrostatic. Family of six differential pressure (P_d) lines correspond to 20-MPa (0.2 kbar) increments of difference: ($P_{conf} - P_{pore}$). Figure based on data of Christensen (1984).

pores against the confining pressures that would otherwise squeeze them shut. In figures 52.24 and 52.25, the appropriate region is now the B field, where pore pressures are above hydrostatic. For active regions of intrusion and magmatic storage, one may envision a constant competition between the metamorphic reactions tending to promote the sealing that raises pore pressures above hydrostatic, and the reinstatement of permeability by rock fracture and intrusion, returning the pressure to hydrostatic. In-situ V_p and V_s would then repeatedly shift back and forth across the hydrostatic curve, from field C to field B, and then back again as permeability was alternately enhanced and destroyed. The long-term prognosis, however, is the maintenance of near-hydrostatic pressures for those regions of the shield, where fluids are readily available. These regions are expected to be well above the compression transition zone of figures 52.21*A*, 52.21*B*, and 52.22.

NEAR-SURFACE CONTRACTANCY IN MAGMATIC SYSTEMS

If the dominant mechanism of bulk compression is the continuous elimination of fault, joint, and microfracture porosity in shallow levels of the system, then we should expect to see correlative changes in the density of the volcanic shield with depth, corresponding to increases in confining pressure. The in-situ densities of the volcanic shields of Kilauea and Mauna Loa are plotted in figure 52.26*B*, which is based on the gravity and seismic-refraction surveys of Zucca and others (1982) and the two-dimensional density structure for these volcanoes that resulted from modeling the gravity profile by application of the polygon approach of Talwani and others (1959), with corrections for three-dimensional end effects using the procedure of Cady (1977).

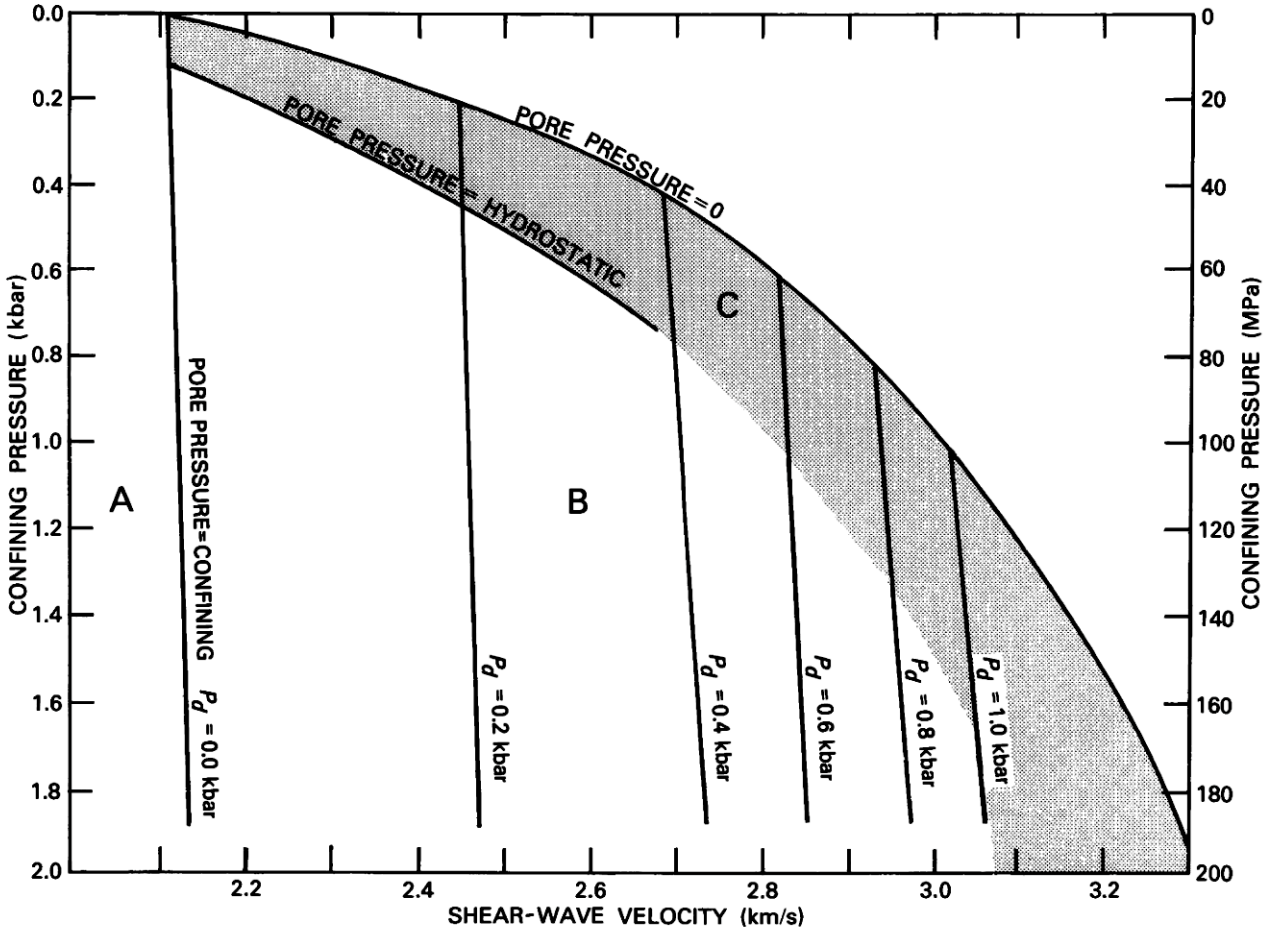

FIGURE 52.25.—Effects of variable pore pressure on shear-wave velocity in basalt. Fields correspond to distinct ratios of pore pressure to externally applied pressure through equivalent lithostatic loading. Field A: pore pressure exceeds external confining pressure; field B: pore pressure is intermediate between confining and hydrostatic; field C: pore pressure is less than hydrostatic. Difference between confining and pore-fluid pressure is differential pressure (P_d) of each of six subvertical lines extending from zero-pore-pressure curve. Figure based on data of Christensen (1984).

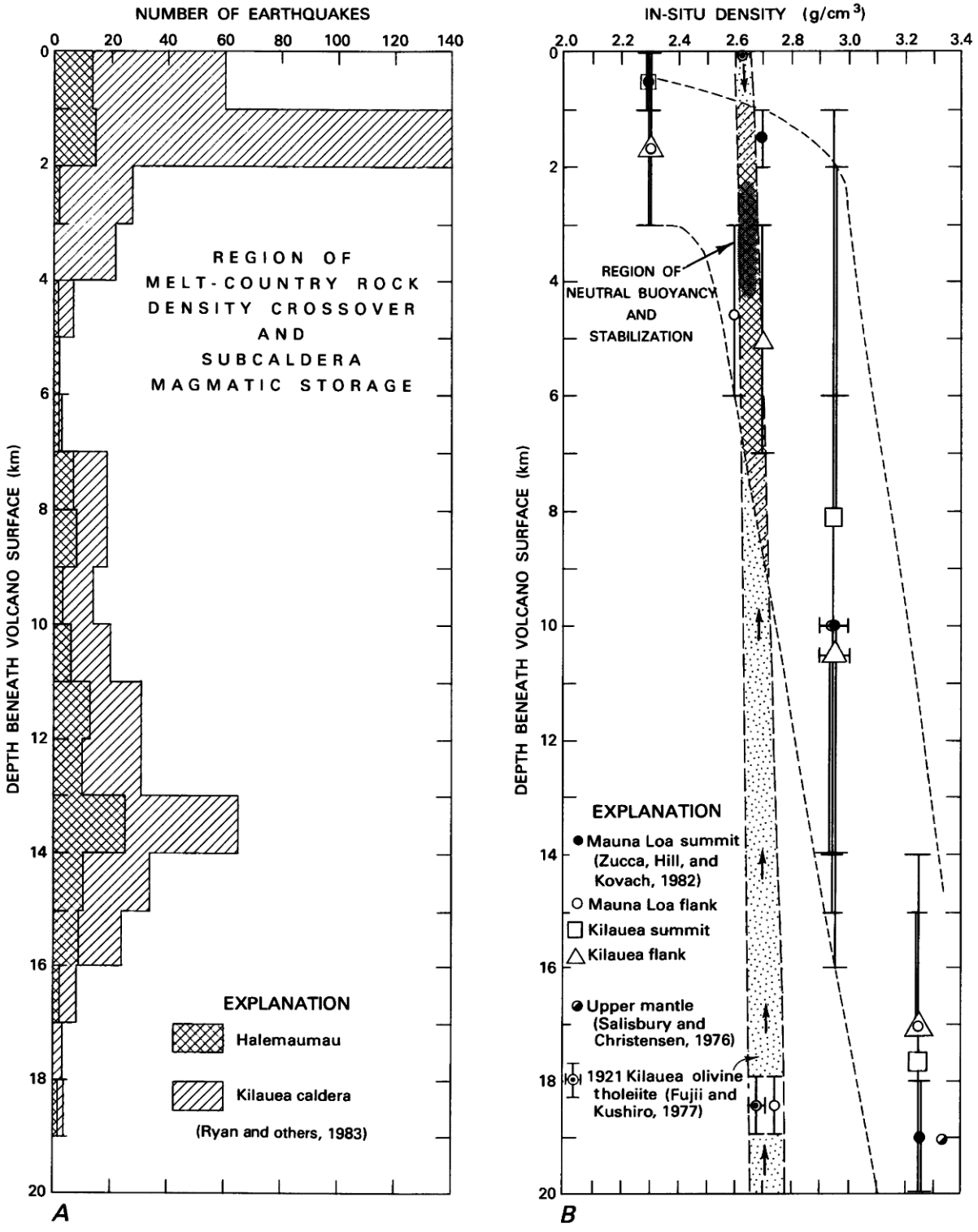
NUMBER OF EARTHQUAKES
0 20 40 60 80 100 120 140
DEPTH BENEATH VOLCANO SURFACE (km)
0 2 4 6 8 10 12 14 16 18 20
REGION OF MELT-COUNTRY ROCK DENSITY CROSSOVER AND SUBCALDERA MAGMATIC STORAGE
EXPLANATION
Halemaumau
Kilauea caldera
(Ryan and others, 1983)
A
IN-SITU DENSITY (g/cm3)
2.0 2.2 2.4 2.6 2.8 3.0 3.2 3.4
DEPTH BENEATH VOLCANO SURFACE (km)
0 2 4 6 8 10 12 14 16 18 20
REGION OF NEUTRAL BUOYANCY AND STABILIZATION
EXPLANATION
Mauna Loa summit (Zucca, Hill, and Kovach, 1982)
Mauna Loa flank
Kilauea summit
Kilauea flank
Upper mantle (Salisbury and Christensen, 1976)
1921 Kilauea olivine tholeiite (Fujii and Kushiro, 1977)
B

The procedure of Talwani and others (1959) enables bodies of varying geometry and dissimilar density to be assembled into a complex composite. For Kilauea and Mauna Loa, this has enabled Zucca and others (1982) to incorporate the effects of the high-density volcanic rift zones and cores in their inversion procedure. These regions are then embedded in the basaltic flanks of the shields, and the computed gravity profiles matched with the observed profiles. The resulting density structure must then be consistent with the seismic-velocity structure inferred from refraction surveys. In turn, the deduced densities have been required to be consistent with the velocity-density systematics at the appropriate confining pressure. In this report, the results of Zucca and others (1982, figs. 10 and 11) have been used in the following way: for each volcano, two vertical density profiles have been taken from the surface to upper mantle depths—one profile beneath the summit caldera and one profile beneath the flanks (fig. 52.26*B*). The symbols for each profile type are provided in the inset box. Vertical bars delimit the stratigraphic extent of the density along the profile. This combined density and velocity structure for both Kilauea and Mauna Loa is consistent with the velocity-density systematics of basaltic, gabbroic, and ultramafic rocks determined independently at 50 and 100 MPa confining pressures (see Christensen and Salisbury, 1975). Collectively, the density profiles define a nonlinear band of values in in-situ density versus depth space. The nonlinear portion of the density band (as determined by the envelope defined by the total density range along a given profile) occurs over the depth interval 0–7 km. This coincides closely with the nonlinear portion of the experimentally derived contractancy curves for basalt and gabbro (figs. 52.16 and 52.17). It also corresponds very closely with the 0 to 9-km-depth interval required to bring about a convergence of the air-saturated and H_2O-saturated branches of the contractancy curve in figure 52.21*B*. Finally, it corresponds closely to the systematics of $\partial V_p/\partial z$ for the seismic-velocity profiles for Hawaii based on the work of Hill (1969), Ward and Gregersen (1973), and Klein (1981), including the low-velocity residuals that lie to the immediate left of the basalt field in figure 52.27. This congruence in depth dependence suggests that several physical states and deduced properties—gravity, density, in-situ seismic velocities and their profiles, and laboratory studies of the pressure dependence of V_p and V_s—are all responding to the nonlinear contractancy associated with the Earth's surface. All are marching to the same drummer: the gradual elimination of void space on all scales with increasing depth.

Plotted also on figure 52.26*B* are measured values of the density of the 1921 Kilauea olivine tholeiite as a function of pressure, based on the work of Fujii and Kushiro (1977). The density range plotted at upper-mantle levels incorporates the experimental uncertainties presented in their figure 18 (p. 442) with the range required to reach their calculated density. At ambient pressure, it is determined by the experimental error. This melt-density band has been stippled in the figure. Particularly significant within the context of contractancy and Hawaiian magmatism is the crossover in melt and country-rock densities at low confining pressure. The melt-density band has been hachured within the crossover region, and the centroid of the crossover with respect to the depth range in country-rock density has been shaded.

At upper-mantle depths, the density contrast between melt and country rock will be a measure of the driving pressure through $\Delta\rho Gh$. In this interval, and through the oceanic crust, this density contrast, $\rho_{rock} - \rho_{melt}$, will be positive, with a continuously diminishing magnitude as melt parcels rise within their dikes. This rise is suggested by the upward-directed arrows (fig. 52.26*B*). As the parcel penetrates the oceanic crust and enters the base of the volcanic shield, the surrounding country-rock will be dominated by basalt and gabbro, and the value of the $\Delta\rho$ will approach zero. Further ascent to a depth level within the heart of the crossover region is expected to bring about a match between melt and environment density. This matching or balance region has been labeled the "region of neutral buoyancy and stabilization" in the figure. The chance passage of melt through the region of neutral buoyancy into the country-rock roof of the reservoir reverses the sign of the density contrast, and $\rho_{rock} - \rho_{melt}$ is now negative. Infinitesimal perturbations above the density balance horizon will return the errant melt parcel to the region of neutral buoyancy (downward-directed arrow). This mechanism—the oscillation of melt parcels about a horizon of density balance—provides for the long-term stabilization of subcaldera magma storage. It is a region where the nonlinear contractancy of rock near the Earth's surface has provided an environment where the critical $\Delta\rho \approx 0$. Breaking the balance and producing significant diking within the roof or eruption at the surface requires the wholesale rupture of the edifice via hydraulic-pressure

FIGURE 52.26.—Earthquake abundance and in-situ density as related to depth beneath volcano surface. ***A***, Distribution of earthquakes beneath Kilauea's summit region. Singly ruled histogram corresponds to depth distribution of seismicity within the volume that encompasses entire Kilauea caldera and extends to 20 km beneath caldera floor. Doubly ruled histogram provides depth distribution of seismicity within prismatic volume that encompasses Halemaumau Crater and extends to 20 km. Aseismic region from 2- to 7-km depth is inferred to have differentially high magma-to-rock ratios. Data from Ryan and others (1983). ***B***, In-situ densities of olivine tholeiite near its liquidus, and volcanic shields, oceanic crustal sections, and upper-mantle bases of Mauna Loa and Kilauea. In-situ densities for Mauna Loa and Kilauea are based on seismic-refraction profiling and gravity surveys of Zucca and others (1982), as resolved by inversion modeling of gravity profiles, consistent with velocity-density systematics of basaltic and gabbroic rocks. Region of density crossover is hachured section of melt-density band. Where band coincides with 2- to 7-km-depth region of subcaldera magma storge, it is doubly hachured. Within centroid of crossover region is a darkly shaded subregion of neutral buoyancy. Data for 1921 Kilauea olivine tholeiite from Fujii and Kushiro (1977), and for upper mantle from Salisbury and Christensen (1976).

increase, tectonic kneading of the reservoir from remotely applied tractions or the reinstatement of a positive $\Delta\rho$ via vesiculation of the melt, or a permutation involving a mix of two or more of these contributors. Reduced to its essentials, the contractancy mechanism suggests a fundamental control on the operation and evolution of magmatic systems in the near-surface environment.

What is the correspondence between the density crossover region and the depth interval associated with subcaldera magma storage? For Kilauea, this interval has been constrained by geodetic studies to occupy the range 2 to 9 km, with the suggestion of the subrange 2 to 4 km, as the most frequently retrieved center of deformation (Mogi, 1958; Eaton, 1962; Fiske and Kinoshita, 1969; Walsh and Decker, 1971; Dieterich and Decker, 1975; Jackson and others, 1975; Swanson and others, 1976; Ryan and others, 1983; Dvorak and others, 1983). The total depth range in the density crossover resolved in figure 52.26*B* is 1 to 7 km, with the central region of neutral buoyancy occupying the 2.5- to 4.5-km-depth range. This depth suggests a good correspondence between the zone of melt/country-rock in-situ density equilibration and the center of magmatic storage inferred from geodetic studies.

Studies of the spatial distribution of subcaldera earthquakes at Kilauea provides a collateral line of independent evidence regarding the depth distribution of magma associated with hydraulic fracturing and its three-dimensional topology. Koyanagi and others (1976) have resolved a relatively aseismic zone, with a mean diameter of about 3 km and a depth range from 3 to 6 km, and have associated this zone with the summit storage reservoir. Ryan and others (1981) have resolved the three-dimensional structure of this region for the period April 1, 1971, to December 31, 1973. These results suggest a reservoir floor in the depth range 6 to 7 km, and a storage complex roof at 2 km. The vertical profiles of the seismicity beneath Kilauea caldera and Halemaumau for this same period (Ryan and others, 1983) have been included in figure 52.26*A*. The roof above 2 km is a zone of intense fracturing, forming a seismic lid on the inflating complex beneath. The interval from 2 to 7 km becomes increasingly aseismic with depth and has a quiet zone in the 4- to 7-km range, suggesting differentially high fluid-to-rock ratios. Beneath 7 km, the level of hydraulically induced fracturing increases, suggesting active transport of magma within the dikes of the primary conduit. The interval from 2 to 7 km in figure 52.26*A* can now be compared with

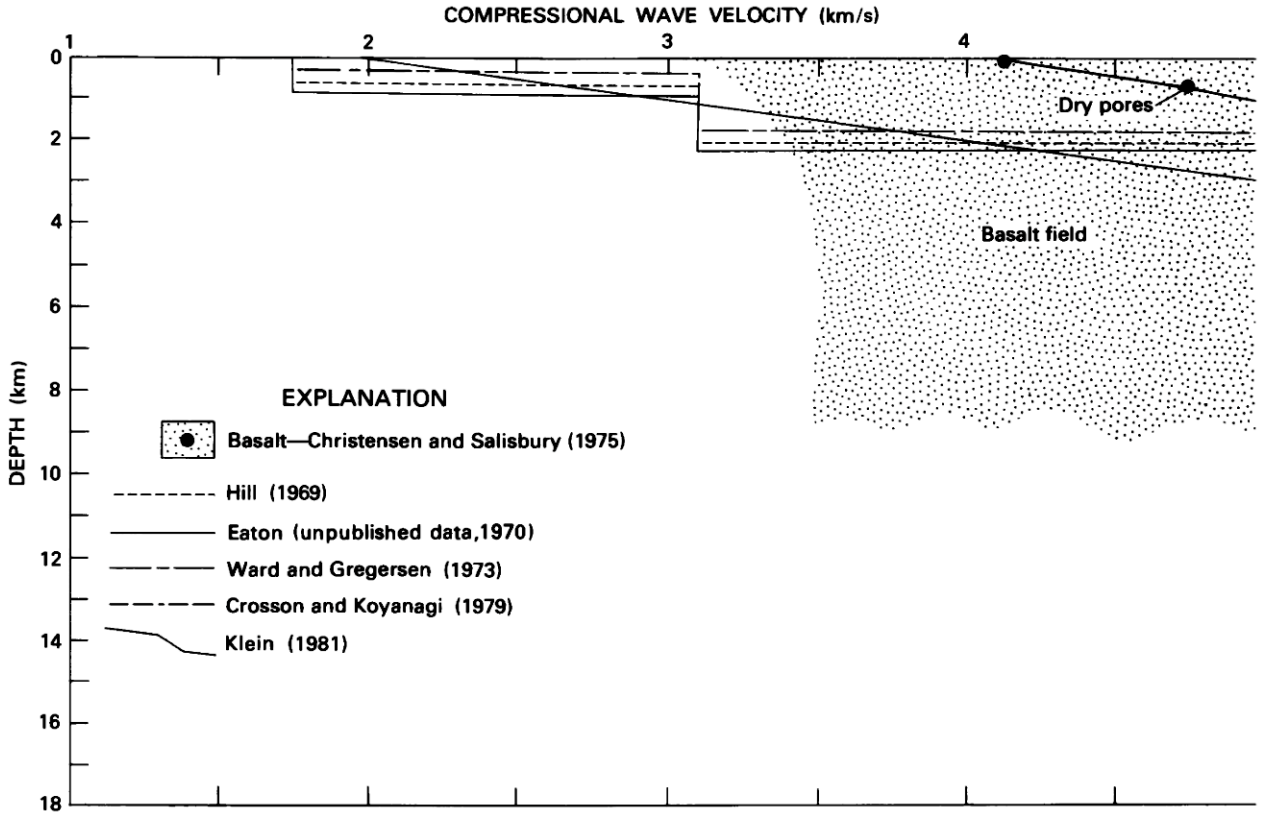

FIGURE 52.27.—Lithologic and seismic compressional wave velocity field beneath Hawaii, with special reference to Kilauea Volcano. Lithologic fields have been compiled from data sets in figures 52.16, 52.17, and 52.18 and references contained therein. Their lateral extents (in V_P space) have been constrained by total ranges in extant compressional wave data as a function of confining pressure. Depth extents of a lithologic field are generally compatible with distribution of seismic velocities with depth, as well as results of gravity surveys and xenolith types in eruptive-vent areas on Hawaii and Oahu. Vertical extent of certain lithologies is expected to be greater than that illustrated, particularly that of gabbro, thus suggesting some overlap between gabbro field and ultramafic fields at upper-mantle

the in-situ melt and country-rock density profiles in figure 52.26*B*. The comparison is striking: there is a 1:1 correspondence between the in-situ density crossover region and the seismically—and geodetically—deduced regions for summit magma storage. Klein and others (1986) resolve the same subcaldera aseismic region. The general relations discussed in this section are summarized in figure 52.28.

CONTRACTANCY AND THE INTERNAL STRUCTURE OF HAWAIIAN VOLCANOES

The discussion of the pressure dependence of the elastic properties of Hawaiian rocks has been largely one dimensional, because the gravitational-force field drives the compression of rocks and orders its variation with depth. Let us now broaden the focus and look at the role of contractancy as it relates to the three-dimensional structure of the magmatic system. Figure 52.29 is a view of the three-dimensional internal structure of Kilauea to 40 km depth. The map scale is 1:62,500, and the physiographic features of Kilauea's surface include: the fracture system of fault blocks, eruptive fissures, and vents of the southwest rift zone and east rift zone; Kilauea caldera, Halemaumau Crater, and major pit craters within the east rift zone; and the major fault systems of the south flank, including the Hilina, Kalanaokuaiki, and Holei palis. Figure 52.30 is a northward-directed view from a depth of 10 km.

The model has been constructed by applying the following constraints:

(1) Seismicity: following the approach of Ryan and others (1981), the three-dimensional distribution of earthquakes associated with magmatic transport and storage has been resolved by plotting their hypocenters within a transparent volume. The period of the study has been January 1, 1969, to January 1, 1983. Uncertainties in event locations have been constrained to be ≤ 1 km. From a total data set of about 50,000 earthquakes, approximately 25,000 have passed the selection criteria of a standard error that is 1 km or less. They are events of magnitude 1.5 and above. Hypocenter locations have employed the linear gradient velocity model of Klein (1981), which is shown in this report to be internally consistent with the pressure dependence of rock properties and the lithology of Kilauea (fig. 52.27).

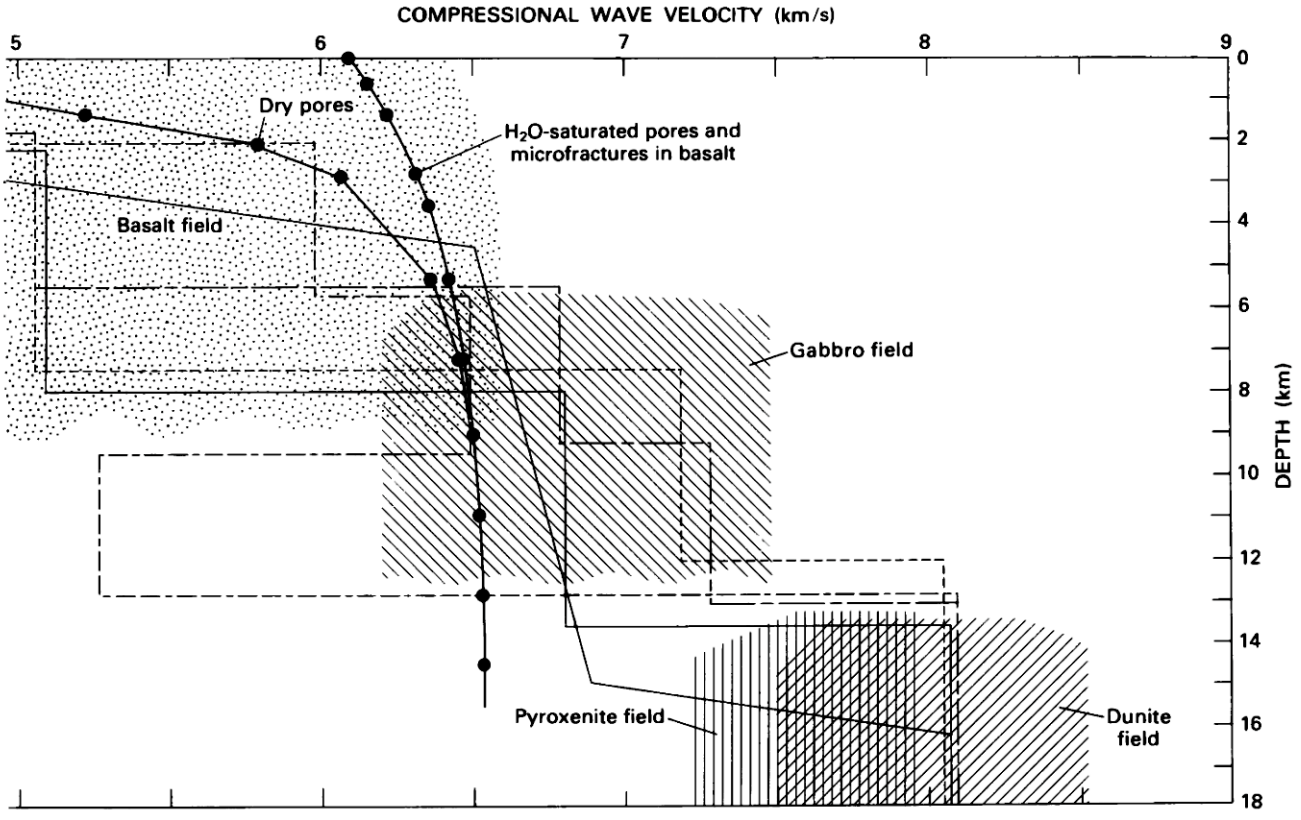

depths, and some additional overlap between gabbro and basalt to within ≈2 km of surface, particularly within core region of volcano. Illustrated field of basalt is constrained laterally by contractancy produced by progressive closure of microfractures and pores with increasing confining pressure. Low seismic velocities outside experimentally determined basalt field suggest contributions from dilatant and partially contracted fracture network associated with free surface of volcano. Base distribution of seismic-velocity profiles has been constructed from profiles of Hill (1969), Eaton (unpublished data, 1970), Ward and Gregersen (1973), and Crosson and Koyanagi (1979) as amended from compilation in Klein (1981).

(2) Geodesy: studies of the deformation associated with rift-zone intrusion have resolved the vertical and horizontal displacement fields generated by the hydraulic inflation of dikes (for example, Jackson and others, 1975; Swanson and others, 1976). These displacement patterns provide essential guidance for the location, strike, and dip of magmatic pressure sources at depth.

(3) Mechanics: the horizontal displacement field for specific intrusive episodes has been modeled for the superstructure of Kilauea at the 1:62,500 scale that corresponds to the model dimensions. The approach uses a finite-element analysis procedure for evaluating the displacement field generated by pressurized discontinuities in an elastic medium. Predicted displacement fields are then examined for consistency with the observed field. Material properties are guided by a combination of in-situ seismic velocities, gravity surveys, and experimental evaluations.

(4) Geology: the distribution of eruptive vents, fissures, and related structures within the rift zones provides collateral constraints on the distribution of magmatic bodies near the surface. Additional guidance is provided by the field study of dikes, sheets, and sills in the dissected shields of ancient Hawaiian volcanoes.

Within the context of this report, the model provides a useful framework for relating the pressure-dependent in-situ properties of the basaltic shield to images of structure and process within and beneath the shield. This framework provides a focal point for applications.

I recognized above that the contractancy of shield volcanoes is influenced by the distribution of faults and fractures in the near surface. Field studies of Kilauea indicate that the fracture networks that influence contractile behavior— and in turn the in-situ V_p, V_s, and density—are heterogeneously distributed. That is, con-

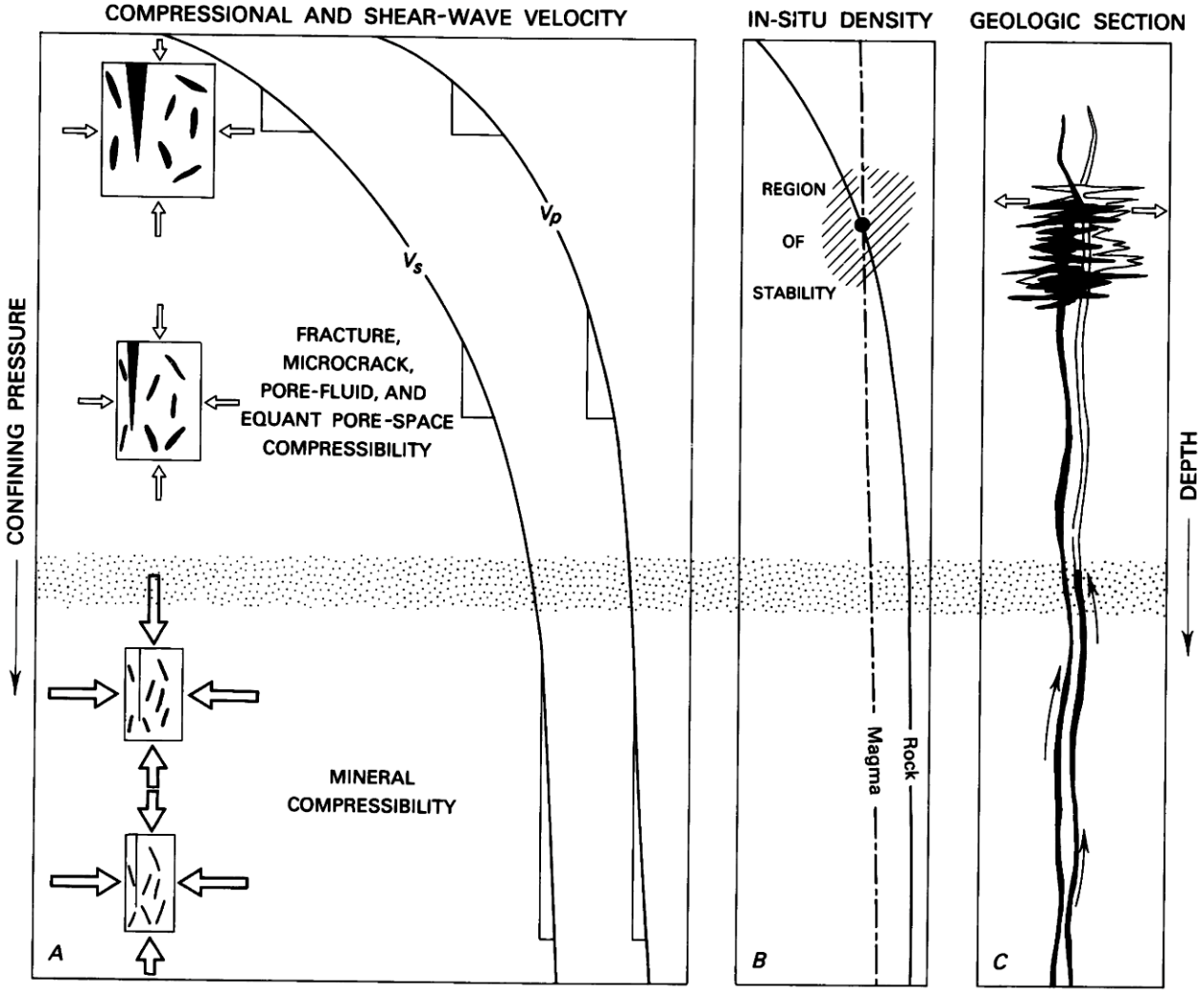

FIGURE 52.28.—*A*, Contributing mechanisms of contractancy in magmatic systems. *B*, Resulting crossover produced in in-situ densities of magma and country rock. *C*, Geologic consequences of a stabilized region with its zone of neutral buoyancy—a subcaldera magma reservoir.

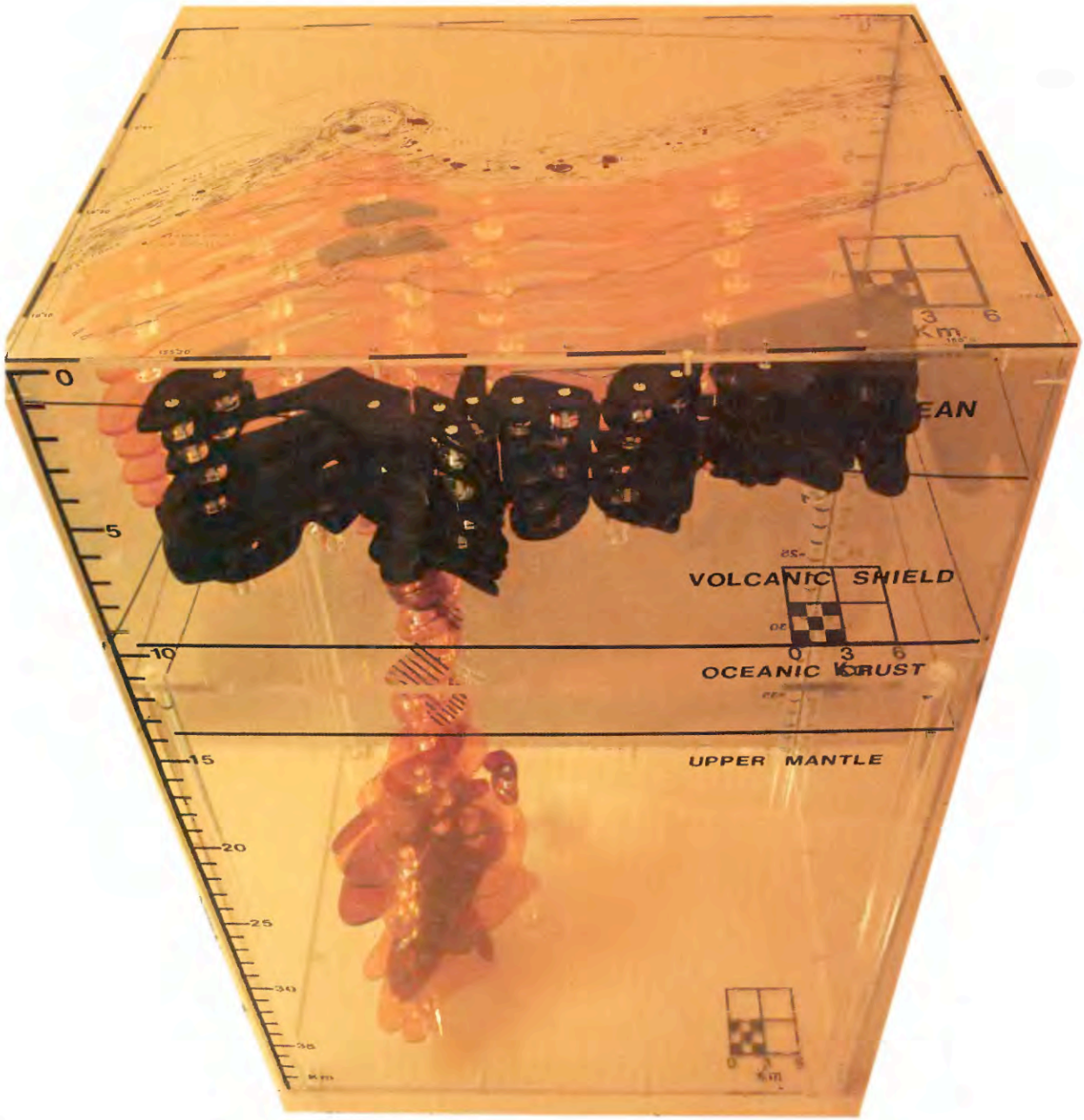

FIGURE 52.29.—Three-dimensional internal structure of Kilauea Volcano, constructed from three-dimensional distribution of earthquakes within and beneath Kilauea, at a map scale of 1:62,500. View orientation is northward, and model extends to 40-km depth. Surface physiography includes fracture systems and eruptive vents of the southwest and east rift zones and Kilauea caldera. Pacific Ocean coastline passes from lower left to middle right. Color coding corresponds to structural elements within the system, as well as temporal variations in hydraulic fracturing associated with magmatic transport from mantle depths. Color-coding format: light to medium amber (within volcanic shield), regions of inferred magmatic movement and storage for period January 1, 1969, to January 1, 1983; maroon, regions of inferred magmatic transport from November 29, 1975, to January 1, 1983; medium amber (within upper mantle), location of magmatic fracture front from January 1, 1969, to November 29, 1975; black, major tectonic blocks within basal levels of volcanic shield, shield-oceanic crust interface, and tectonic blocks of Koae fracture system; hachured amber, levels of low seismic control and uncertainty in geometric constraints. Configuration of major structural subdivisions, including volcanic shield, oceanic crust, and upper-mantle interfaces, is based on work of Hill (1969), Zucca and Hill (1980), and Zucca and others (1982). Vertical scale is 2 times horizontal, allowing an expanded view of geometry of individual level sections.

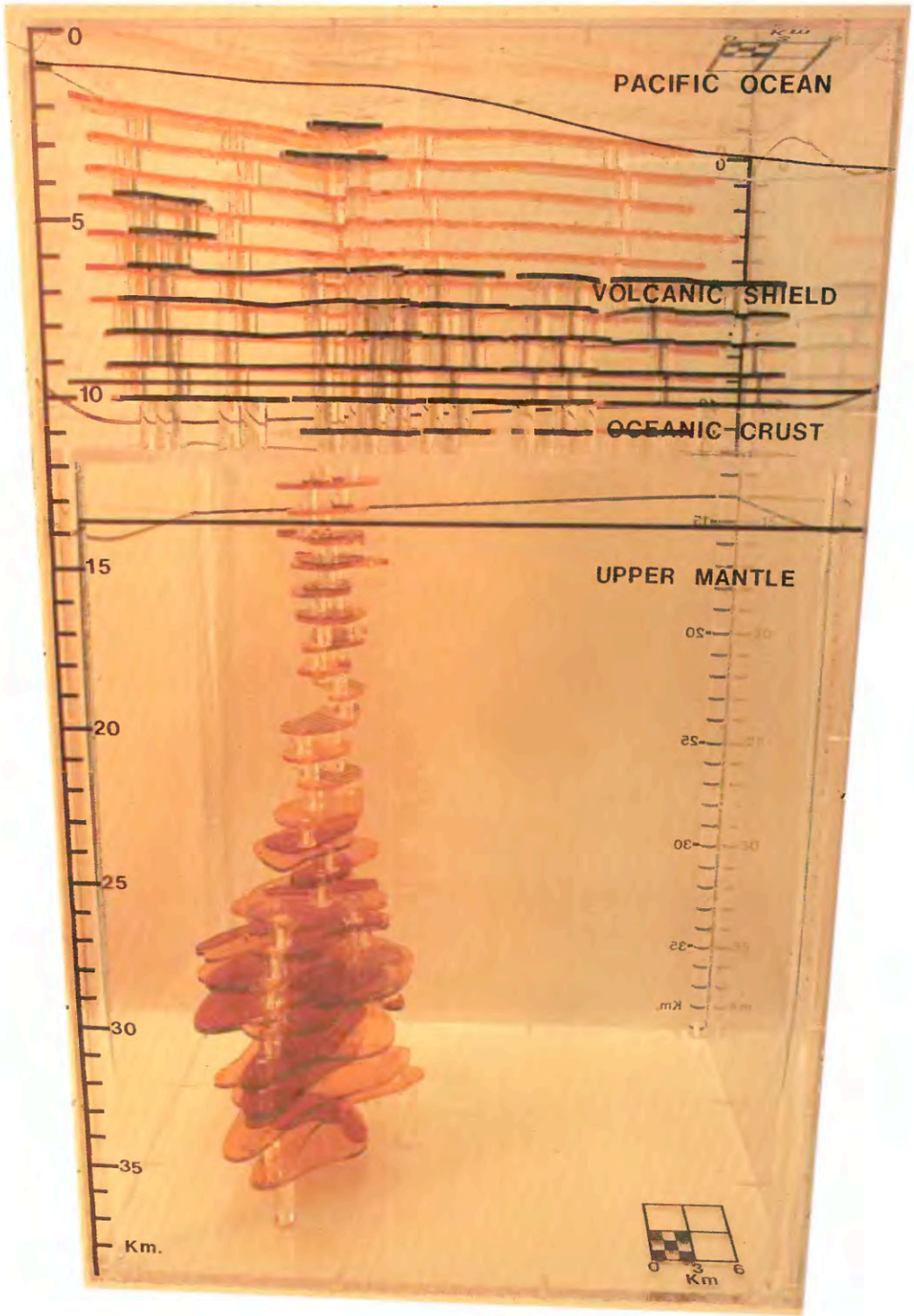
0
5
10
15
20
25
30
35
Km.
PACIFIC OCEAN
VOLCANIC SHIELD
OCEANIC CRUST
UPPER MANTLE
0
3
6
Km

tractancy itself has a three-dimensional structure. It is of interest then to relate these zones of inferred differential rock compression to the three-dimensional structure of the active magmatic system.

The internal structures of the southwest rift zone and east rift zone of Kilauea are resolved in figures 52.29, 52.30, and 52.31. These rift systems appear as medium amber in the figures and extend to the west (left) and east (right), respectively, in these northward-directed views. Their orientation is nearly vertical, and they intersect the surface of the volcano in a region of high fracture density that extends from the "great crack" in the southwest to Heiaheiahulu in the northeast. These fracture systems form in response to the hydraulic inflation of dikes within the rift zones. They record at the surface the differential stretch of rift-zone country rock at depth, as successive intrusive episodes are accommodated. Rift-zone intrusion then produces a zone of differentially contractant (low in-situ V_p, V_s, and ρ) rock above it. It is bounded below by the upper levels of the active dike complex, bounded above by the free surface of the volcano, and elongate along the strike of the rift system. The three-dimensional contractancy structure then mimics the map distribution of the intrusives at depth. Therefore, though rift systems are associated with relatively high densities and seismic velocities at depth, thus reflecting a shift from the velocity structure of the basaltic flanks (fig. 52.16) to the velocities of gabbroic complexes (fig. 52.17), we may expect the thin basaltic veneer of fault blocks above the dike complex to be rather low in in-situ density, V_p, and V_s values (for example, the low-velocity residuals in figure 52.27, to the left of the basalt field).

By analogy with the one-dimensional region of neutral buoyancy plotted in figure 52.26*B*, we may now construct an image of the topography of the three-dimensional neutral-buoyancy surface for Kilauea, relating it to the structure of the magmatic system in figures 52.29, 52.30, and 52.31. Such a surface makes up an in-situ isodensity topography for the interior of the volcano. At points on the surface, $\rho_{rock} - \rho_{melt} \approx 0$, and intrusives have reached density equilibrium positions with respect to the surrounding country rock. Consideration of the two-dimensional density structure resolved by Zucca and others (1982) suggests that, in cross-sectional slices orthogonal to the strike of the rift zone, the profile of neutral buoyancy rises from depth within the flanks to near-surface positions above the rift-zone complex, plunging once again to greater depth once the rift zone is crossed. In three dimensions, such a surface resembles an anticlinal fold, with a fold axis that is coaxial with the strike of the rift system, and a fold wavelength that scales with the rift-complex width. The three-dimensional neutral-buoyancy surface for Kilauea may now be visualized with reference to figures 52.29, 52.30, and 52.31. We would expect it to be draped over both the east and southwest rift systems: rising from depth beneath the south flank palis, passing over the axes of the rifts and caldera, and moving to depth once again beneath the stable north flank. From the summit, the fold axis of the neutral buoyancy surface plunges toward the coastline, following at depth the topography of the volcano, along both the southwest and east rift systems.

MECHANICAL EVOLUTION OF HAWAIIAN SHIELD VOLCANOES

Perhaps the initial suggestion that the summit magma reservoir of Hawaiian shield volcanoes moves progressively upward as the volcano grows was made by Jackson (1968, p. 146), who envisioned:

> A stack of tabular floored chambers representing successive periods of growth [and forming] a cylindrical body of dense rock that could account for the relatively high P wave velocities . . . under the summits.

This suggestion was adopted by Hill (1969, fig. 11, p. 129), who incorporated such a sequence in his summary cross section of a generalized Hawaiian volcano. Fiske and Kinoshita (1969, p. 348) concurred with this view:

> If such a reservoir complex has existed throughout much of Kilauea's history, it is reasonable to assume that the reservoir has migrated to progressively higher levels as the volcano grew to its present size. Today's reservoir would, therefore, be underlain by the sites of former reservoirs, and these would probably consist of dense sills and feeder dikes, containing accumulations of olivine.

It remained for Decker and others (1983, p. 547), however, to provide a convincing demonstration that such an evolutionary pattern is a fundamental theme in the development of Hawaiian volcanoes:

> The similarity between the surface-deformation pattern of the summit areas of Mauna Loa and Kilauea volcanoes is striking . . . The similarity of the morphology and evolution of the calderas on Mauna Loa and Kilauea, and the recent discovery of an apparent caldera on Loihi . . . indicate that the filling and collapse of calderas is a long-lasting and common mechanism in the growth of Hawaiian volcanoes. This conclusion implies that the magma storage zone grows upward from the old sea bottom as the volcano gains in elevation.

FIGURE 52.30.—Three-dimensional structure of Kilauea Volcano, in a northward-directed view from a depth of 10 km beneath summit caldera. Submarine topography of volcanic shield is uppermost light-weight line, deepening eastward (right). Black basal sections of south-flank tectonic blocks lie in front of southwest rift zone, caldera section, and east rift zone, progressing from left to right in 6- to 10-km-depth range. Hydraulic inflation of dikes within these rift systems lever blocks incrementally seaward, toward observer. Oceanic crust is isostatically depressed under primary loading of Mauna Loa, with a 3°–4° dip toward island center, based on seismic-refraction surveys of Hill (1969) and Zucca and Hill (1980). This loading produces crustal warping evident in this view. Contraction of volcanic shield takes place in 0- to 8–9-km-depth interval. Above 8 km, contraction is dominated by compression of macroscopic and microscopic fractures, vesicles, and fracture-filling fluids, including magma, sea water, and fresh water. Beneath 9 km, contraction of shield has been completed, and mineral compression is dominant.

The realization that both Mauna Loa and Kilauea possess a ubiquitous thin veneer of surface material of low in-situ density ($\rho \approx 2.3$ g/cm^3), combined with an appreciation of the density of tholeiitic melt ($\rho = 2.62$ gm/cm^3) at atmospheric pressure, requires a density crossover beneath the surface and poses an additional question. What is the relative position of the subcaldera magma storage reservoir for each of these volcanoes?

Geodetic surveys in the form of horizontal point-to-point distance measurements have been conducted on the summit of Mauna Loa over the period 1977 to 1981 (Decker and others,

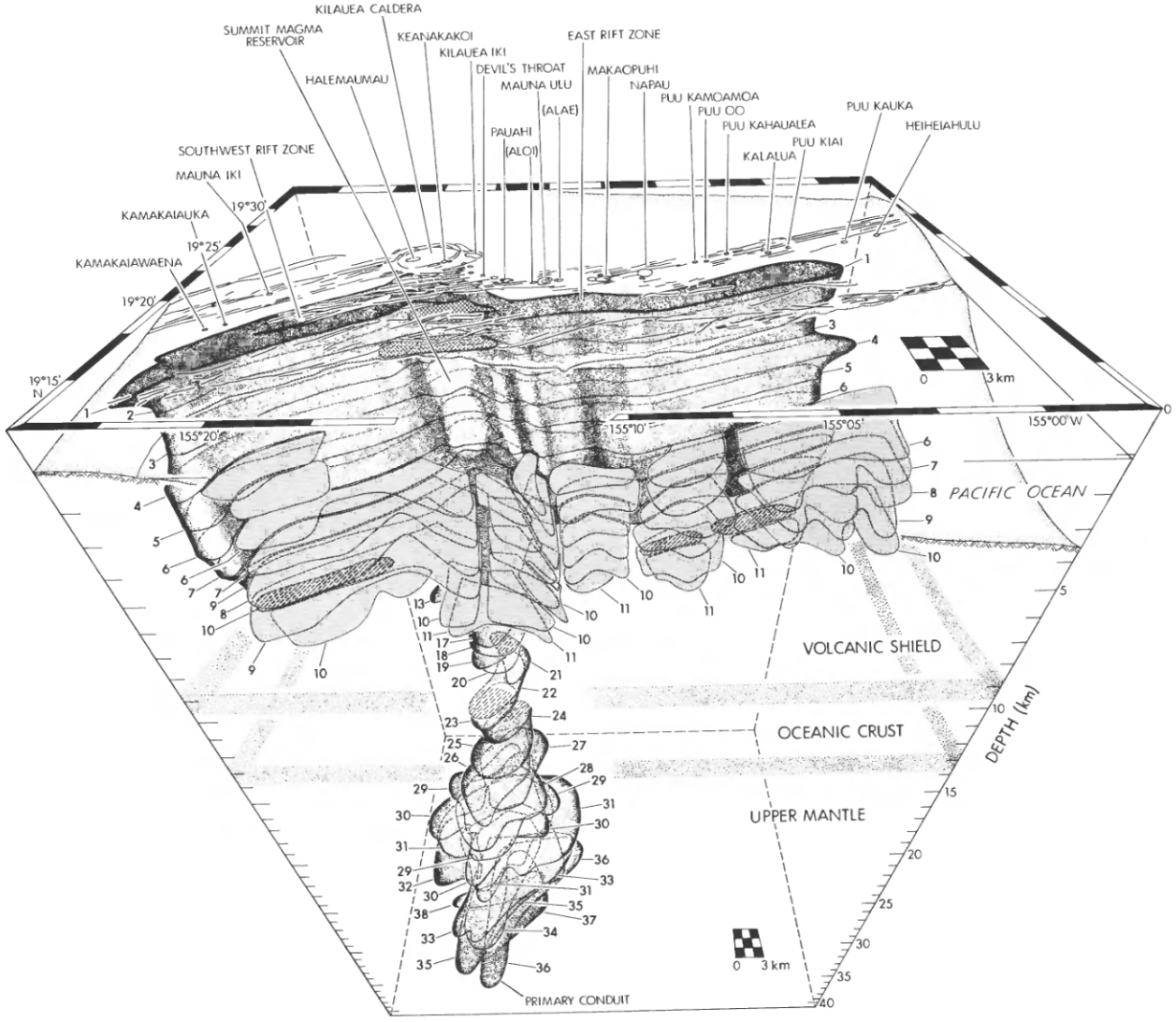

FIGURE 52.31.—Three-dimensional internal structure of Kilauea in a north-directed view from above, as constrained by three-dimensional distribution of earthquakes within and beneath volcano, and analytic mechanics of rift-zone intrusion. Magmatic system within volcanic shield lies to the north (rear) of tectonic blocks of the south flank (even light-gray shading). Influxes of magma within summit reservoir occurs by buoyant rise of melt parcels within primary conduit. Rupture of reservoir wall rock generally occurs at a depth of 3 km beneath caldera floor. This corresponds to region of neutral buoyancy. Dike injection from summit magma reservoir occurs into southwest and east rift zones. During injection process, leading edge of advancing dike propagates along neutral-buoyancy horizon. In general, this lies at a local depth of ≈3 km. Thus, mechanics of lateral dike-injection process are governed by maintenance of a near-constant local depth and neutral-buoyancy principle as pressure increases gained in summit storage are progressively spent. In constructing model, distribution of seismic hypocenters has partially constrained geometric details of rift zones, primary conduit, and south-flank tectonic blocks. Level numbers correspond to individual cross sections. These cross sections are dashed where seismic control is limited. Marine bathymetry has been guided by surveys of Chase and others (1980). Top of magmatic block of rift zone complexes and subcaldera intrusive complex lies at a local depth of 1 km. Between this depth and surface are eruptive fissures and conduits that feed surface activity, such as current eruptive center at Puu Oo. Neutral buoyancy—contractancy-mechanics principle—is viewed as dominant control for producing long rift systems in Hawaiian shield volcanoes. Doubly hachured areas south of caldera are blocks of Koae fracture system.

1983). The inversion of this data set, using the point-source modeling approach of Dvorak and others (1983), suggests an inflation center located at a depth of approximately 3.2 km beneath the caldera floor. Spirit-level tilt measurements taken over the same period suggest, upon inversion, a similar but somewhat shallower depth, 2.6 km (Decker and others, 1983). These surveys defined the geodetic signature of the magmatic pressure increases that led to the outbreak of eruptive activity in March 1984. If we now compare this suggested pressure center with that of its neighbor Kilauea, we see that the depth-below-caldera positions to the summit magma reservoir are remarkably similar: an averaged 2.9 km for Mauna Loa and the range 2–4 km for Kilauea, as discussed earlier. Yet the elevation above sea level for the volcanoes is very different: 4,169 m for Mauna Loa and 1,240 m for Kilauea. The elevation difference in the calderas is then nearly 3 km. Figure 52.32 illustrates the topography of Mauna Loa and Kilauea.

What accounts for this apparently systematic positioning of summit magma storage in these very different volcanoes? Our survey and discussion of the pressure dependence of the in-situ mechanical properties of basaltic and gabbroic rock offer a mechanical rationale. Reduced to its essentials, the contractancy model deals with a dilatant-free surface that is loaded gravitationally. Increases in depth then correspond to increases in lateral confining pressure, as the dilatant fracture space is progressively squeezed shut. A reconsideration of figures 52.21*B* and 52.26*B* suggests that it is the depth below the free-surface reference level that orders the amount of fracture permeability for such dilatant regimes. This reasoning accords well with the role of confining pressure on permeability suggested by Gangi (1978) and Walsh (1981) and implicit in the experiments of Christensen (1974).

A comparison of the relative positioning of subcaldera magma reservoirs in relation to volcanic stature and age turns our attention to

FIGURE 52.32.—Summit caldera of Kilauea (K) in relation to its older neighbor to northwest, Mauna Loa (M). Elevation of Mauna Loa's summit (4,169 m) contrasts with Kilauea's (1,240 m). Similarity in depths of magmatic pressure centers and regions of neutral buoyancy for each volcano (Kilauea, 2–4 km; Mauna Loa, ≈2.9 km) suggests that during evolution of Hawaiian shields, summit reservoir climbs progressively upward. This upward progression is regulated by contractancy of volcanic shield. This mechanism produces increases in confining pressure at fixed reference depths during shield building. Reservoir region may then be viewed as being squeezed upward during maturation process. Hence, shield contractancy has produced a reservoir within Mauna Loa whose upper levels are now at same elevation as Kilauea's summit region (that is, 3 km beneath Mokuaweoweo caldera). Older edifice of Hualalai (H) lies still farther northwest. In foreground is community of Volcano, Hawaii. Photograph by James Griggs.

the south of Kilauea—to Loihi Seamount. Geophysical data in the form of geodetic surveys analogous to those routinely conducted on Kilauea and Mauna Loa are nonexistent, and available seismic data are insufficient to provide the required constraints on the existence and nature of a potential magma-storage region within Loihi's edifice. Bathymetric surveys in the form of sonar mapping and Angus bottom photography have resolved, however, the presence of two radial rift zones and a summit crater complex at an elevation of 980 m below sea level (Malahoff, chapter 6; Malahoff and others, 1982). By analogy with its neighbors to the north, an edifice magma storage capability of modest dimensions may be suggested. Identical conclusions relative to Loihi have been reached by Decker (chapter 42).

The considerations above, coupled with the discussion of the pressure dependence of elasticity and in-situ velocity and density systematics for Hawaiian shield volcanoes, lead naturally to the following proposal for their mechanical evolution. As a shield is formed, the dilatancy produced by diminished lateral constraints within its upper levels produces a contractancy profile. Continued growth and maturation raises the contractancy profile to higher levels, because the origin is always associated with the volcanoes free surface. Stated differently, as a volcano grows, it carries its contractancy profile with it. The upward evolutionary track of contractancy then orders the upward subsurface positioning of the region of neutral buoyancy and the associated magma storage reservoir and its coupled rift systems. This progression, from infancy through middle age to maturity, is illustrated in figure 52.33.

Within a given reservoir, the region of neutral buoyancy will order the positioning of the upper levels of magmatic storage, whereas the basal levels are regulated by the squeezing shut of available fracture permeability. Stated differently, the top of magmatic storage corresponds to the depth level where the compressive

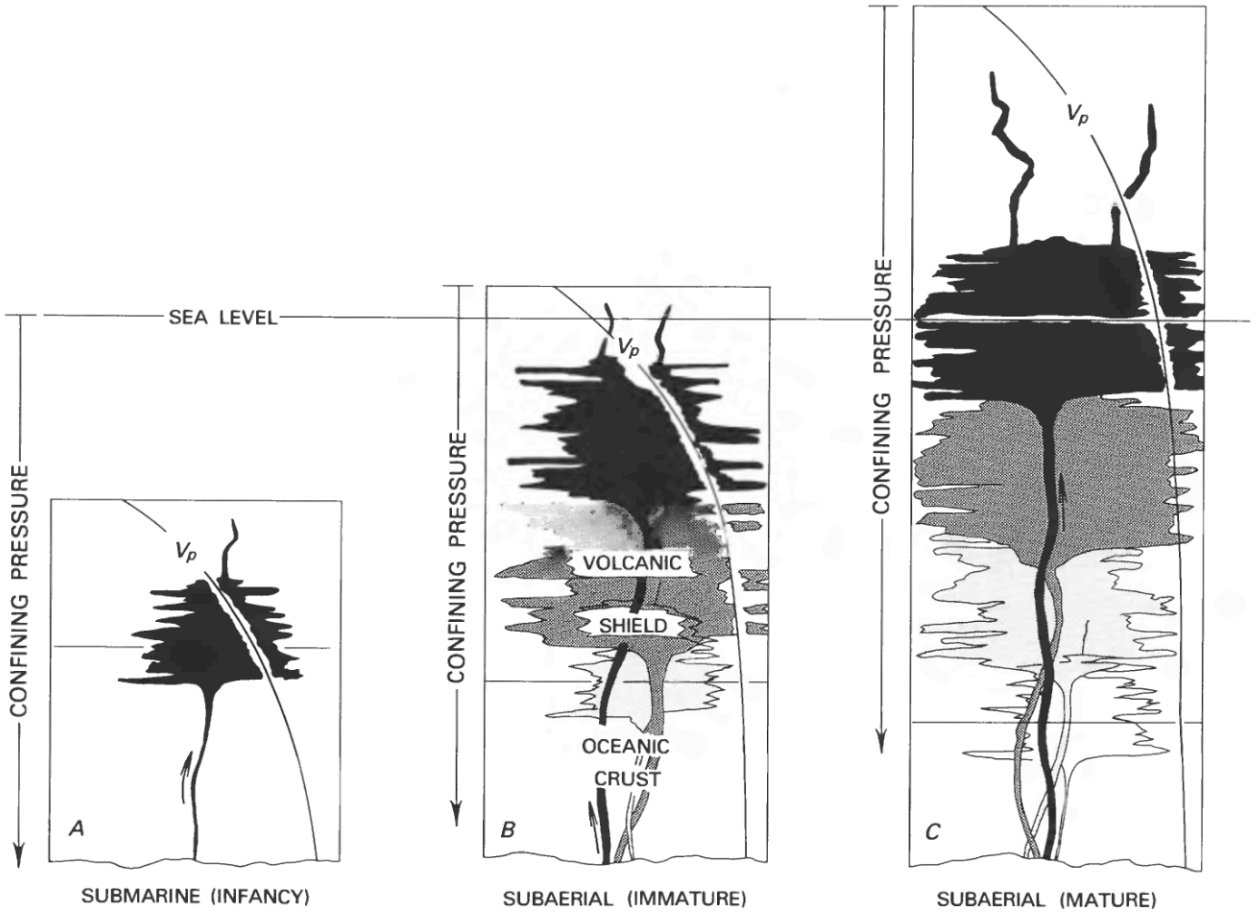

FIGURE 52.33.—Schematic changes in contractancy distribution with depth during growth and evolution of oceanic volcanoes. Volcanic shield-oceanic crust interface is stippled and is isostatically depressed under growing volcanic load. As a volcano grows, it carries its contractancy profile with it. Concomitant changes along this evolutionary track include: (1) progressive upward migration in transition zone that separates fields of fracture and pore-fluid compression above from mineral compression below; and (2) progressive upward migration of zone of neutral buoyancy. These changes provide mechanical rationale for evolutionary climb of subcaldera magma reservoirs in progression from submarine infancy (*A*) through subaerial immaturity (*B*) to subaerial maturity (*C*).

elimination of void space has just begun, and the bottom of the reservoir corresponds to the depth where void-space elimination has been completed. This general correlation is expected to apply to the rift systems as well as the subcaldera reservoir. In light of this relationship, we should expect the summit storage region to be laterally more extensive, with gains in elevation beneath the caldera. In a somewhat crude analogy, the evolving reservoir is lifting itself by its own bootstraps.

THE NATURE OF THE EVOLUTIONARY TRACK

The integration of in-situ seismic-wave velocities, in-situ densities for country rock and tholeiitic melt near its liquidus, magma-reservoir positions from geodetic and seismic studies, volcanic lithology, and structural geology with laboratory data bearing on the pressure and temperature dependence of elasticity leads to a set of empirical relations that unify the observations. When this type of information is compiled for Mauna Loa, Kilauea, and Loihi Seamount—each in a distinctive phase of its evolutionary progression—a set of further empirical relationships is discovered. These relations, presented below, provide the mechanical linkage between volcanic evolution and in-situ rock behavior. They form the basic correlations and postulates of the contractancy model.

Relation 1.—The datum for confining pressure is positioned at the volcanic summit and at the crest of the rift systems. As the volcano grows this datum is progressively raised. In the interior of the volcano, the depth level required to achieve a given confining pressure is simultaneously elevated. During the growth of the shield, the transition zone that separates the relatively shallow field of fracture and pore-fluid compression from the deeper field of mineral compression is therefore progressively elevated. This transition region will have a three-dimensional topography and should be controlled by the stature of the volcanic shield above it. It is expected to be broadly associated with the base of the subcaldera storage complex and the basal section of the rift zones.

Relation 2.—The surficial veneer of low in-situ V_p, V_s, and density is progressively elevated during growth. Formed principally by the macroscopic fracture network in the upper 2 km of the shield, it produces an associated region of density crossover between the country rock and near-liquidus melt. This region of neutral buoyancy provides a mechanically stable environment for the subcaldera storage of magma. Increases in volcanic stature then elevate this region during the maturation process. For Kilauea and Mauna Loa, the geodetically and seismically constrained regions of subcaldera magma storage have a 1:1 correspondence with the region of neutral buoyancy. The stability of intra-rift-zone magmatic storage is expected to adhere to this general principle.

Relation 3.—The thickness of the reservoir roof, determined principally by the depth level of the region of neutral buoyancy, is expected to remain roughly constant as growth proceeds. To first order, this approximate constancy in thickness, mean composition, gross crack density per unit volume, and the pressure-temperature (P,T) environment suggests broadly comparable volumetric strengths. These relations are compatible with the observation of essentially concurrent and progressive caldera collapse as the edifice evolves.

Relation 4.—The progressive and proportional enlargement of the caldera region during shield evolution suggests that the region of neutral buoyancy spreads radially as the shield grows. For Mauna Loa, Kilauea, and Loihi, this spreading is elliptical in plan form, with a major axis that is guided in part by the pervasive influence of the rift systems that originate beneath the caldera.

Relation 5.—The progressive closure of macroscopic and microscopic fractures with depth, as well as the continued compression and expulsion of pore fluids, will systematically raise the in-situ values of the bulk modulus (K), the shear modulus (μ), and the Young's modulus (E). Poisson's ratio (ν) will also vary with depth, because it reflects the ratio of in-situ lateral strains to the axial strains induced by the overburden. These changes track the experimentally determined changes in V_p and V_s with pressure and the in-situ variations of seismic-wave velocities with increasing depth. The progressive closure of fractures with depth will also continuously reduce the amount of bulk anelasticity and simultaneously increase the appropriateness of the continuum assumption employed in mechanical analyses.

Relation 6.—During the seamount phase of oceanic shield development, the bottom of the contractancy curve is expected to lie within the oceanic crust. Continued upward growth of the shield will elevate the compression transition zone to the level of oceanic crustal layer one, where the deepest levels of fracture closure will interact with the low-modulus sediments in controlling the base level of active rift systems. This condition describes the current state of Kilauea Volcano. Further increases in volcanic stature will lift the compression-transition-zone above the old oceanic crust and into the base of the volcanic shield itself. This compression-transition-zone elevation characterizes the current status of Mauna Loa Volcano. Thus, contractancy and the pressure dependence of fracture closure regulates the positions of active-rift-system keels during the mature phase of shield evolution.

SUBMARINE RIFT SYSTEMS AND THE GLOBAL ROLE OF NEUTRAL BUOYANCY

The general association in time and space of rift systems, dike intrusion, dilatant fractures, axial graben, and the neutral buoyancy-contractancy mechanism suggests that this effect may play a fundamental role in the intrusion mechanics and physical evolution of the Earth's oceanic rift systems. Clearly, important differences distinguish Hawaiian rift zones from their counterparts at accretionary plate margins. However, the overall simplicity of the dike-injection process and the primary structures associated with it suggests the following as geologic features of the neutral buoyancy—magma stabilization environment within active rift systems.

(1) Abundant dilatant and deep fissures, aligned parallel with the rift (for example, Ballard and others, 1979; Hey and others, 1985; Renard and others, 1985). Increases in confining pressure with depth will squeeze these fractures shut, increasing the in-situ density and compressional and shear wave velocity. Additional

sealing will be produced by the infilling of sediments and hydrothermal mineralization.

(2) Geomorphic evidence of lava drainback into dilatant fissures (lava-lake terraces, Ballard and others, 1979; and "bathtub" rings, Renard and others, 1985). Large amounts of accessible fracture volume, in turn, suggest significant decreases for in-situ ρ, V_p, and V_s.

(3) Nonlinear increases in compressional-wave velocity in the upper 2 to 3 kilometers within and near the spreading ridge (McClain and Atallah, 1985; Ritzert and Jacoby, 1985; Purdy and Detrick, 1986).

(4) Low aggregate in-situ densities inferred for the upper several hundred meters to 2,000 m.

(5) An axial valley characterized by tensional or downdropped structures.

(6) Gabbroic intrusives that have been emplaced at very shallow depth and subsequently exposed (Fox and others, 1985; Hey and others, 1985).

A consideration of these features prompts the question: What further predictions might the model make? First, a crossover in the in-situ density of basaltic magma and country rock should occur within oceanic rift zones, leading to conditions of neutral buoyancy and mechanical stability. To the extent that a given segment of rift zone was fed from a point source at depth, this would promote the lateral injection of dikes along a shallow horizon of neutral buoyancy. I believe that many sheeted-dike complexes within ancient oceanic crust record the general position of the neutral-buoyancy horizon during their emplacement. A second (and corollary) result is that magmatic eruptions in oceanic rift systems would be appreciably less favored than intrusions. The widespread occurrence of axial grabens suggest a pervasive dike-induced stretch at depth, without the infilling eruptions that would otherwise bury and obliterate these axial valleys. My own field studies on the dynamics of the magma injection-dike formation process in the Gjastykki rift system of the Krafla central volcano, northeastern Iceland, support these inferences. The role of neutral buoyancy in the world's oceanic rift zones is thus a vertically stabilizing one: mechanical equilibrium is achieved between intrusives and their host country rock.

CONCLUSIONS

Experiments conducted to 1,133 K in flexural and torsional resonance have permitted evaluation of the Young's modulus and the modulus of rigidity for Hawaiian olivine tholeiite. The temperature dependence of elasticity for this rock type is very nearly linear. The explicit temperature dependence from regression treatments of replicate runs for each primary mode of mechanical loading is:

Young's modulus,

$$E(T) = (6.054 - 0.00083T) \times 10 \text{ GPa},$$

and *modulus of rigidity,*

$$\mu(T) = (2.615 - 0.00038T) \times 10 \text{ GPa},$$

where T is the temperature in degrees Celsius.

Dilatometric evaluations of linear thermal-expansion coefficients for the same olivine tholeiite yield the value $\alpha_l = 4.58 \times 10^{-6}$ °C^{-1} at 373 K, whereas the expansivity at 973 K is $\alpha_l = 7.93 \times 10^{-6}$ °C^{-1}.

The effects of cyclic heating and cooling histories on the thermal expansivity of olivine tholeiite have been studied in experiments conducted to within 30° of the 1-atm solidus—1,223 K. Parallel comparison runs have been made with diabase in companion experiments. For the basalt, cyclic excursions to 1,223 K induce irreversible thermal strain. One cycle is sufficient to achieve this effect, and repeated cycling to the same maximum temperature induces additional increments of irreversible strain. These permanent dimension changes are interpreted as reflecting the production of successive generations of microfractures during successive visits to high temperatures. The behavior of diabase during cyclic heating and cooling is qualitatively similar: thermal-strain hysteresis with continued cycling. The sense of irreversible thermal strain is different, however, for basalt and diabase: contractile and expansive length changes, respectively. This difference suggests a progressive compaction in the basalt, via microcrack-induced micropore collapse, and a progressive opening of the microstructure of the diabase by microfracture only.

A model has been developed for the high-temperature elasticity of basalt that incorporates the compositional and microstructural dependence of the relevant moduli. Specialized for the major mineral phases of tholeiitic basalt in this report, it is general in nature and is applicable to other rock types. Tabulated values of the elastic properties of olivine, clinopyroxene and orthopyroxene, and plagioclase provide a basis for immediate extensions to mafic and ultramafic rock types of relevance to Hawaii.

The model incorporates the following parameters and capabilities:

(1) Compositional: the aggregate may be monomineralic or consist of an assemblage of n-multiple phases. There are no conceptual limitations on either the mineralogy or the number of phases. Required input data should be either the directionally dependent elastic stiffness and compliance coefficients or the mineral V-R-H-averaged bulk modulus and rigidity. The ultimate limitations on the number of mineral components reduces to the familiar problem of the availability of reliable input data. The model provides predictions of aggregate bulk (K), shear (μ), and Young's (E) moduli.

(2) Microstructural: the compositional model is complemented by incorporating the voids and flaws that weaken the solid and lower the moduli. For basalt, these voids are dominated by the vesicles produced during posteruption degassing. Spherical voids approximate the vesicles. Calculations with needle-shaped voids approximate the geometry of certain grain-edge microfractures. Volume fractions within each category are adjustable and may be guided, for example, by petrographic thin-section examination. The model is readily extendable to incorporate flat microfractures.

(3) Thermal: the temperature dependence is incorporated by introducing the temperature derivative for each contributing mineral phase. Specifically required is the temperature dependence for the bulk modulus (dK/dT) and the modulus of rigidity($d\mu/dT$). Each

contributes to the aggregate behavior through its weighted average. The model may be extended to incorporate pressure dependence by an application of the V-R-H-averaged pressure derivatives as outlined in Graham and Dobrzykowski (1976).

The effects of pressure on the elasticity of basalt provide a basis for developing the contractancy model of the mechanical behavior of shield volcanoes. The model provides a unifying framework that relates the following physical states and derivative properties: (1) the velocity-confining pressure systematics in laboratory samples for V_p and V_s; (2) the in-situ velocity-stratigraphy systematics for seismic profiles beneath the Island of Hawaii; (3) the in-situ density-stratigraphy structure through the Island of Hawaii, as inferred from studies of gravity profiles over summit, rift zone, and flank environments; and (4) the structural geology of Hawaiian shield volcanoes, with particular reference to caldera and rift-zone structure, and their fracture networks.

Additional coherence is suggested by the contractancy model: within Kilauea and Mauna Loa Volcanoes, a crossover occurs between the in-situ density of tholeiitic melt near its liquidus and the in-situ density of the country-rock environment in the subcaldera magma reservoir. The crossover occurs in the nonlinear region of the contractancy profile; that is, at confining pressures that are generally less than 200 MPa (2 kbar). In the core of the density crossover is a region of neutral buoyancy. Here $\rho_{rock} - \rho_{melt} \approx 0$. This mechanism suggests that contractancy provides the fundamental control on the long-term stability of these reservoirs. For Kilauea and Mauna Loa, the geodetically constrained magma-storage reservoirs have a 1:1 coincidence with the density crossover region produced by the contractant shields. This coincidence is produced again in the three-dimensional structure of Kilauea's summit reservoir, as constrained by subcaldera seismicity. In addition, and as a logical consequence, shield contractancy (and derivative in-situ density) provides a mechanism for the frequent observation of intrusives that have come to rest at very shallow depths (for example, dikes in rift systems), as inferred in geodetic-inversion studies and as directly observed in dissected Hawaiian rift systems. Finally, the progressively contractant behavior of Hawaiian shield volcanoes with depth and the attendant in-situ density progression that it implies provide the mechanical rationale for the physical evolution of their subcaldera magma reservoirs as the maturation process continues.

REFERENCES CITED

Aleksandrov, K.S., Ryzhova, T.V., and Belikov, B.P., 1964, The elastic properties of pyroxenes: Soviet Physics-Crystallography, v. 8, no. 5, p. 589-591.

Amadei, B., and Goodman, R.E., 1981, A 3-D constitutive relation for fractured rock masses, *in* Selvadurai, A.P.S., ed., Mechanics of structured media: Amsterdam, Elsevier, p. 249-268.

Anderson, O.L., Schreiber, E., Liebermann, R.C., and Soga, N., 1968, Some elastic constant data on minerals relevant to geophysics: Review of Geophysics, v. 6, p. 491-524.

Arndt, J., and Häberle, J., 1973, Thermal expansion and glass transition temperatures of synthetic glasses of plagioclase composition: Contributions to Mineralogy and Petrology, v. 39, p. 175-185.

Babuska, V., 1972, Elasticity and anisotropy of dunite and bronzitite: Journal of Geophysical Research, v. 77, p. 6955-6963.

Bajuk, E.I., Valarovich, M.P., Klima, K., Pros, Z., and Vanek, J., 1957, Velocity of longitudinal waves in eclogite and ultrabasic rocks under pressures to 4 kilobars: Studies in Geophysics and Geodesy, v. 11, p. 271.

Ballard, R.D., Holcomb, R.T., and Van Andel, T.H., 1979, The Galapagos rift at 86°N, 3. Sheet flows, collapse pits and lava lakes of the rift valley: Journal of Geophysical Research, v. 84, p. 5407-5422.

Bandis, S.C., Lumsden, A.C., and Barton, N.R., 1983, Fundmentals of rock joint deformation: International Journal of Rock Mechanics and Mining Sciences and Geomechanics Abstracts, v. 20, p. 249-268.

Birch, F., 1960, Velocity of compressional waves in rocks to 10 kilobars, Part I: Journal of Geophysical Research, v. 65, p. 1083.

Brace, W.F., Paulding, B.W., Jr., and Scholz, C.H., 1966, Dilatancy in the fracture of crystalline rocks: Journal of Geophysical Research, v. 71, p. 3939-3956.

Breyer, H., 1930, Über die Elastizität von Gesteinen: Zeitschrift für Geophysik: Heft, v. 2, p. 98-111.

Brown, S.R., and Scholz, C.H., 1985, Closure of random elastic surfaces in contact: Journal of Geophysical Research, v. 90, p. 5531-5545.

Budiansky, B., 1965, On the elastic moduli of some heterogeneous materials: Journal of the Mechanics and Physics of Solids, v. 13, p. 223-227.

Budiansky, B., and O'Connell, R.J., 1976, Elastic moduli of a cracked solid: International Journal of Solids and Structures, v. 12, p. 81-97.

Bulau, J.R., Waff, H.S., and Tyburczy, J.A., 1979, Mechanical and thermodynamic constraints on fluid distribution in partial melts: Journal of Geophysical Research, v. 84, p. 6102-6108.

Cady, J.W., 1977, Calculation of gravity and magnetic anomalies along profiles with end corrections and inverse solutions for density and magnetization: U.S. Geological Survey Open-File Report 77-463, 110 p.

Chase, T.E., Miller, C.P., Seekins, B.A., Normark, W.R., Gutmacher, C.E., Wilde, P., and Young, J.D., 1980, Topography of the southern Hawaiian Islands: U.S. Geological Survey Open-File Map 81-120, 3 pls.

Christensen, N.I., 1966, Elasticity of ultrabasic rocks: Journal of Geophysical Research, v. 71, p. 5921-5931.

———1971, Fabric, seismic anisotropy and tectonic history of the Twin Sisters dunite: Geological Society of America Bulletin, v. 82, p. 1681.

———1973, Compressional and shear wave velocities in basaltic rocks, DSDP leg 16, *in* Van Andel, T.H., Heath, G.R., and others, eds., Initial reports of the Deep Sea Drilling Project: U.S. Government Printing Office, v. 16, p. 647-649.

———1974, The petrologic nature of the lower oceanic crust and upper mantle, *in* Kristjansson, L., ed., Geodynamics of Iceland and the North Atlantic area: Dordrecht, Netherlands, D. Reidel, p. 165-176.

———1976, Seismic velocities, densities and elastic constants of basalts from DSDP leg 35, *in* Hollister, C.D., Craddock, C., and others, eds., Initial reports of the Deep Sea Drilling Project: U.S. Government Printing Office, v. 35, p. 335-337.

———1978, Ophiolites, seismic velocities and oceanic crustal structure: Tectonophysics, v. 47, p. 131-157.

———1984, Pore pressure and oceanic crustal seismic structure: Geophysical Journal of the Royal Astronomical Society, v. 79, p. 411-424.

Christensen, N.I., Carlson, R.L., Salisbury, M.H., and Fountain, D.M., 1975, Elastic wave velocities in volcanic and plutonic rocks recovered on DSDP leg 31, *in* Kraig, D.E., Ingle, J.C., and others, eds., Initial reports of the Deep Sea Drilling Project: U.S. Government Printing Office, v. 31, p. 607-609.

———1974a, Velocities and elastic moduli of volcanic and sedimentary rocks recovered on DSDP leg 25, *in* Simpson, E.S.W., Schlich, R., and others, eds., Initial reports of the Deep Sea Drilling Project: U.S. Government Printing Office, v. 25, p. 357-360.

———1974b, Velocities of compressional and shear waves in DSDP leg 27 basalts, *in* Veevers, J.J., and Heirtzler, J.R., eds., Initial reports of the Deep Sea Drilling Project: U.S. Government Printing Office, v. 27, p. 445-449.

Christensen, N.I., and Ramananantoandro, R., 1971, Elastic moduli and anisotropy of dunite to 10 kilobars: Journal of Geophysical Research, v. 76, p. 4003.

Christensen, N.I., and Salisbury, M.H., 1972, Sea floor spreading, progressive alteration of layer two basalts, and associated changes in seismic velocities: Earth and Planetary Science Letters, v. 15, p. 367-375.

———1973, Velocities, elastic moduli and weathering-age relations for Pacific layer 2 basalts: Earth and Planetary Science Letters, v. 19, p. 461-470.

———1975, Structure and constitution of the lower oceanic crust: Review of Geophysics and Space Physics, v. 13, p. 57-86.

Coble, R.L., and Kingery, W.D., 1956, Effect of porosity on physical properties of sintered alumina: Journal of American Ceramic Society, v. 39, p. 337-385.

Crosson, R.S., and Endo, E.T., 1982, Focal mechanisms and location of earthquakes in the vicinity of the 1975 Kalapana earthquake aftershock zone 1970-1979: Implications for tectonics of the south flank of Kilauea Volcano, Island of Hawaii: Tectonics, v. 1, p. 495-542.

Crosson, R.S., and Koyanagi, R.Y., 1979, Seismic velocity structure below the Island of Hawaii from local earthquake data: Journal of Geophysical Research, v. 84, p. 2331-2342.

Davis, P.M., Hastie, L.M., and Stacey, F.D., 1974, Stresses within an active volcano—with particular reference to Kilauea: Tectonophysics, v. 22, p. 355-362.

Decker, R.W., Koyanagi, R.Y., Dvorak, J.J., Lockwood, J.P., Okamura, A.T., Yamashita, K.M., and Tanigawa, W.R., 1983, Seismicity and surface deformation of Mauna Loa volcano, Hawaii: Eos, v. 64, p. 545-547.

Dieterich, J.H., and Decker, R.W., 1975, Finite element modeling of surface deformation associated with volcanism: Journal of Geophysical Research, v. 80, p. 4094-4102.

Duffield, W.A., Christensen, R.L., Koyanagi, R.Y., and Peterson, D.W., 1982, Storage, migration and eruption of magma at Kilauea Volcano, Hawaii, 1971-1972: Journal of Volcanology and Geothermal Research, v. 13, p. 273-307.

Dvorak, J.J., Okamura, A.T., and Deiterich, J.H., 1983, Analysis of surface deformation data, Kilauea Volcano, Hawaii: October 1966 to September 1970: Journal of Geophysical Research, v. 88, p. 9295-9304.

Eaton, J.P., 1962, Crustal structure and volcanism in Hawaii, *in* Crust of the Pacific Basin: American Geophysical Union Monograph, p. 13-29.

Eaton, J.P., and Murata, K.J., 1960, How volcanoes grow: Science, v. 132, p. 925-938.

Eshelby, J.D., 1957, The determination of the elastic field of an ellipsoidal inclusion and related problems: Proceedings of the Royal Society of London, ser. A, v. 241, p. 376-396.

Fedotov, S.A., 1977a, Geophysical data on deep-seated magmatic activity below Kamchatka and an estimate of the forces that cause the rise of magmas into volcanoes: International Geology Review, v. 19, p. 661-670.

———1977b, Mechanism of deep-seated magmatic activity below island-arc volcanoes and similar structures: International Geology Review, v. 19, p. 671-680.

———1977c, Ascent of basic magmas in the crust and the mechanism of basaltic fissure eruptions: International Geology Review, v. 20, p. 33- 48.

Fiske, R.S., and Jackson, E.D., 1972, Orientation and growth of Hawaiian volcanic rifts: The effect of regional structure and gravitational stresses: Proceedings of the Royal Society of London, ser. A, v. 329, p. 299-326.

Fiske, R.S., and Kinoshita, W.T., 1969, Inflation of Kilauea Volcano prior to its 1967–1968 eruption: Science, v. 165, p. 341-349.

Fornari, D.J., Malahoff, A., and Heezen, B.C., 1978, Volcanic structure of the crest of the Puna ridge, Hawaii: geophysical implications of submarine volcanic terrain: Geological Society of American Bulletin, v. 89, p. 605-616.

Förster, F., 1937, Ein neues Messverfahren zur Bestimmung des Elastizitäts Moduls und der Dämpfung (New method for determination of modulus of elasticity and damping): Zeitschrift für Metallkunde, v. 29, p. 109-115.

Fox, P.J., Moody, R.H., Karson, J.A., Bonatti, E., Kidd, W.S.F., Crane, K., Gallo, D.G., Stroup, J.B., Fornari, D.J., Elthon, D., Hamlyn, P., Casey, J.F., Needham, D., and Sartori, R., 1985, The geology of the oceanographer transform: The transform domain: Marine Geophysical Researches, v. 7, p. 329-358.

Fox, P.J., and Schreiber, E., 1973, Compressional wave velocities in basalt and dolerite samples recovered during leg 15, *in* Edgar, N.T., Saunders, J.B., and others, eds., Initial reports of the Deep Sea Drilling Project: U.S. Government Printing Office, v. 15, p. 1013-1015.

Fox, P.J., Schreiber, E., and Peterson, J.J., 1973, The geology of the Oceanic crust: compressional wave velocities of oceanic rocks: Journal of Geophysical Research, v. 78, p. 5155-5172.

Frisillo, A.L., 1972, The elastic coefficients of bronzite as a function of pressure and temperature: University Park, Pennsylvania State University, Ph.D. thesis.

Frisillo, A.L., and Buljan, S.T., 1972, Linear thermal expansion coefficients of orthopyroxene to 1000 °C: Journal of Geophysical Research, v. 77, p. 7115-7117.

Fujii, T., and Kushiro, I., 1977, Density, viscosity, and compressibility of basaltic liquid at high pressures: Carnegie Institution of Washington Year Book, v. 76, p. 419-424.

Gangi, A.F., 1978, Variation of whole and fractured porous rock permeability with confining pressure: International Journal of Rock Mechanics and Mining Sciences and Geomechanics Abstracts, v. 15, p. 249-257.

Gold, T., and Soter, S., 1985, Fluid ascent through the solid lithosphere and its relation to earthquakes: Pure and Applied Geophysics, v. 122, p. 492-530.

Graham, E.K., 1969, The elastic coefficients of forsterite as a function of pressure and temperature: University Park, Pennsylvania State University, Ph.D. thesis.

Graham, E.K., and Barsch, G., 1969, Elastic constants of single-crystal forsterite as a function of temperature and pressure: Journal of Geophysical Research, v. 74, p. 5949-5960.

Graham, E.K., and Dobrzykowski, D., 1976, Temperatures in the mantle as inferred from simple compositional models: American Mineralogist, v. 61, p. 549-559.

Grove, T.L., and Baker, M.B., 1983, Effects of melt density on magma mixing in calc-alkaline series lavas: Nature, v. 305, p. 416-418.

Hashin, Zvi, 1964, Theory of mechanical behavior of heterogeneous media: Applied Mechanics Reviews, v. 17, p. 1-8.

Hashin, Zvi, and Shtrikman, S., 1962, A variational approach to the theory of the elastic behavior of polycrystals: Journal of Mechanics and Physics in Solids, v. 10, pp. 343-352.

Hassleman, D.P.H., 1961, Tables for the computation of the shear modulus and Young's modulus of elasticity from the resonant frequencies of rectangular prisms: Niagara Falls, N.Y., Applied Research Branch, The Carborundum Co., 17 p.

Hekinian, R., Auzende, J.M., Francheteau, J., Gente, P., Ryan, W.B.F., and Kappel, E.S., 1985, Offset spreading centers near 12°53'N on the East Pacific rise: Submersible observations and composition of the volcanics: Marine Geophysical Researches, v. 7, p. 359-377.

Herzberg, C.T., Fyfe, W.S., and Carr, M.J., 1983, Density constraints on the formation of the continental Moho and crust: Contributions to Mineralogy and Petrology, v. 84, p. 1-5.

Hey, R.N., Sinton, J.M., Atwater, T.M., Christie, D.M., Johnson, H.P., Kleinrock, M.C., Macdonald, K.C., Miller, S.P., Neal, C.A., Searle, R.C., Sleep, N.H., and Yonover, R.N., 1985, Alvin investigation of an oceanic propagating rift system, Galapagos 95.5°W: Eos, v. 66, p. 1091.

Hill, D.P., 1969, Crustal structure of the Island of Hawaii from seismic-refraction measurements: Bulletin of the Seismological Society of America, v. 59, p. 101-130.

Hill, R.E.T., and Boettcher, A.L., 1970, Water in the earth's mantle: melting curves of basalt-water and basalt-water-carbon dioxide: Science, v. 167, p. 980-982.

Hill, R.W., 1952, The elastic behavior of a crystalline aggregate: Proceedings of the Royal Society of London, ser. A, v. 65, p. 349-354.

———1965, A self-consistent mechanics of composite materials: Journal of Mechanics and Physics of Solids, v. 13, p. 213-222.

Hughes, D.S., and Cross, J.H., 1951, Elastic wave velocities in rocks at high pressures and temperatures: Geophysics, v. 16, p. 577.

Hughes, D.S., and Maurette, C., 1957, Variation of elastic wave velocities in basic igneous rocks with pressure and temperature: Geophysics, v. 22, p. 23.

Hyndman, R.D., 1976, Seismic velocity measurements of basement rocks from DSDP leg 37, *in* Aumento, F., and Melson, W.G., eds., Initial reports of the Deep Sea Drilling Project: U.S. Government Printing Office, v. 37, p. 373-387.

Ide, J.M., 1936, Some dynamic methods for determination of Young's modulus: Review of Scientific Instruments, v. 6, p. 296.

———1937, The velocity of sound in rocks and glasses as a function of temperature: Journal of Geology, v. 45, p. 689-715.

Iida, K., and Kumazawa, M., 1960, Measurements of elastic wave velocities in

volcanic rocks at high temperatures by means of ultrasonic impulse transmission, Part I: Nagoya University, Journal of Earth Science, v. 7, p. 49-64.

Jackson, D.B., Swanson, D.A., Koyanagi, R.Y., and Wright, T.L., 1975, The August and October 1968 east rift eruptions of Kilauea Volcano, Hawaii: U.S. Geological Survey Professional Paper 890, 33 p.

Jackson, E.D., 1968, The character of the lower crust and upper mantle beneath the Hawaiian Islands: International Geological Congress, 23d, Prague, 1968, v. 1, p. 135-150.

Jackson, E.D., Clague, D.A., Engleman, E., Friesen, W.B., and Norton, D., 1981, Xenoliths in the alkalic basalt flows from Hualalai Volcano, Hawaii: U.S. Geological Survey Open-File Report 81–1031, 33 p.

Jackson, E.D., and Wright, T.L., 1970, Xenoliths in the Honolulu Volcanic Series, Hawaii: Journal of Petrology, v. 11, p. 405-430.

Johnson, A.T., and Pollard, D.D., 1973, Mechanics of growth of some laccolithic intrusions in the Henry Mountains, Utah, I: Tectonophysics, v. 18, p. 261-309.

Jones, L.E.A., 1977, High-temperature elasticity of rutile-structure MgF_2: Physics and Chemistry of Minerals, v. 1, p. 179-198.

Kanamori, H., and Mizutani, 1965, Ultrasonic measurements of elastic constants of rocks under high pressures: Bulletin of the Earthquake Research Institute, v. 43, p. 173.

Kern, H., and Rich, A., 1979, Compressional and shear wave velocities at high temperature and confining pressure in basalts from the Faeroe Islands: Tectonophysics, v. 54, p. 231-252.

King, M.S., 1966, Wave velocities in rocks as a function of changes in overburden pressure and pore fluid saturants: Geophysics, v. 31, p. 50-73.

Klein, F.W., 1981, A linear gradient crustal model for south Hawaii: Bulletin of the Seismological Society of America, v. 71, p. 1503-1510.

Koyanagi, R.Y., Unger, J.D., Endo, E.T., and Okamura, A.T., 1976, Shallow earthquakes associated with inflation episodes at the summit of Kilauea Volcano, Hawaii: Bulletin of Volcanology, v. 39, p. 621-631.

Kroenke, L.W., Manghnani, M.H., Rai, C.S., Fryer, P., and Ramananantoandro, R., 1976, Elastic properties of selected ophiolitic rocks from Papua, New Guinea: Nature and composition of oceanic crust and upper mantle, *in* Sutton, G.H., Manghnani, M.H., and Moberly, R., eds., The geophysics of the Pacific Ocean basin and its margins: Washington, American Geophysical Union, v. 19, p. 407.

Kröner, E., 1958, Kontinuumstheorie der Versetzungen und Eigenspannungen: Ergebnisse der Angewandten Mathematik: Springer-Verlag, v. 5.

———1967, Elastic moduli of perfectly disordered composite materials: Journal of the Mechanics and Physics of Solids, v. 15, p. 319-329.

Lambeck, K., and Nakiboglu, S.M., 1980, Seamount loading and stress in the ocean lithosphere: Journal of Geophysical Research, v. 85, p. 6403-6418.

Leibfried, G., and Ludwig, W., 1961, Theory of anharmonic effects in crystals, *in* Seitz, F., and Turnbull, D., eds., Solid State Physics, v. 12: New York, Academic Press, p. 276-444.

Liou, J.G., Kuniyoshi, S., and Ito, K., 1974, Experimental studies of the phase relations between greenschist and amphibolite in a basaltic system: American Journal of Science, v. 274, p. 613-632.

Macdonald, G.A., and Katsura, T., 1964, Chemical composition of Hawaiian lavas: Journal of Petrology, v. 5, p. 82-133.

Malahoff, A., McMurtry, G.M., Wiltshire, J.C., and Yeh, H-W., 1982, Geology and chemistry of hydrothermal deposits from active submarine volcano, Loihi, Hawaii: Nature, v. 298, p. 234-239.

Manghnani, M.H., and Woollard, G.P., 1968, Elastic wave velocities in Hawaiian rocks at pressures to 10 kilobars, *in* Knopoff, L., Drake, C.L., and Hart, P.J., eds., The crust and upper mantle of the Pacific area: American Geophysical Union, v. 12, p. 501-516.

Mao, N.-H., Ito, J., Hays, J.F., Drake, J., and Birch, F., 1970, Composition and elastic constants of hortonolite dunite: Journal of Geophysical Research, v. 75, p. 4071-4076.

McClain, J.S., and Atallah, C.A., 1985, The structure of young oceanic crust near a very fast spreading ridge: Geophysical Research Letters, v. 12, p. 689-692.

McKenzie, D., 1984, The generation and compaction of partially molten rock: Journal of Petrology, v. 25, p. 713-765.

Mizutani, H., and Newbigging, D.F., 1973, Elastic wave velocities of Apollo 14, 15 and 16 rocks: Proceedings of the Fourth Lunar Science Conference, v. 3, p. 2601-2609.

Mogi, K., 1958, Relations between the eruptions of various volcanoes and the deformations of the ground surfaces around them: Bulletin of Earthquake Research Institute, Tokyo University, v. 36, p. 99-134.

Moore, J.G., 1975, Mechanism of formation of pillow lava: American Scientist, v. 63, p. 269-277.

Moore, J.G., and Fiske, R.S., 1969, Volcanic substructure inferred from dredge samples and ocean bottom photographs, Hawaii: Geological Society of America Bulletin, v. 80, p. 1191-1202.

Moore, R.B., Helz, R.T., Dzurisin, D., Eaton, G.P., Koyanagi, R.Y., Lipman, P.W., Lockwood, J.P., and Puniwai, G.P., 1980, The 1977 eruption of Kilauea Volcano, Hawaii: Journal of Volcanology and Geothermal Research, v. 7, p. 189-210.

Murase, T., and McBirney, A.R., 1973, Properties of some common igneous rocks and their melts at high temperatures: Geological Society of America Bulletin, v. 84, p. 3563-3592.

Nakamura, K., 1980, Why do long rift zones develop in Hawaiian volcanos—a possible role of thick oceanic sediments: Bulletin of the Volcanology Society of Japan, v. 25, p. 255-269.

O'Connell, R.J., and Budiansky, B., 1974, Seismic velocities in dry and cracked solids: Journal of Geophysical Research, v. 79, p. 5412-5426.

Peck, D.L., and Kinoshita, W.T., 1976, The eruption of August 1963 and the formation of Alae lava lake, Hawaii: U.S. Geological Survey Professional Paper 935-A, 33 p.

Pollard, D.D., 1976, On the form and stability of open hydraulic fractures in the Earth's crust: Geophysical Research Letters, v. 3, p. 513-516.

Pollard, D.D., and Holzhausen, G., 1979, On the mechanical interaction between a fluid-filled fracture and the Earth's surface: Tectonophysics, v. 53, p. 27-57.

Pollard, D.D., and Muller, O.H., 1976, The effect of gradients in regional stress and magma pressure on the form of sheet intrusions in cross section: Journal of Geophysical Research, v. 81, p. 975-984.

Purdy, G.M., and Detrick, R.S., 1986, Crustal structure of the mid-Atlantic ridge at 23°N seismic refraction studies: Journal of Geophysical Research, v. 91, p. 3729-3762.

Ramberg, H., 1981, Gravity and deformation of the Earth's crust: New York, Academic Press, 452 p.

Rao, M., Ramana, Y.V., and Gogte, B.S., 1974, Dependence of compressional velocity on the mineral chemistry of eclogites: Earth and Planetary Science Letters, v. 23, p. 15-20.

Renard, V., Hekinian, R., Francheteau, J., Ballard, R.D., and Backer, H., 1985. Submersible operations at the axis of the ultra-fast-spreading East Pacific rise (17°30′ to 21°30′S): Earth and Planetary Science Letters, v. 75, p. 339-353.

Reuss, A., 1929, Berechnung der Fleissgrenze von Mischkristallen auf Grund der Plastizitätsbedingung für Einkristalle: Zeitschrift für Angewandte Mathematik und Mechanik, v. 9, p. 49

Richter, D.H., and Simmons, G., 1974, Thermal expansion behavior of igneous rocks: International Journal of Rock Mechanics and Mining Sciences & Geomechanics Abstracts, v. 11, p. 403-411.

Richter, D.H., and Moore, J.G., 1966, Petrology of Kilauea Iki lava lake, Hawaii: U.S. Geological Survey Professional Paper 537–B, 26 p.

Richter, D.H., and Murata, K.J., 1966, Petrography of the lavas of the 1959–60 eruption of Kilauea Volcano, Hawaii: U.S. Geological Survey Professional Paper 537–D, 12 p.

Ritzert, M., and Jacoby, W.R., 1985, On the lithospheric seismic structure of Reykjanes ridge at 62.5°N: Journal of Geophysical Research, v. 90, p. 10117-10128.

Robie, R.A., Hemingway, B., and Fisher, J., 1978, Thermodynamic properties of minerals and related substances at 298.15K and 1 bar (10^5 pascals) pressure and at higher temperatures: U.S. Geological Survey Bulletin 1452, 456 p.

Robie, R.A., and Waldbaum, D.R., 1968, Thermodynamic properties of minerals and related substances at 298.15K (25.0°C) and one atmosphere (1.013 bars) pressure and at higher temperatures: U.S. Geological Survey Bulletin 1259,

Ryan, M.P., Blevins J.Y.K., Okamura, A.T., and Koyanagi, R.Y., 1983, Magma reservoir subsidence mechanics: Theoretical summary and application to Kilauea Volcano, Hawaii: Journal of Geophysical Research, v. 88, p. 4147-4181.

Ryan, M.P., Koyanagi, R.Y., and Fiske, R.S., 1981, Modeling the three-dimensional structure of magma transport systems: Application to Kilauea Volcano, Hawaii: Journal of Geophysical Research, v. 86, p. 7111-7129.

Ryan, M.P., and Sammis, C.G., 1978, Cyclic fracture mechanisms in cooling basalt: Geological Society of America Bulletin, v. 89, p. 1295-1308.

———1981, The glass transition in basalt: Journal of Geophysical Research, v. 86, p. 9519-9535.

Ryzhova, T.V., 1964, The elastic properties of plagioclase: Izvestia Geophysics, ser. 7, p. 1049-1051.

Salisbury, M.H., and Christensen, N.I., 1976, Sonic velocities and densities of basalts from the Nazca plate, DSDP leg 34, *in* Yeats, R.S., Hart, S.R., and others, eds., Initial Reports of the Deep Sea Drilling Project: U.S. Government Printing Office, v. 34, p. 543-546.

Schock, R.N., Heard, H.C., and Stephens, D.R., 1973, Stress-strain behavior of a granodiorite and two greywackes on compression to 20 kilobars: Journal of Geophysical Research, v. 78, p. 5922-5941.

Schreiber, E., Fox, P.J., and Peterson, J.J., 1972, Compressional wave velocities in selected samples of gabbro, schist, limestone, anhydrogypsum and halite, *in* Ryan, W.B.F., Hsu, K.J., and others, eds., Initial reports of the Deep Sea Drilling Project: U.S. Government Printing Office, v. 13, p. 595-597.

———1974, Compressional wave velocities in samples recovered from DSDP leg 24, *in* Fisher, R.L., and others, eds., Initial reports of the Deep Sea Drilling Project: U.S. Government Printing Office, v. 24, p. 787-789.

Shaw, H.R., 1980, The fracture mechanisms of magma transport from the mantle to the surface, *in* R.B. Hargraves, ed., Physics of magmatic processes: Princeton, N.J., Princeton University Press, p. 201-264.

Shaw, H.R., and Swanson, D.A., 1970, Eruption and flow rates of flood basalts, *in* Gilmour, E.H., and Stradling, D., eds., Proceedings of the Second Columbia River Basalt Symposium: Cheney, Eastern Washington State College Press.

Simmons, G., and Wang, H., 1971, Single crystal elastic constants and calculated aggregate properties: A handbook (2d ed.): Cambridge, Massachusetts Institute of Technology Press, 370 p.

Skinner, B.J., 1966, Thermal expansion, sec. 6 *of* Clark, S.P., ed., Handbook of physical constants (revised ed.): Geological Society of America Memoir 97, p. 75-96.

Sleep, N.H., 1974, Segregation of magma from a mostly crystalline mush: Geological Society of America Bulletin, v. 85, p. 1225-1232.

Soga, N., and Anderson, O.L., 1967, High-temperature elasticity and expansivity of forsterite and steatite: Journal of the American Ceramic Society, v. 50, p. 239-359.

Solomon, S.C., 1975, Mare volcanism and lunar crustal structure, *in* Proceedings of the Sixth Lunar Science Conference: Elmsford, N.Y., Pergamon Press, p. 2021-2042.

Sparks, R.S.J., and Huppert, H.E., 1984, Density changes during the fractional crystallization of basaltic magmas: Fluid dynamic implications: Contributions to Mineralogy and Petrology, v. 85, p. 300-309.

Spence, D.A., and Turcotte, D.L., 1985, Magma-driven propagation of cracks: Journal of Geophysical Research, v. 90, p. 575-580.

Spinner, S., and Tefft, W.E., 1961, A method for determining mechanical resonance frequencies and for calculating elastic moduli from these frequencies: Proceedings of the American Society of Testing and Materials, p. 1221-1238.

Spudich, P., and Orcutt, J., 1980, A new look at the seismic velocity structure of the oceanic crust: Review of Geophysics and Space Physics, v. 18, p. 627- 645.

Stolper, E., Walker, D., Hager, B.H., and Hays, J.F., 1981, Melt segregation from partially molten source regions: The importance of melt density and source region size: Journal of Geophysical Research, v. 86, p. 6261-6271.

Swanson, D.A., Duffield, W.A., and Fiske, R.S., 1976, Displacement of the south flank of Kilauea Volcano: The result of forceful intrusion of magma into the rift zones: U.S. Geological Survey Professional Paper 963, 39 p.

Swanson, D.A., Jackson, D.B., Koyanagi, R.Y., and Wright, T.L., 1976, The February 1969 rift eruption of Kilauea Volcano, Hawaii: U.S. Geological Survey Professional Paper 891, 30 p.

Talwani, M., Worzel, J.L., and Landisman, M., 1959, Rapid gravity computations for two-dimensional bodies with application to the Mendocino submarine fracture zone: Journal of Geophysical Research, v. 64, p. 49-59.

Thompson, R.N., and Tilley, C.E., 1969, Melting and crystallization relations of Kilauean basalts of Hawaii. The lavas of the 1959-60 Kilauea eruption: Earth and Planetary Science Letters, v. 5, p. 469-477.

Tilley, C.E., 1950, Some aspects of magmatic evolution: Quarterly Journal of the Geological Society of London, v. 106, p. 37-61.

Todd, T., and Simmons, G., 1972, Effect of pore pressure on the velocity of compressional waves in low-porosity rocks: Journal of Geophysical Research, v. 77, p. 3731-3743.

Vogt, P.R., 1974, Volcano height and plate thickness: Earth and Planetary Science Letters, v. 23, p. 337-348.

Voigt, W., 1928, Lehrbuch der Kristallphysik: Leipzig, B.B. Teubner.

Volarovich, M.P., and Gurvich, A.S., 1957, Investigation of dynamic moduli of elasticity for rocks in relation to temperature: Izvestia Akademiya Nauk SSSR. Seriya Geofiziko, no. 4, p. 417-425.

Waff, H.S., 1979, Equilibrium fluid distribution in an ultramafic partial melt under hydrostatic stress conditions: Journal of Geophysical Research, v. 84, p. 6109-6114.

———1980, Effects of the gravitational field on liquid distribution in partial melts within the upper mantle: Journal of Geophysical Research, v. 85, p. 1815-1825.

Waff, H.S., and Bulau, J.R., 1979, Equilibrium fluid distribution in an ultramafic partial melt under hydrostatic stress conditions: Journal of Geophysical Research, v. 84, p. 6109-6114.

Walsh, J.B., 1968, Attenuation in partially melted material: Journal of Geophysical Research, v. 73, p. 2209-2216.

———1969, New analysis of attenuation in partially melted rock: Journal of Geophysical Research, v. 74, p. 4333-4337.

———1981, Effect of pore pressure and confining pressure on fracture permeability: International Journal of Rock Mechanics and Mining Sciences & Geomechanics Abstracts, v. 18, p. 429-435.

Walsh, J.B., and Decker, R.W., 1971, Surface deformation associated with volcanism: Journal of Geophysical Research, v. 76, p. 3291-3302.

Wang, H., Todd, T., Richter, D., and Simmons, G., 1973, Elastic properties of plagioclase aggregates and seismic velocities, *in* The Moon: Proceedings of the Fourth Lunar Science Conference, v. 3, p. 2663-2671.

Ward, P.L., and Gregersen, S., 1973, Comparison of earthquake locations determined with data from a network of stations and small tripartite arrays on Kilauea Volcano, Hawaii: Bulletin of the Seismological Society of America, v. 63, p. 679-711.

Watt, J.P., Davies, G.F., and O'Connell, R.J., 1976, The elastic properties of composite materials: Review of Geophysics and Space Physics, v. 14, p. 541-563.

Weertman, J., 1971a, Theory of water-filled crevasses in glaciers applied to vertical magma transport beneath oceanic ridges: Journal of Geophysical Research, v. 76, p. 1171-1183.

———1971b, Velocity at which liquid-filled cracks move in the earth's crust or in glaciers: Journal of Geophysical Research, v. 76, p. 8544-8553.

———1980, The stopping of a rising, liquid-filled crack in the earth's crust by a freely slipping horizontal joint: Journal of Geophysical Research, v. 85, p. 967-976.

Weertman, J., and Chang, S.P., 1977, Fluid flow through a large vertical crack in the Earth's crust: Journal of Geophysical Research, v. 82, p. 929-932.

Whitcomb, J.H., Garmany, J.D., and Anderson, D.L., 1973, Earthquake prediction: Variation of seismic velocities before the San Fernando earthquake: Science, v. 180, p. 632-635.

Wilson, L., and Head, J.W., 1981, Ascent and eruption of basaltic magma on the Earth and Moon: Journal of Geophysical Research, v. 86, p. 2971-3001.

Wingquist, C.F., 1971, Elastic moduli of rock at elevated temperatures: U.S. Bureau of Mines Report of Investigations 7269.

Wright, T.L., and Fiske, R.S., 1971, Origin of the differentiated and hybrid lavas

of Kilauea Volcano, Hawaii: Journal of Petrology, v. 12, p. 1-65.

Wright, T.L., and Okamura, R.T., 1977, Cooling and crystallization of tholeiitic basalt, 1965 Makaopuhi lava lake, Hawaii: U.S. Geological Survey Professional Paper 1004, 78 p.

Wright, T.L., and Weiblen, P.W., 1968, Mineral composition and paragenesis in tholeiitic basalt from Makaopuhi lava lake, Hawaii [abs.], *in* Abstracts for 1967: Geological Society of America Special Paper 115, p. 242-243.

Wyss, M., and Holcomb, D.J., 1973, Earthquake prediction based on station residuals: Nature, v. 249, p. 139-140.

Yamshikov, V.S., 1965, A study of the temperature dependence of the modulus of elasticity of rocks: Izvestia, Earth Physics Series no. 10, p. 83-87.

Yoder, H.S., and Sahama, H.G., 1957, Olivine x-ray determinative curve: American Mineralogist, v. 42, p. 475-491.

Yoder, H.S., and Tilley, C.E., 1962, Origin of basalt magmas: An experimental study of natural and synthetic rock systems: Journal of Petrology, v. 3, no. 3, p. 342-532.

Zablocki, C.J., Tilling, R.I., Peterson, D.W., Christiansen, R.L., Keller, G.V., and Murray, J.C., 1974, A deep research drill hole at the summit of an active volcano, Kilauea, Hawaii: Geophysical Research Letters, v. 1, p. 323-326.

Zucca, J.J., and Hill, D.P., 1980, Crustal structure of the southeast flank of Kilauea Volcano, Hawaii, from seismic refraction measurements: Bulletin of the Seismological Society of America, v. 70, p. 1149-1159.

Zucca, J.J., Hill, D.P., and Kovach, R.L., 1982, Crustal structure of Mauna Loa Volcano, Hawaii, from seismic refraction and gravity data: Bulletin of the Seismological Society of America, v. 72, p. 1535-1550.